Figure 4.956: DH A35-A36 180deg - bridgegirder @ pylon: Torsional moment [MNm]
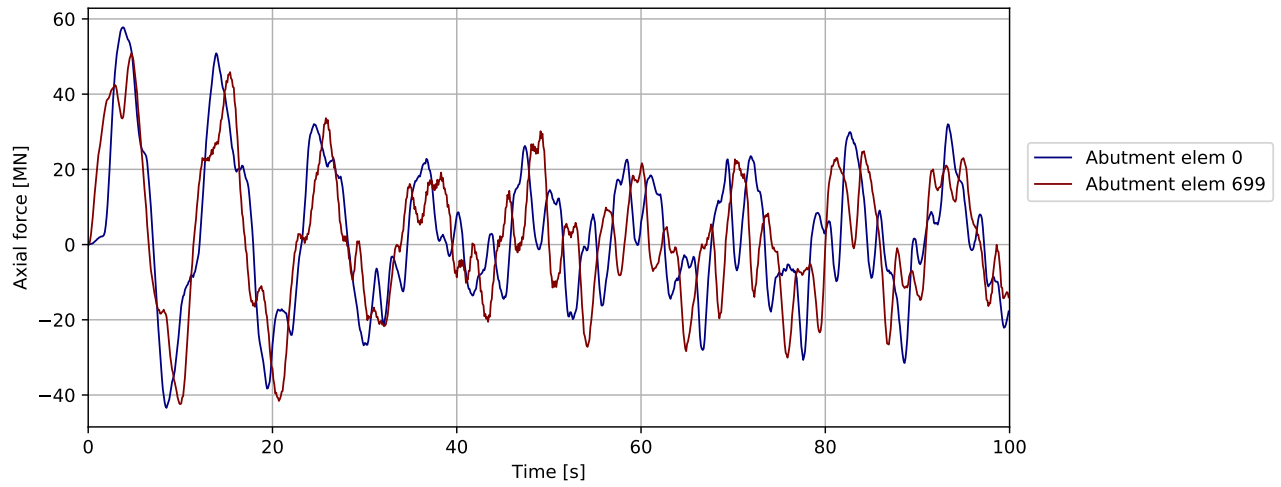

Figure 4.957: DH A35-A36 180deg - bridgegirder @abutments: Axial force [MN]
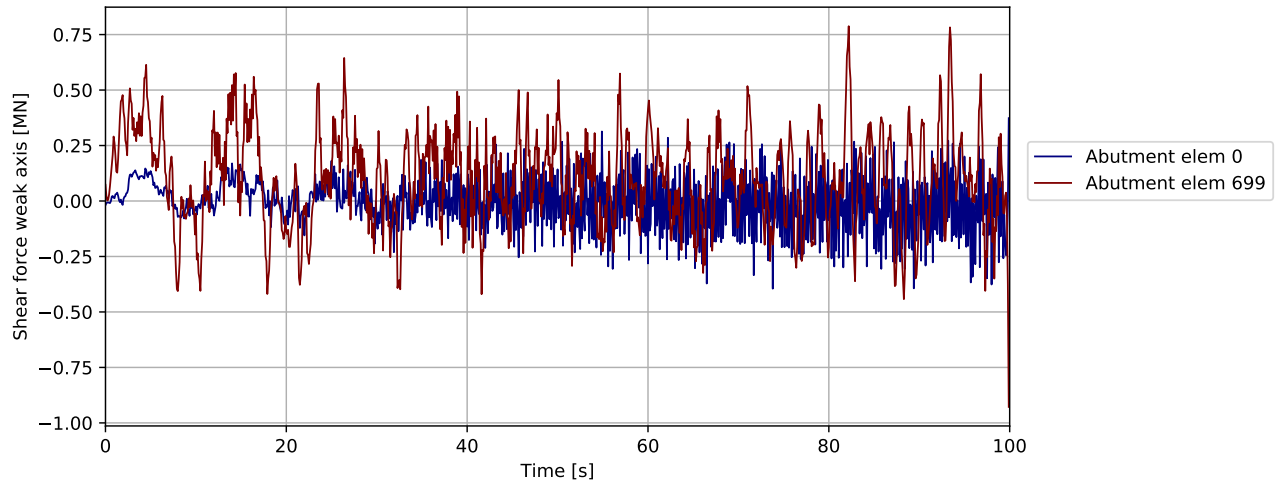
Figure 4.958: DH A35-A36 180deg - bridgegirder @abutments: Shear force weak axis [MN]
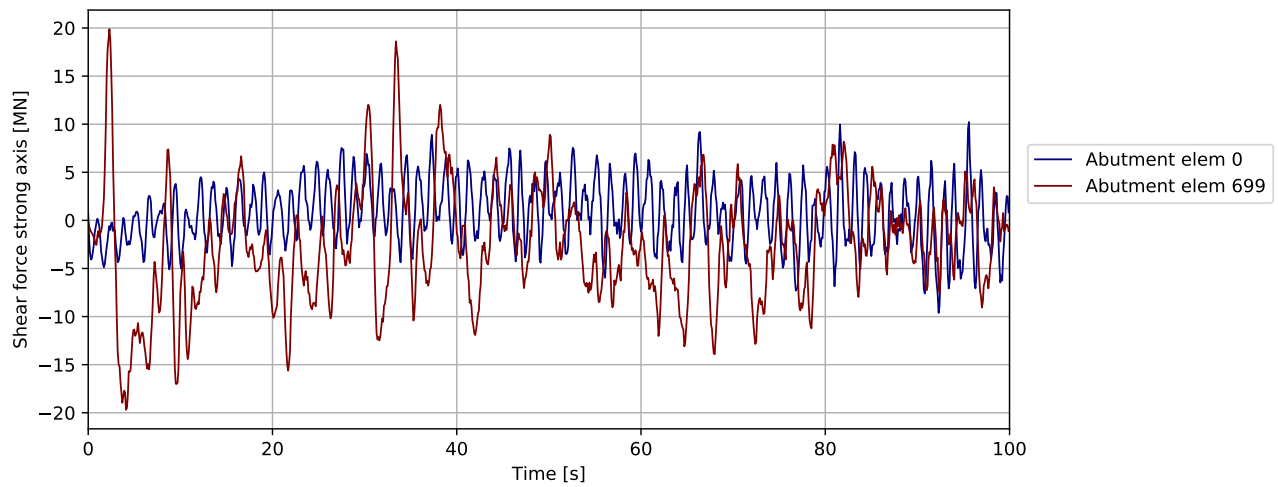

Figure 4.959: DH A35-A36 180deg - bridgegirder @abutments: Shear force strong axis [MN]
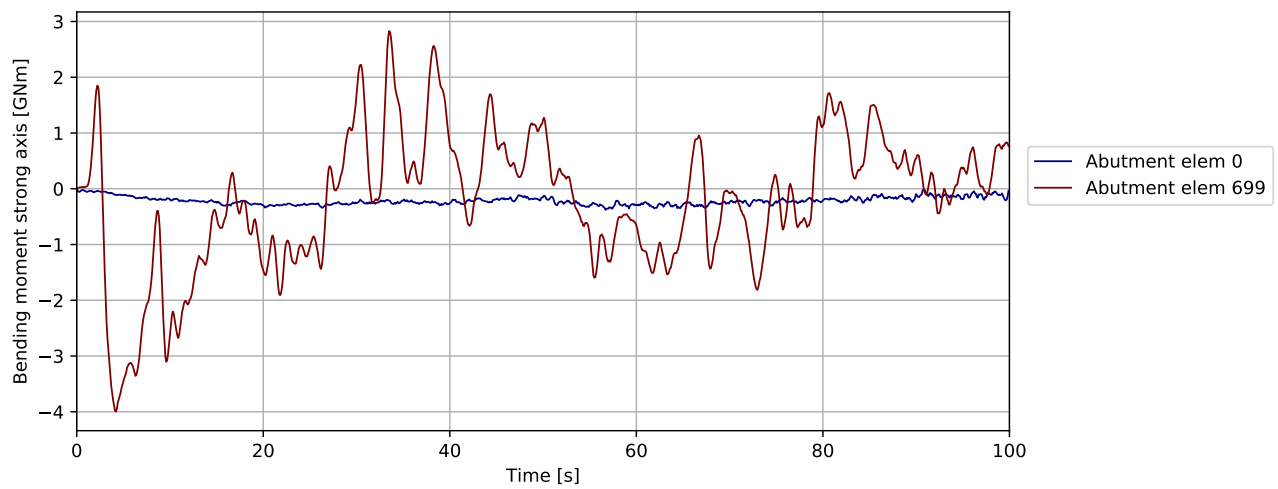

Figure 4.960: DH A35-A36 180deg - bridgegirder @abutments: Bending moment strong axis [GNm]
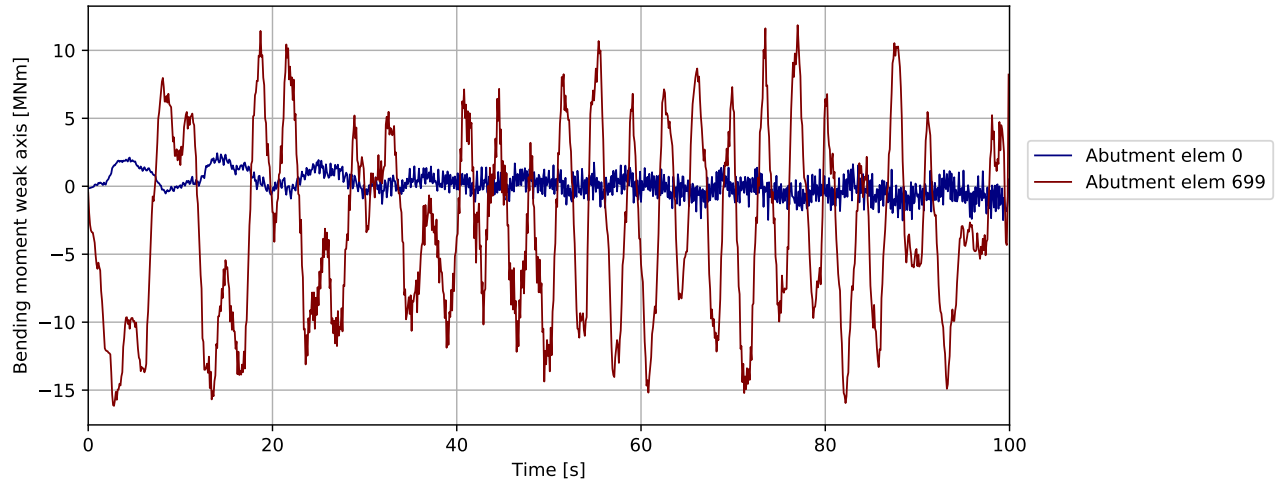
Figure 4.961: DH A35-A36 180deg - bridgegirder @abutments: Bending moment weak axis [MNm]
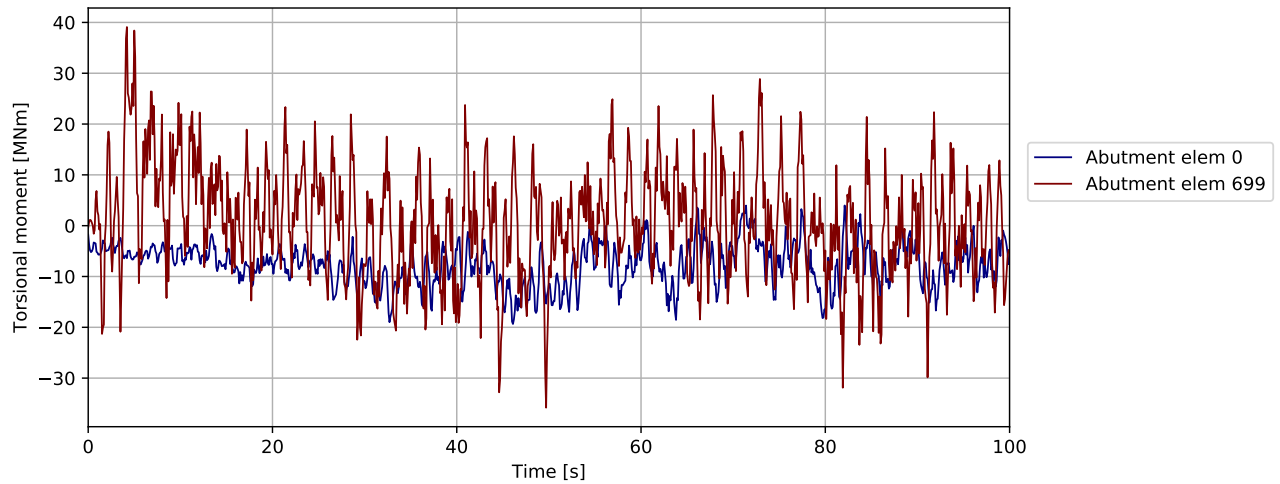

Figure 4.962: DH A35-A36 180deg - bridgegirder @abutments: Torsional moment [MNm]

Note : Compressive spring force is negative
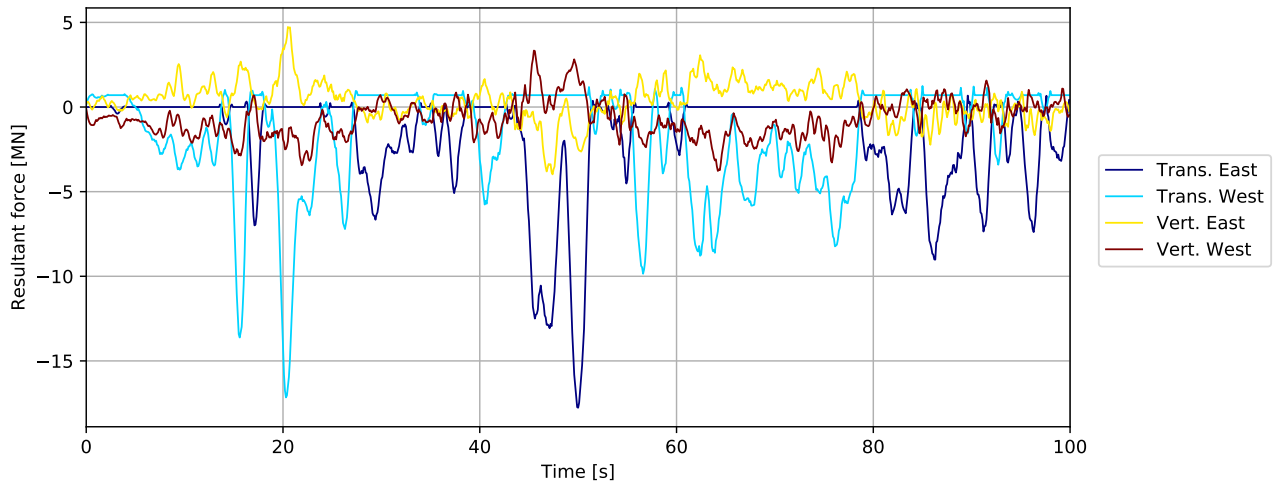

Figure 4.963: DH A35-A36 180deg - bridgegirder supports in tower: Resultant force [MN]
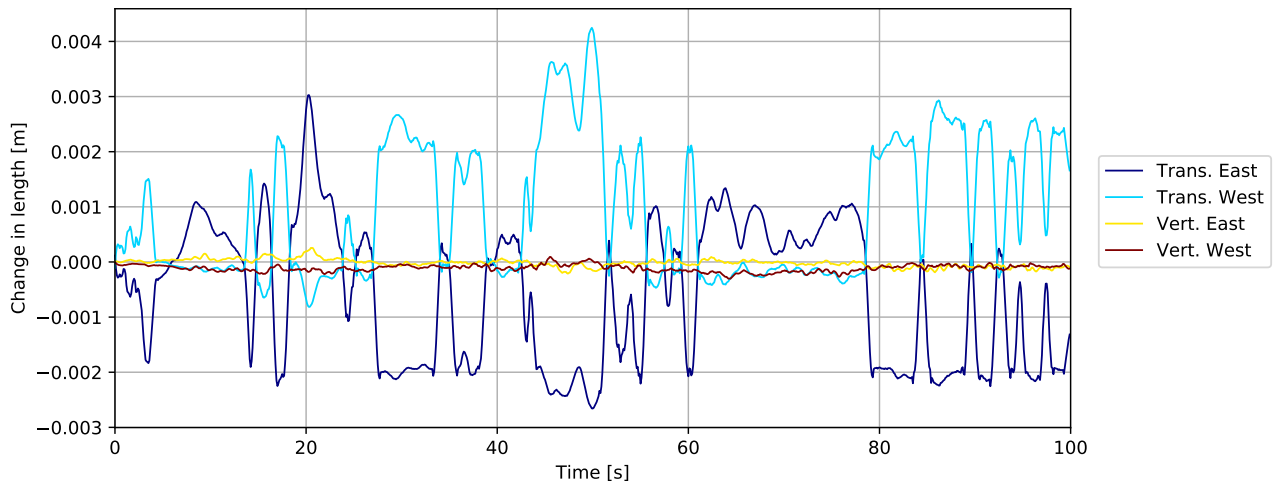
Figure 4.964: DH A35-A36 180deg - bridgegirder supports in tower: Change in length [m]
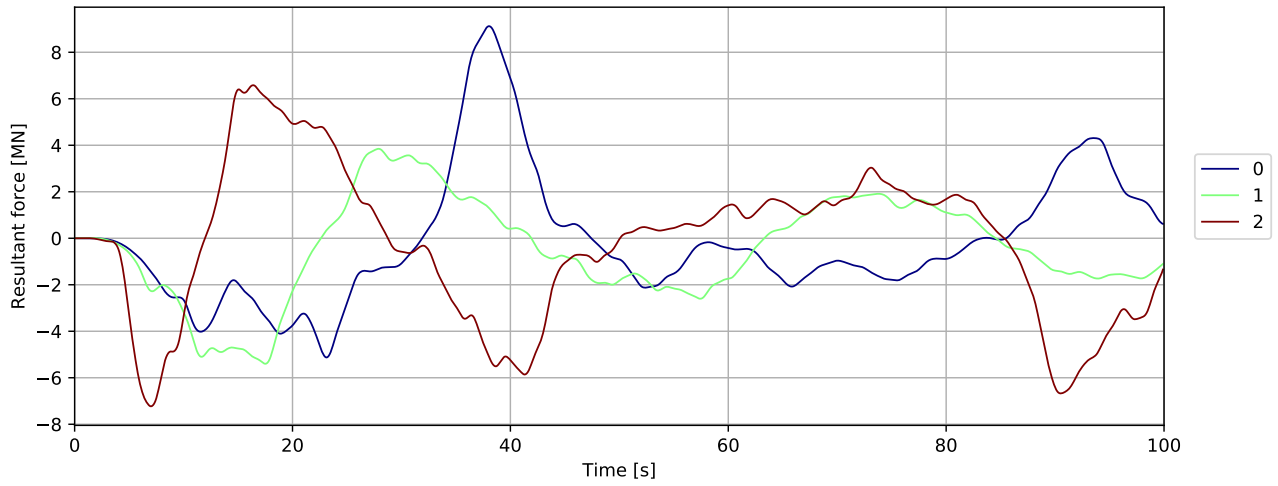
Figure 4.965: Mooring force
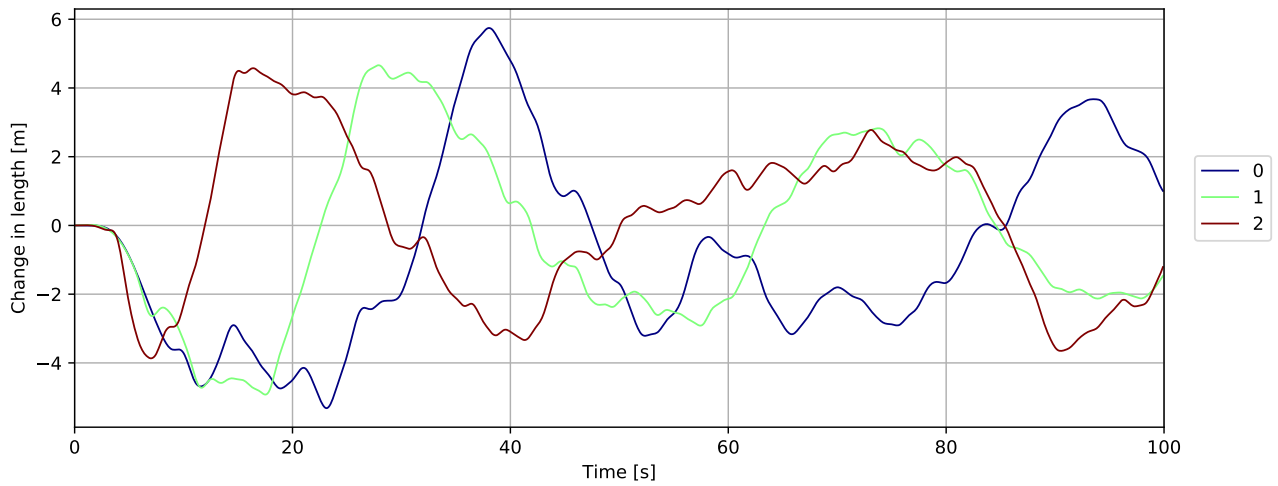
Figure 4.966: Mooring displacement

4.22   Deck house A39-A40 180deg

4.22.1   Overall response
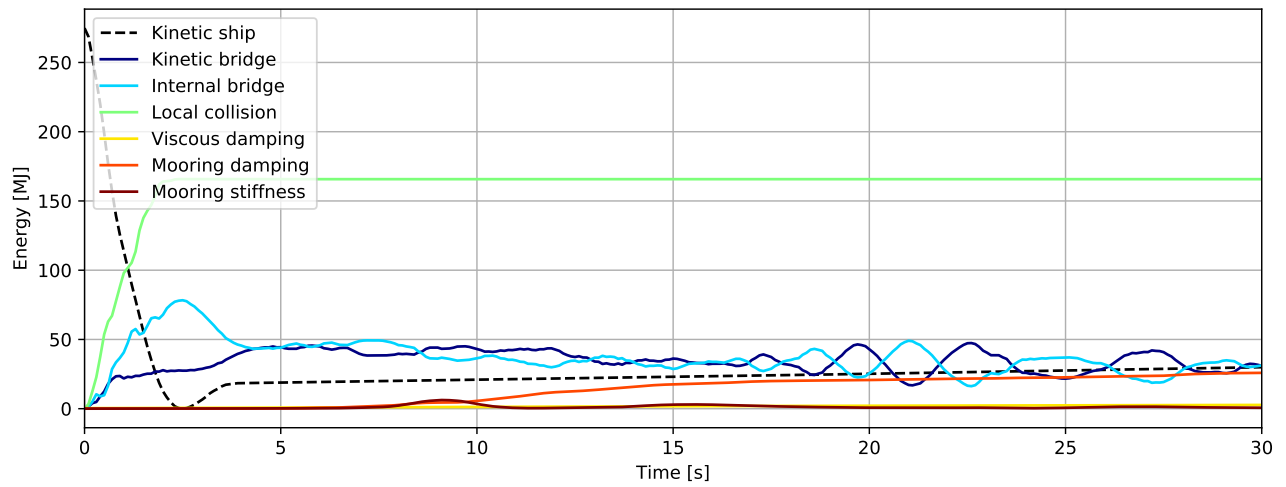
Figure 4.967: Energy [MJ] - initial phase
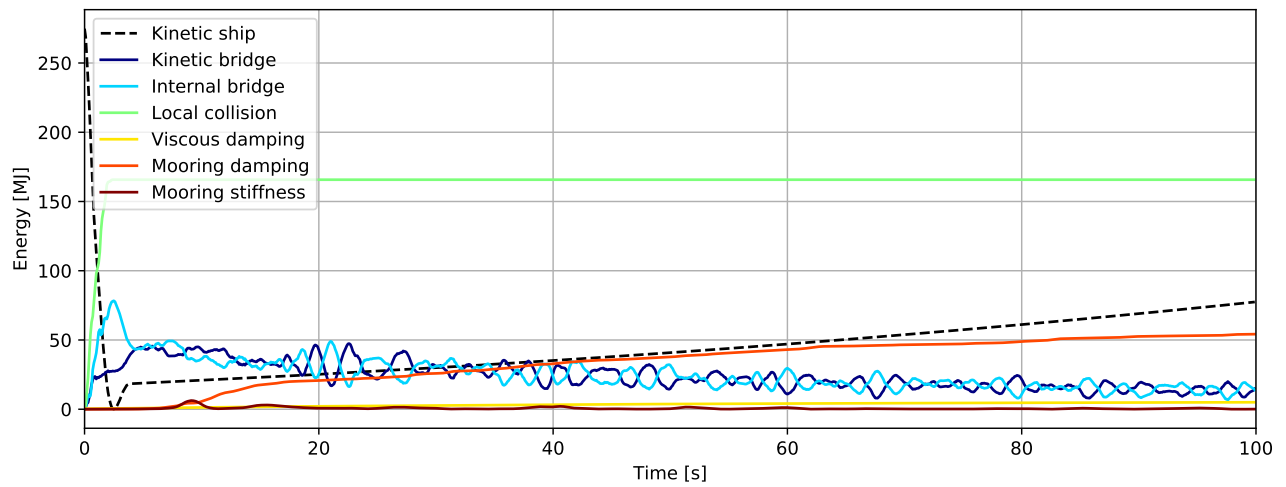
Figure 4.968: Energy [MJ]
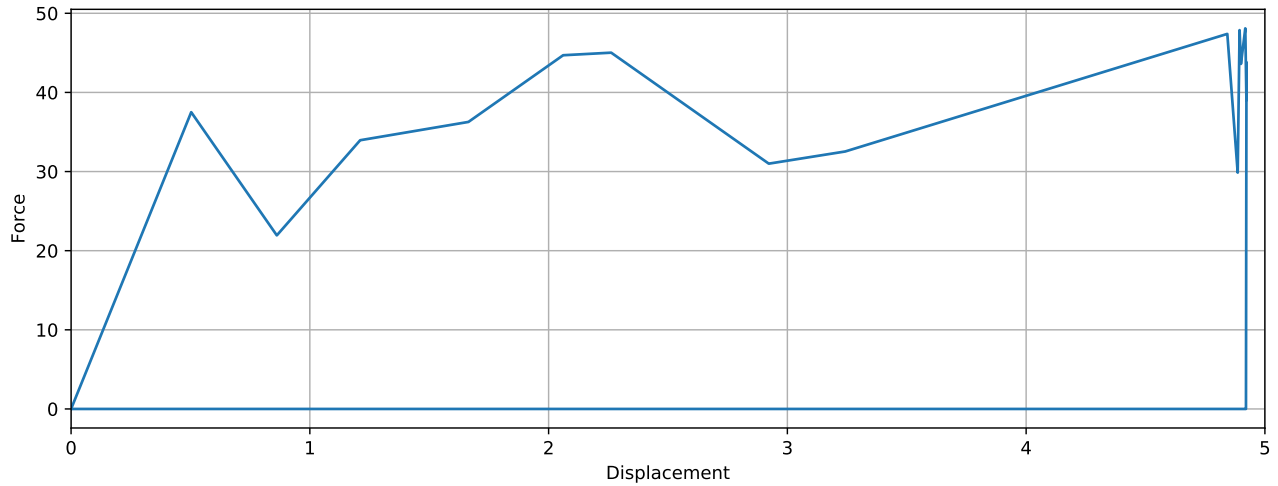
Figure 4.969: Simulated local collision force-displacement
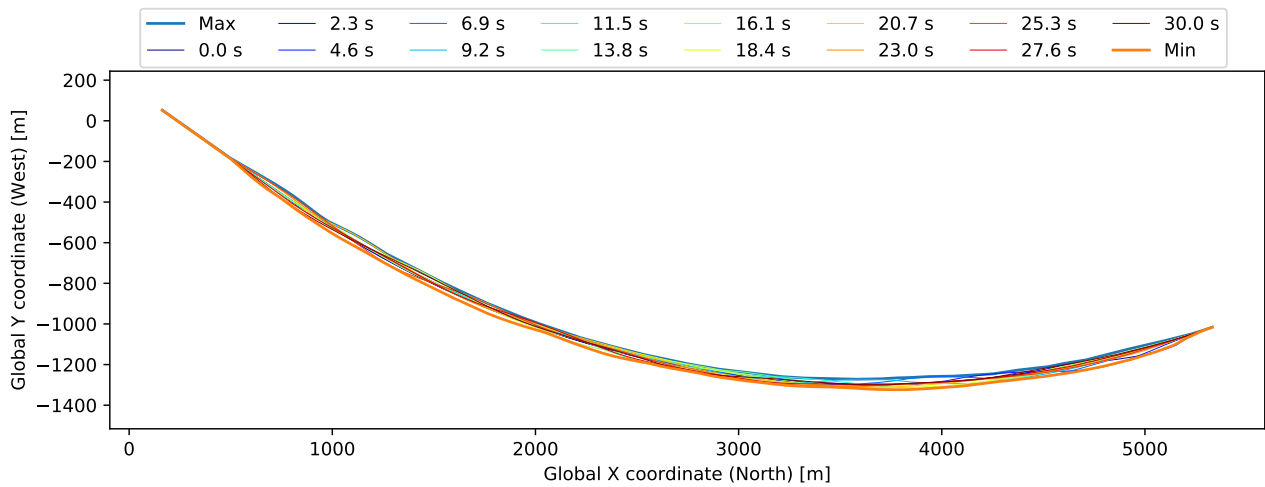
Figure 4.970: Bridgegirder deflection (10x displacment scaling)
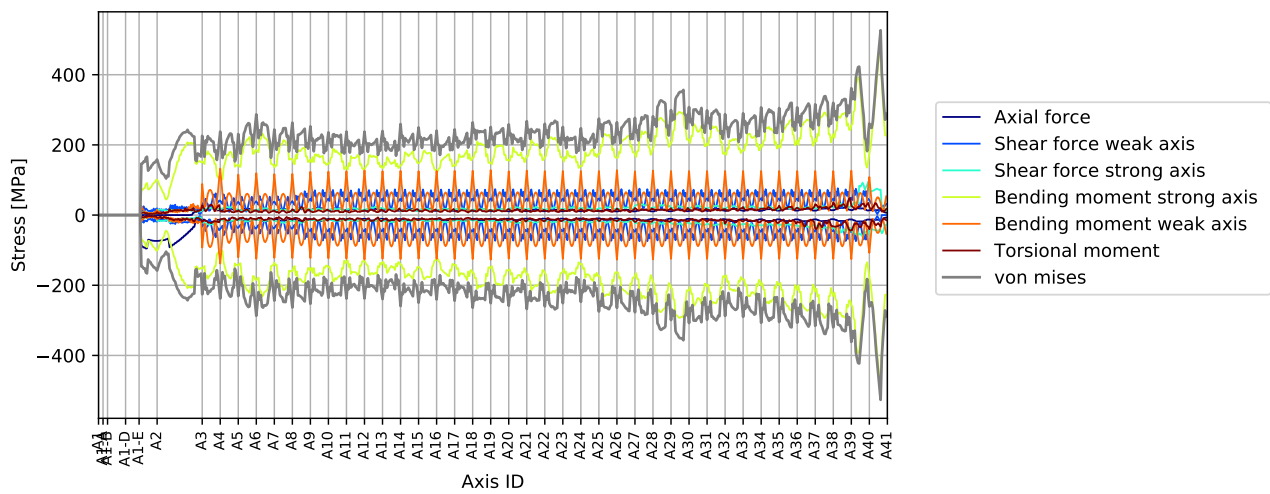
Figure 4.971: Stress envelope from all force components

4.22.2   Envelope plots
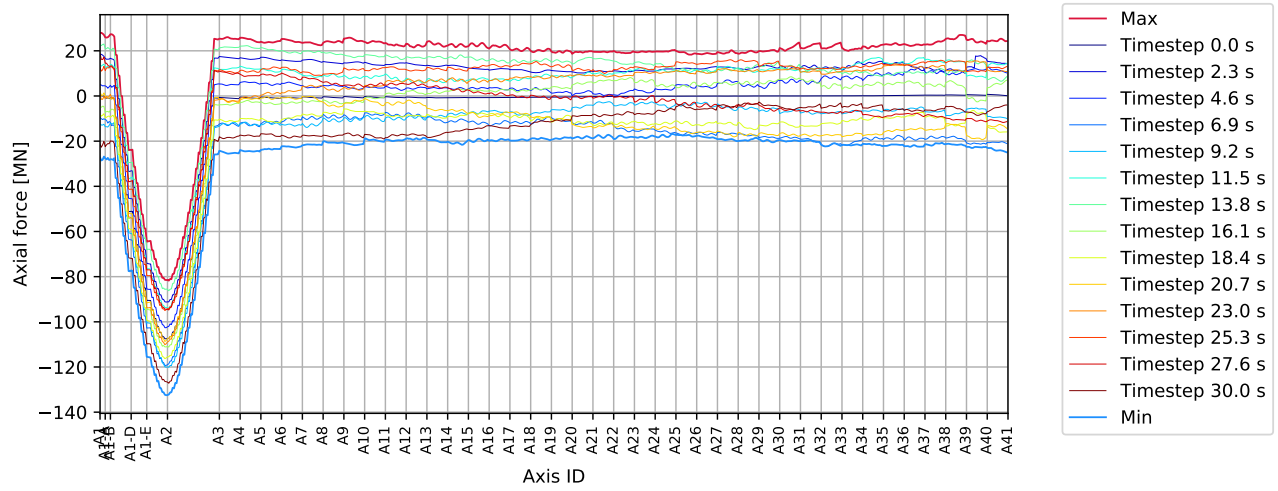
Figure 4.972: DH A39-A40 180deg - bridgegirder : Axial force [MN]
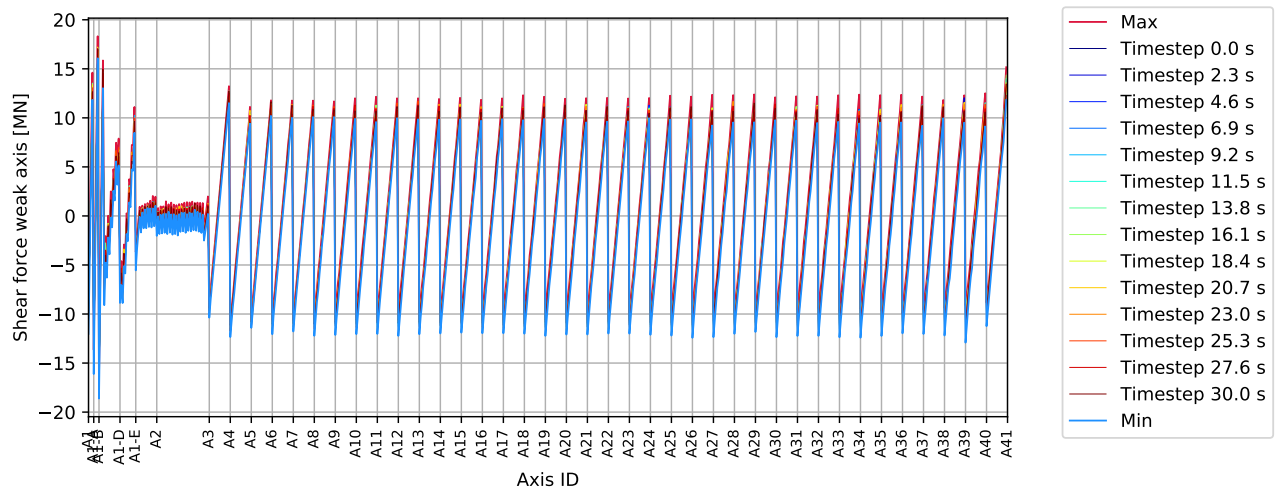
Figure 4.973: DH A39-A40 180deg - bridgegirder : Shear force weak axis [MN]

Figure 4.974: DH A39-A40 180deg - bridgegirder : Shear force strong axis [MN]

Figure 4.975: DH A39-A40 180deg - bridgegirder : Bending moment strong axis [GNm]

Figure 4.976: DH A39-A40 180deg - bridgegirder : Bending moment weak axis [MNm]

Figure 4.977: DH A39-A40 180deg - bridgegirder : Torsional moment [MNm]
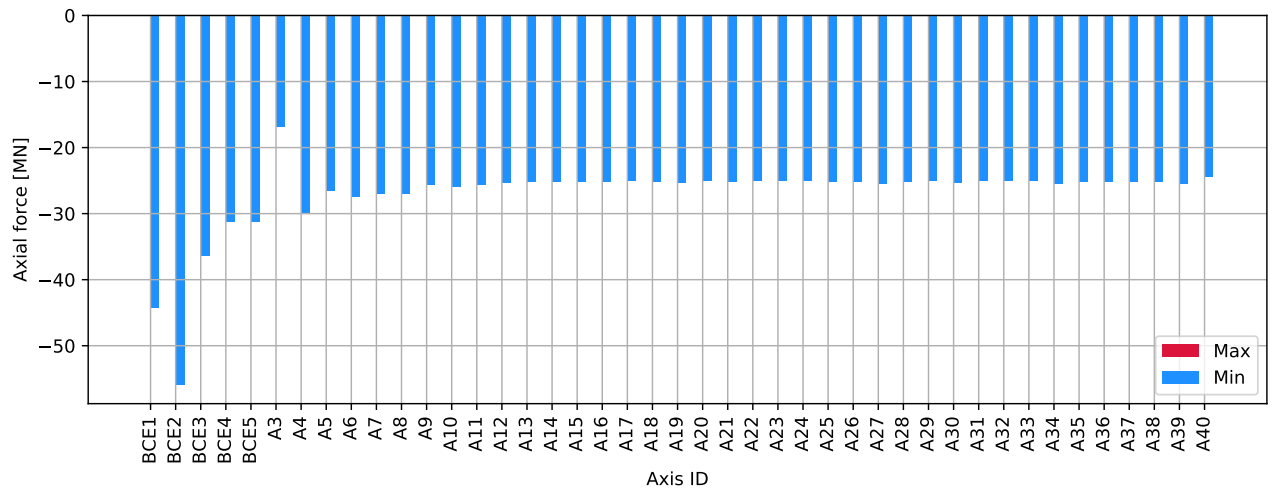
Figure 4.978: DH A39-A40 180deg - columns bottom : Axial force [MN]
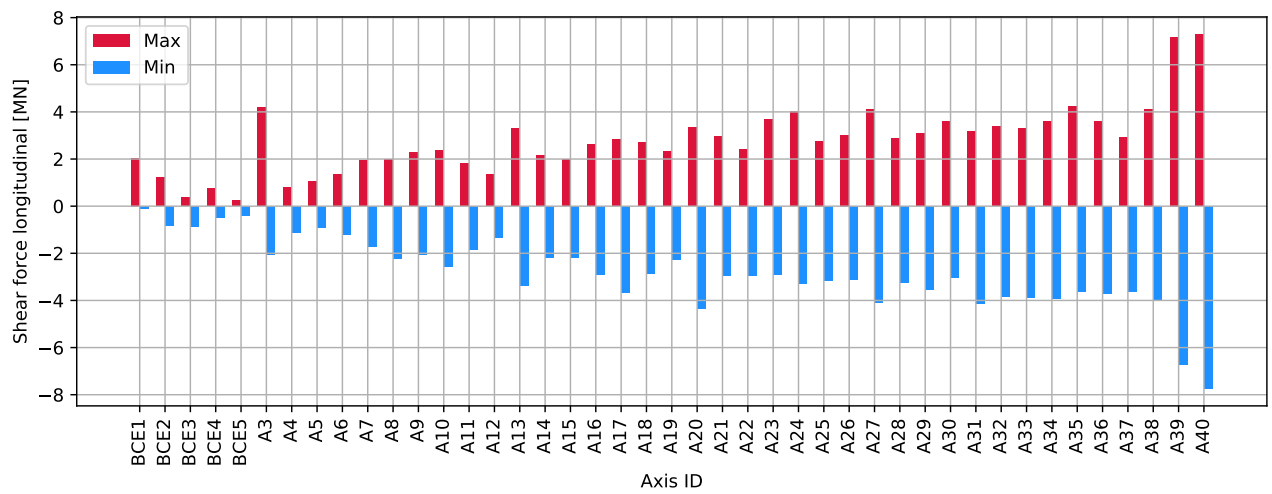
Figure 4.979: DH A39-A40 180deg - columns bottom : Shear force longitudinal [MN]
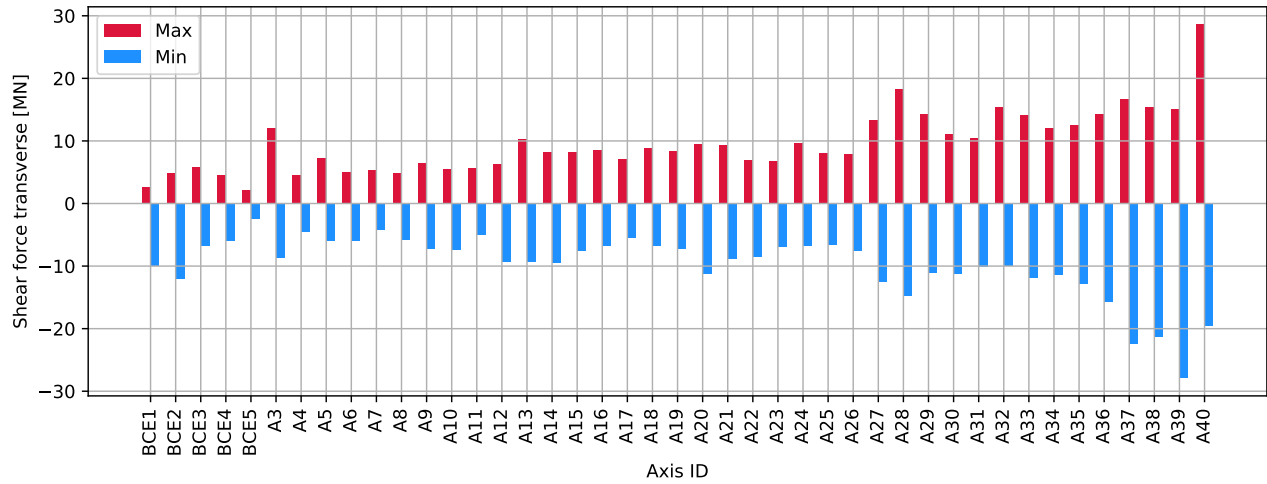
Figure 4.980: DH A39-A40 180deg - columns bottom : Shear force transverse [MN]
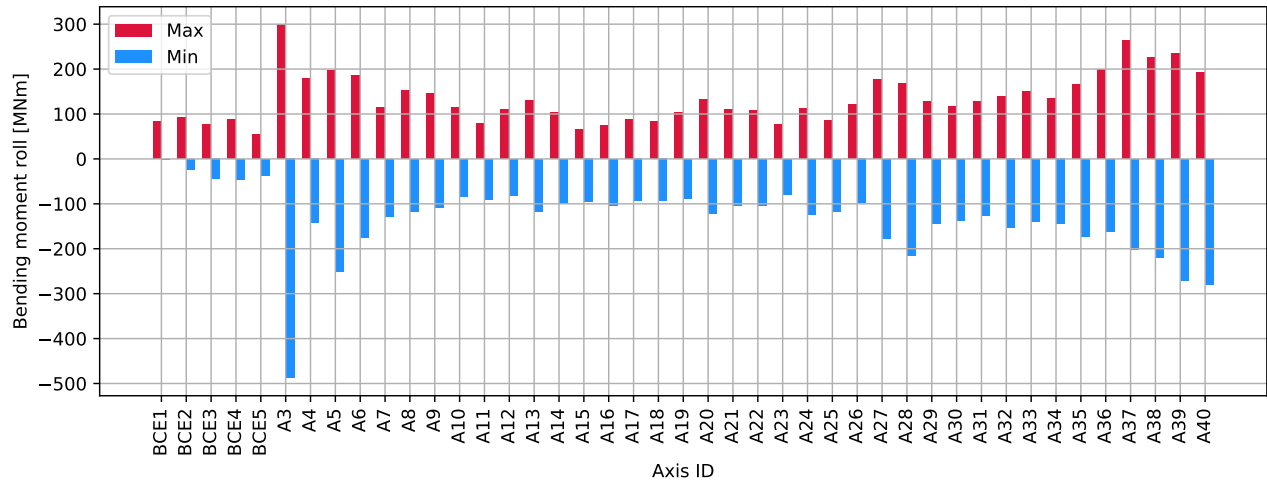
Figure 4.981: DH A39-A40 180deg - columns bottom : Bending moment roll [MNm]
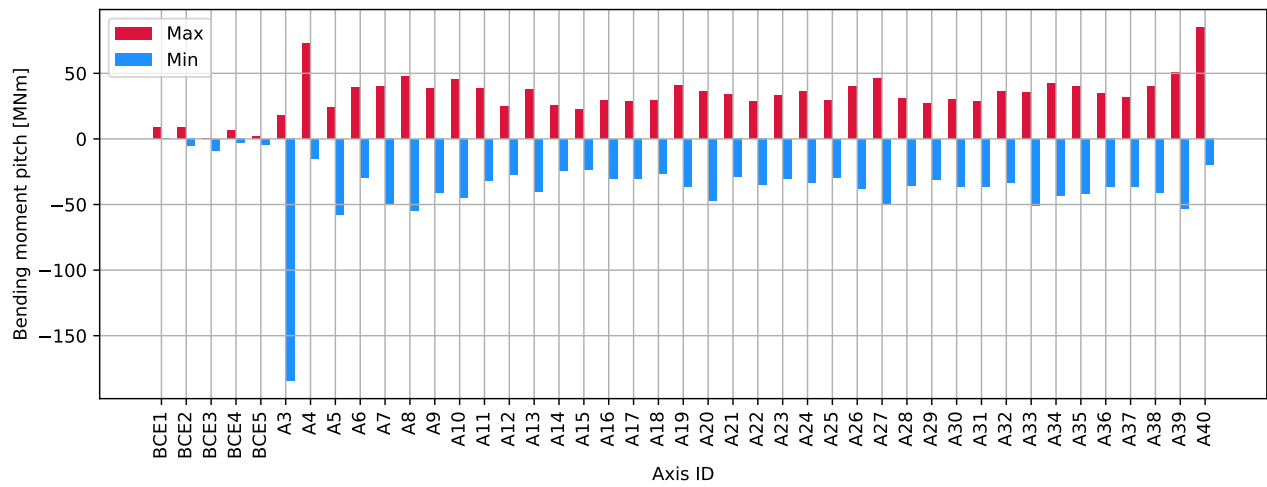
Figure 4.982: DH A39-A40 180deg - columns bottom : Bending moment pitch [MNm]
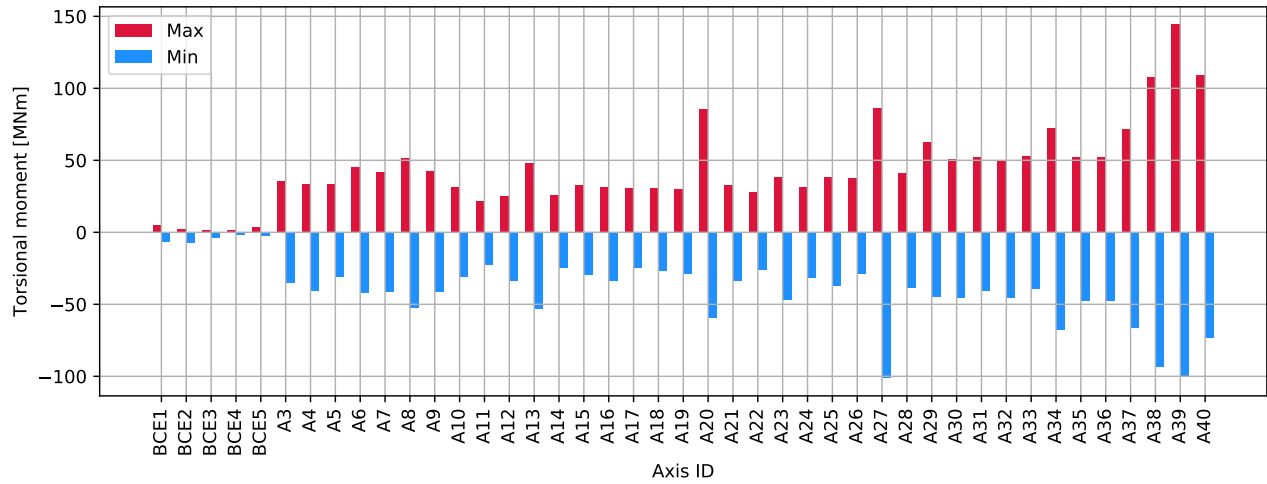
Figure 4.983: DH A39-A40 180deg - columns bottom : Torsional moment [MNm]
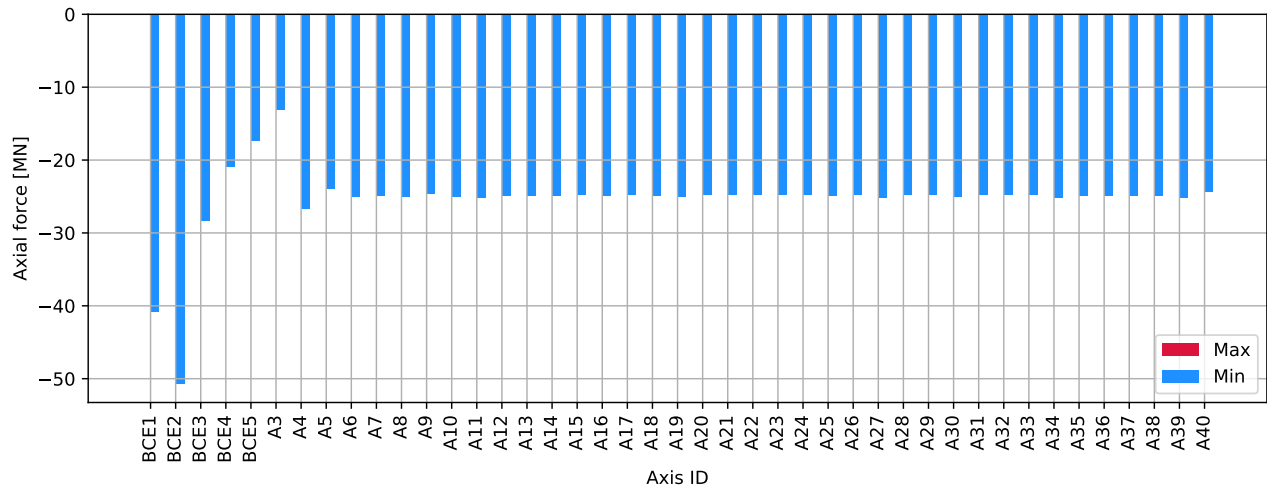
Figure 4.984: DH A39-A40 180deg - columns top : Axial force [MN]
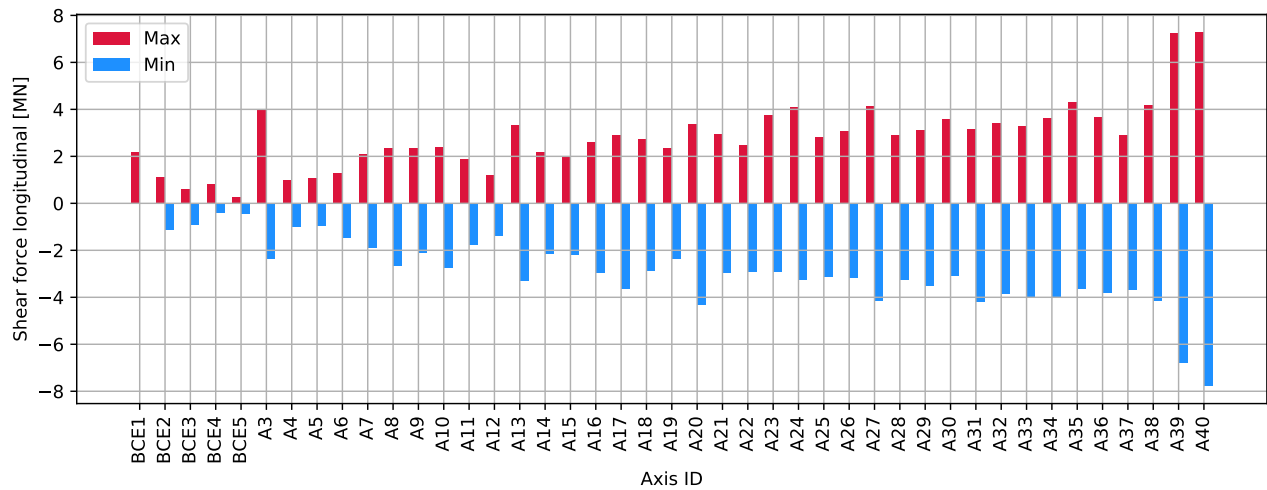
Figure 4.985: DH A39-A40 180deg - columns top : Shear force longitudinal [MN]
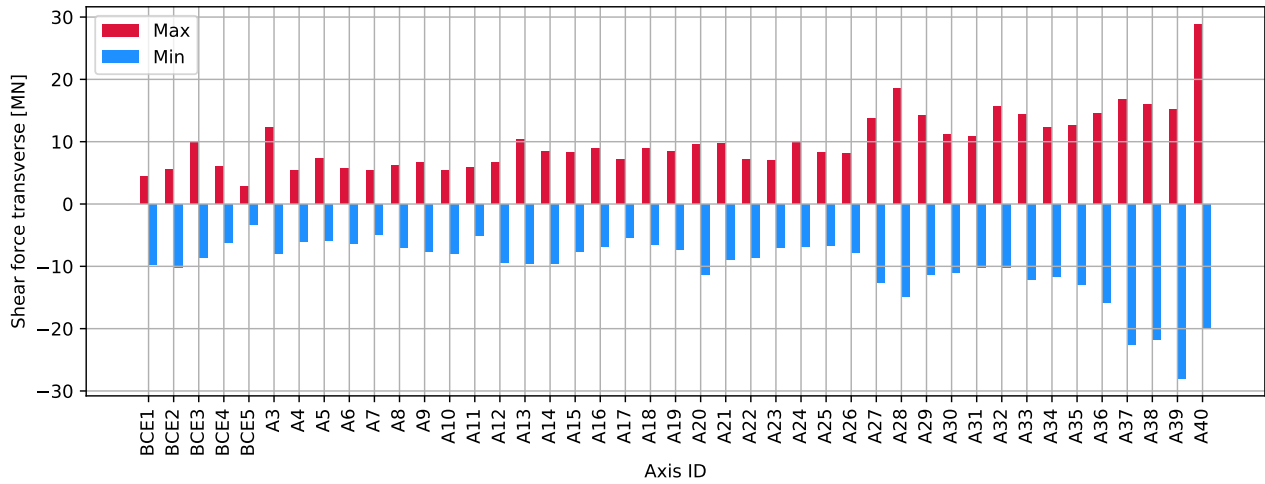
Figure 4.986: DH A39-A40 180deg - columns top : Shear force transverse [MN]
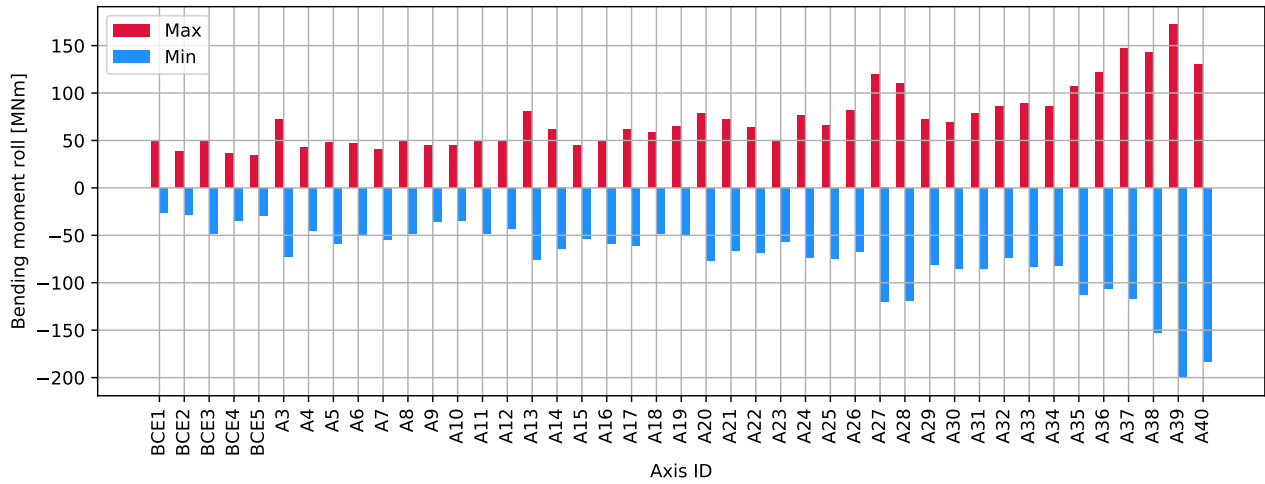
Figure 4.987: DH A39-A40 180deg - columns top : Bending moment roll [MNm]
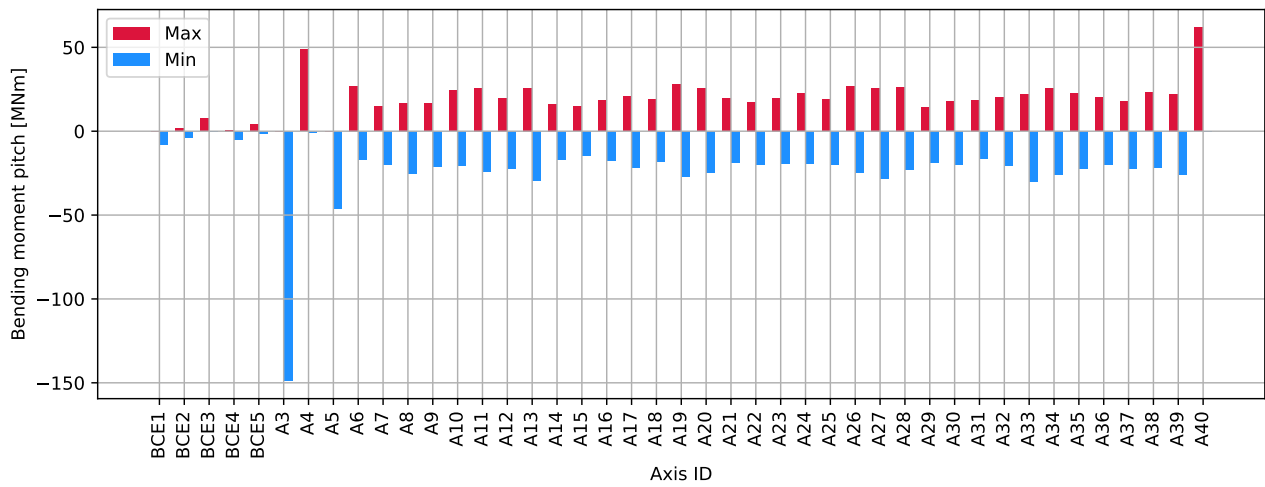
Figure 4.988: DH A39-A40 180deg - columns top : Bending moment pitch [MNm]
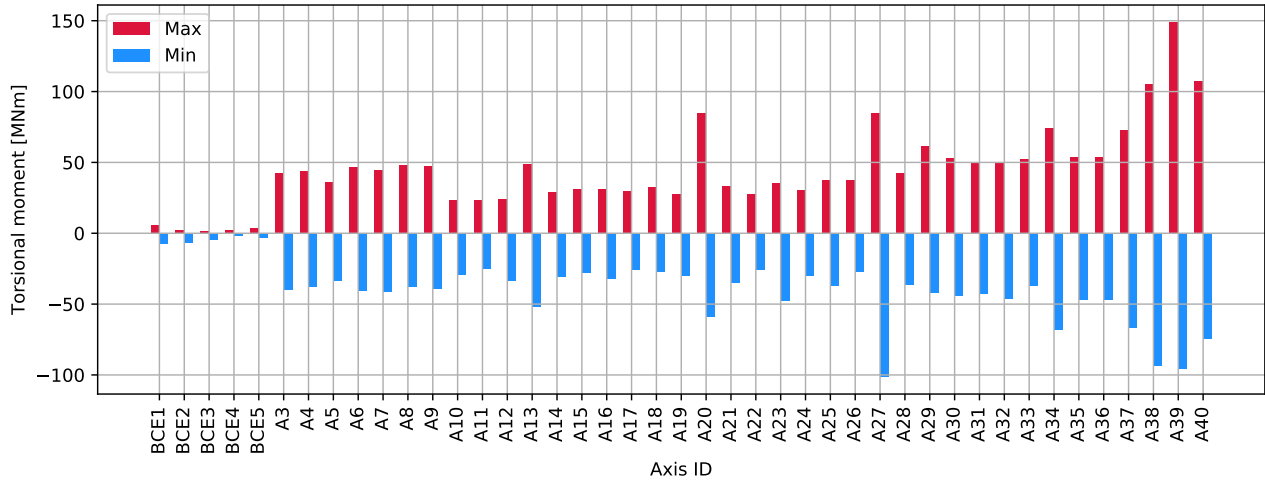
Figure 4.989: DH A39-A40 180deg - columns top : Torsional moment [MNm]
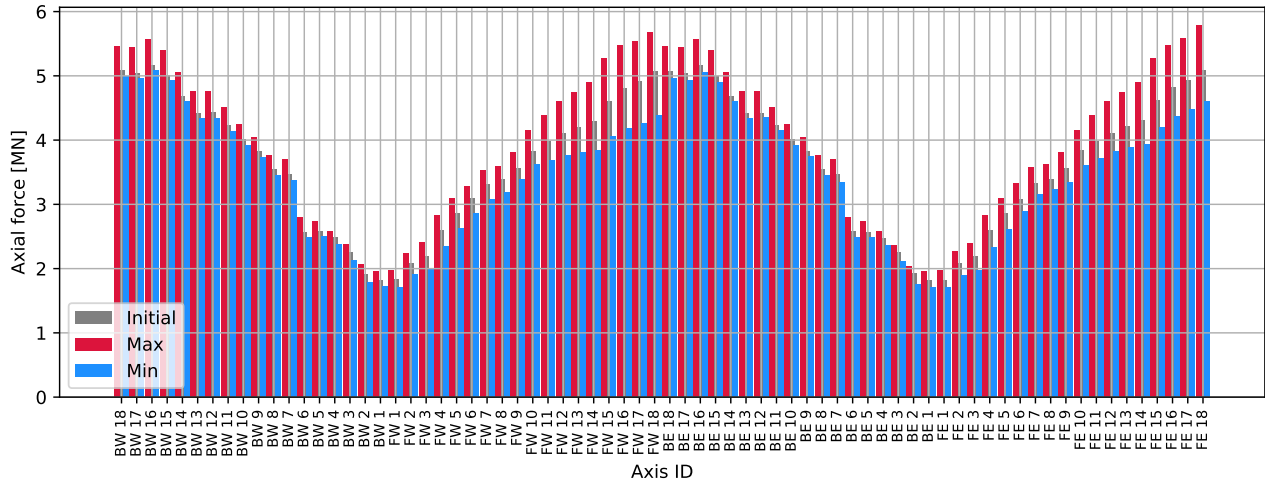
Figure 4.990: DH A39-A40 180deg - cables : Axial force [MN]
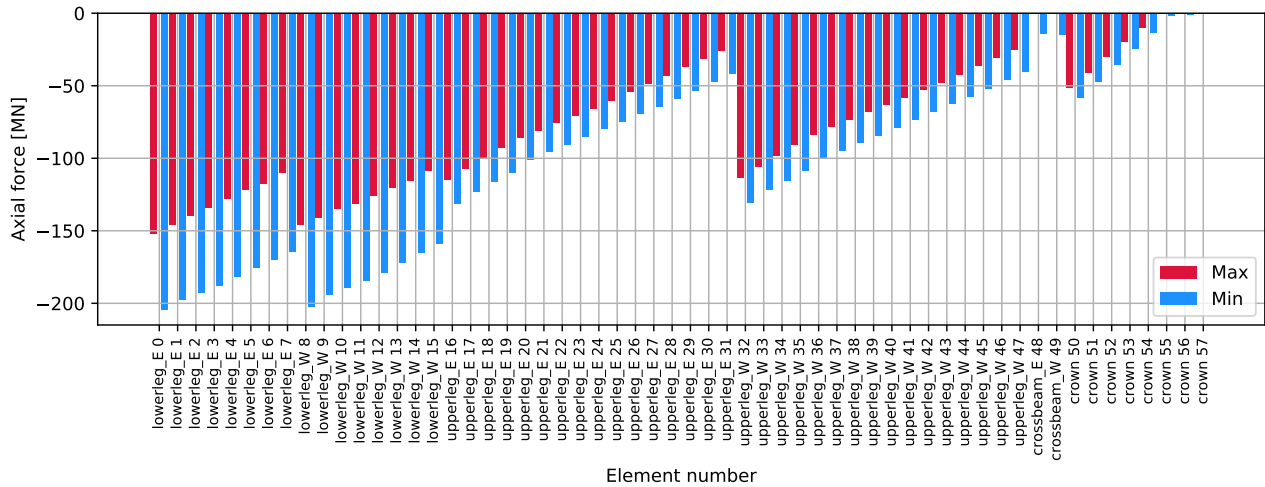
Figure 4.991: DH A39-A40 180deg - tower: Axial force [MN]
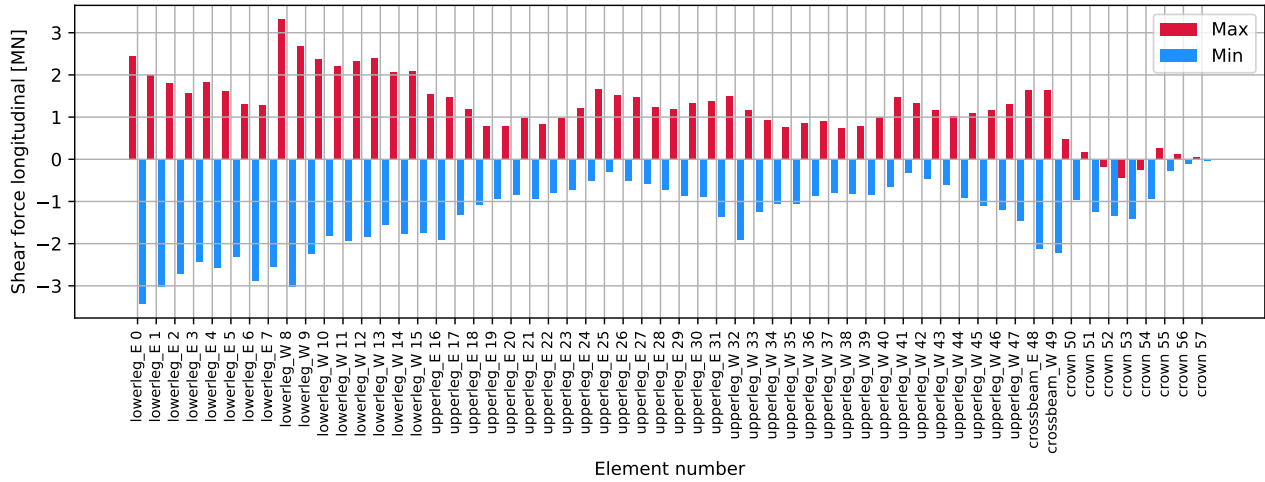
Figure 4.992: DH A39-A40 180deg - tower: Shear force longitudinal [MN]
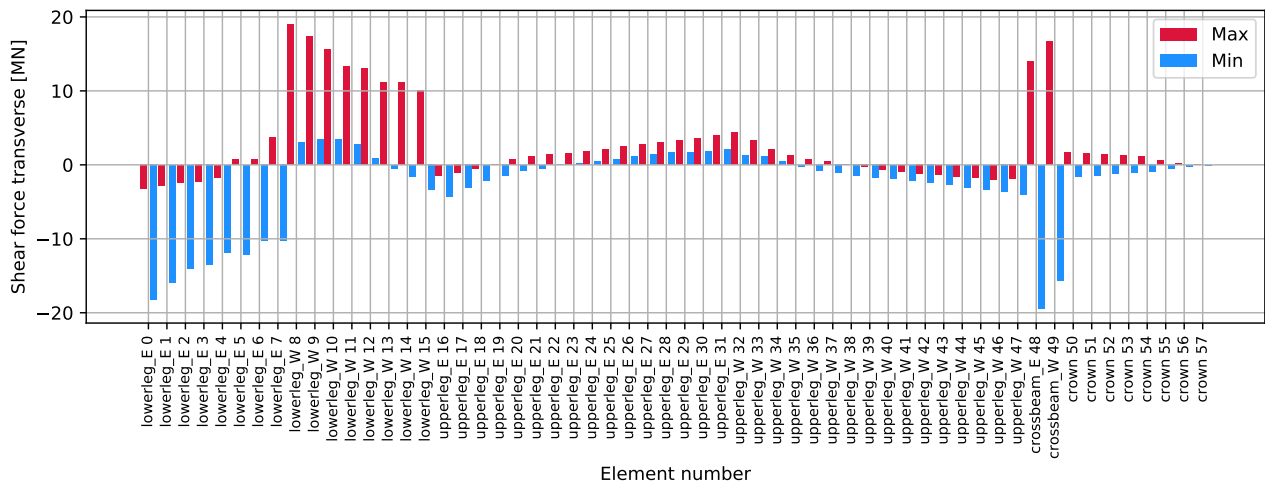
Figure 4.993: DH A39-A40 180deg - tower: Shear force transverse [MN]
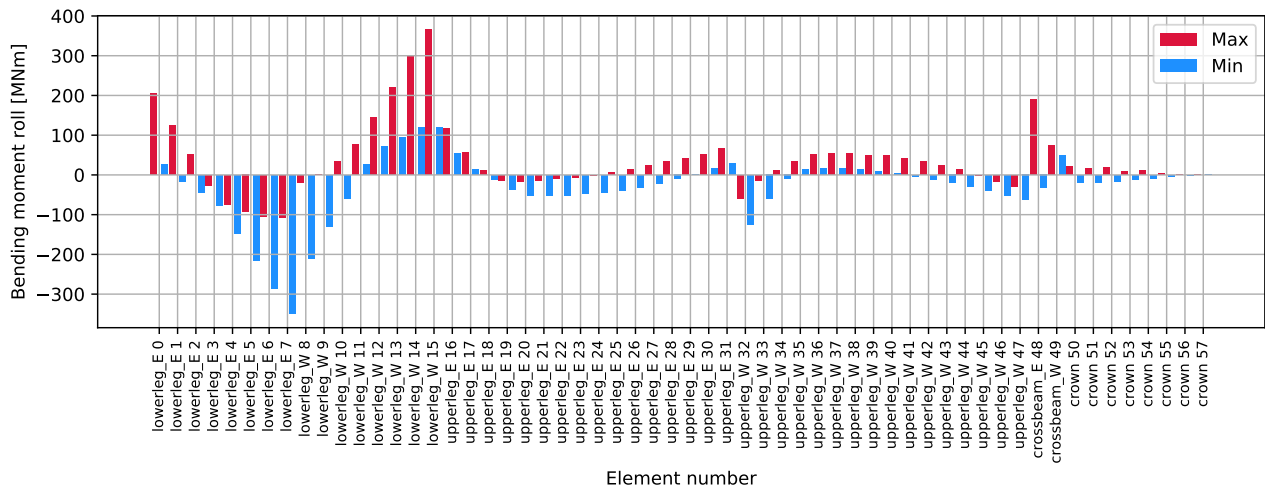
Figure 4.994: DH A39-A40 180deg - tower: Bending moment roll [MNm]
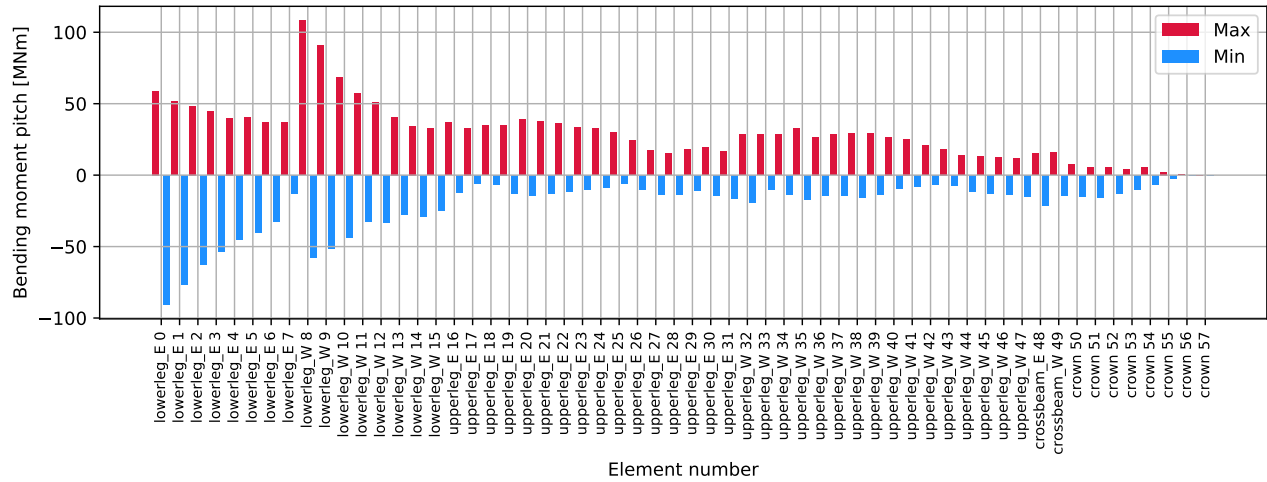
Figure 4.995: DH A39-A40 180deg - tower: Bending moment pitch [MNm]
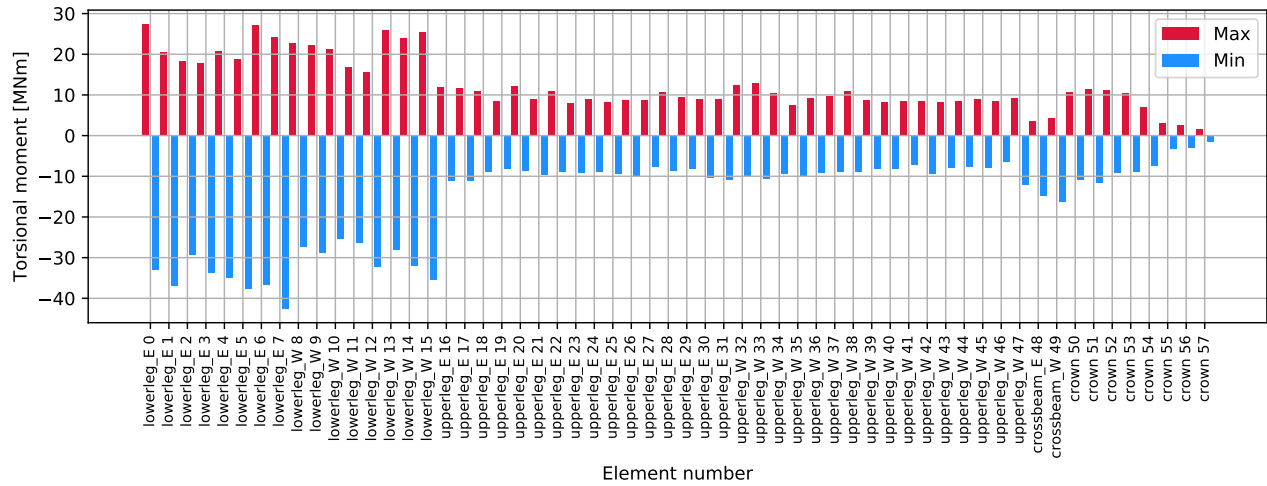
Figure 4.996: DH A39-A40 180deg - tower: Torsional moment [MNm]

4.22.3 Time series

Note : Time series are filtered using a Saviotzky-Golay filter for increased readability of the time history plots. Hence, maximum values that occur due to a rapid vibration are not shown in the plots. For maximum values, refer to the tabulated data.

All elements are numbered from South to North, bottom to top
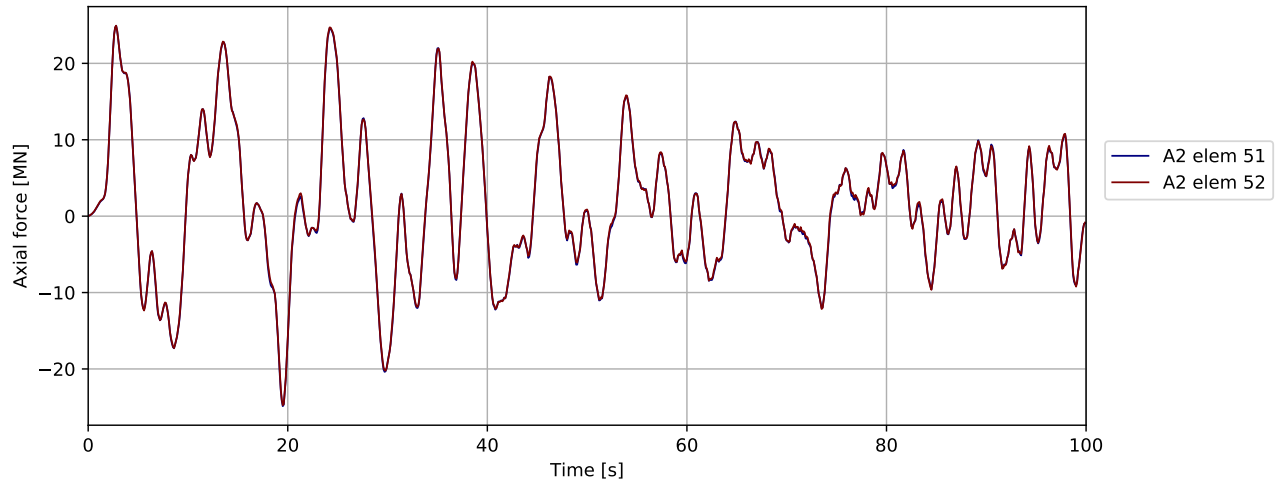
Figure 4.997: DH A39-A40 180deg - bridgegirder @ pylon: Axial force [MN]
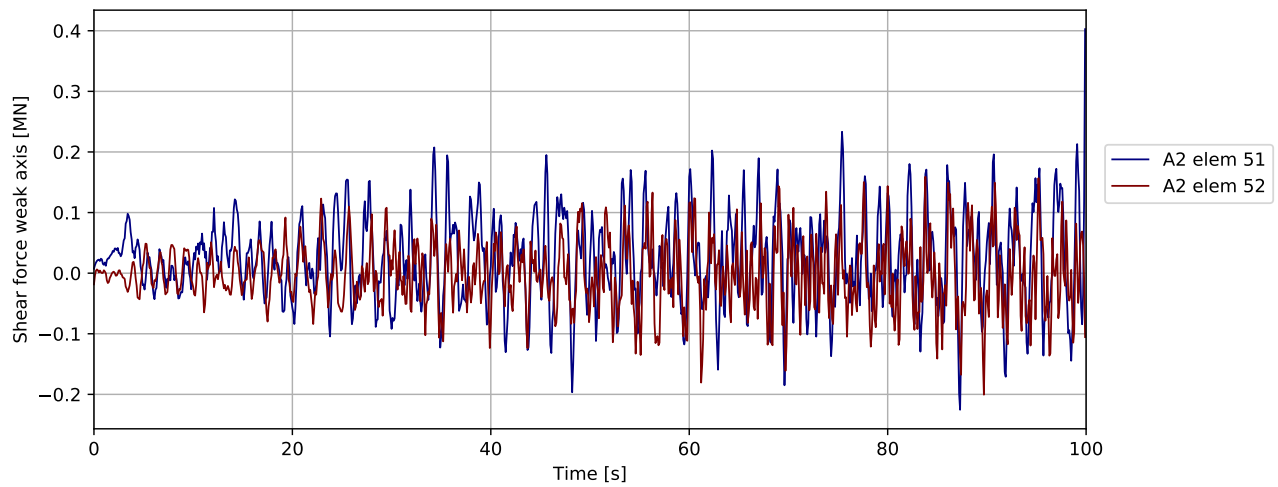
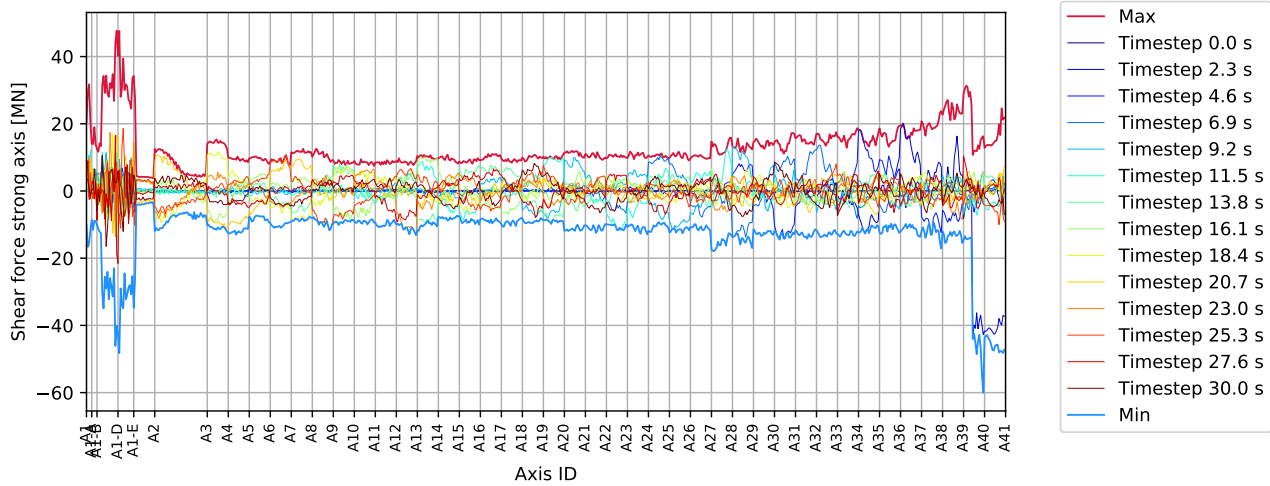Figure 4.998: DH A39-A40 180deg - bridgegirder @ pylon: Shear force weak axis [MN]
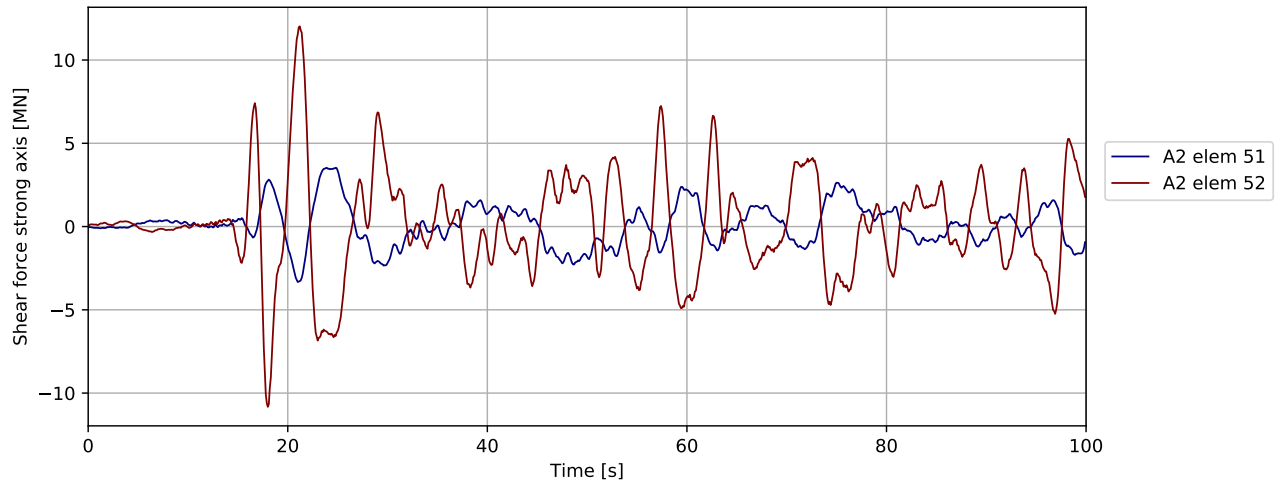
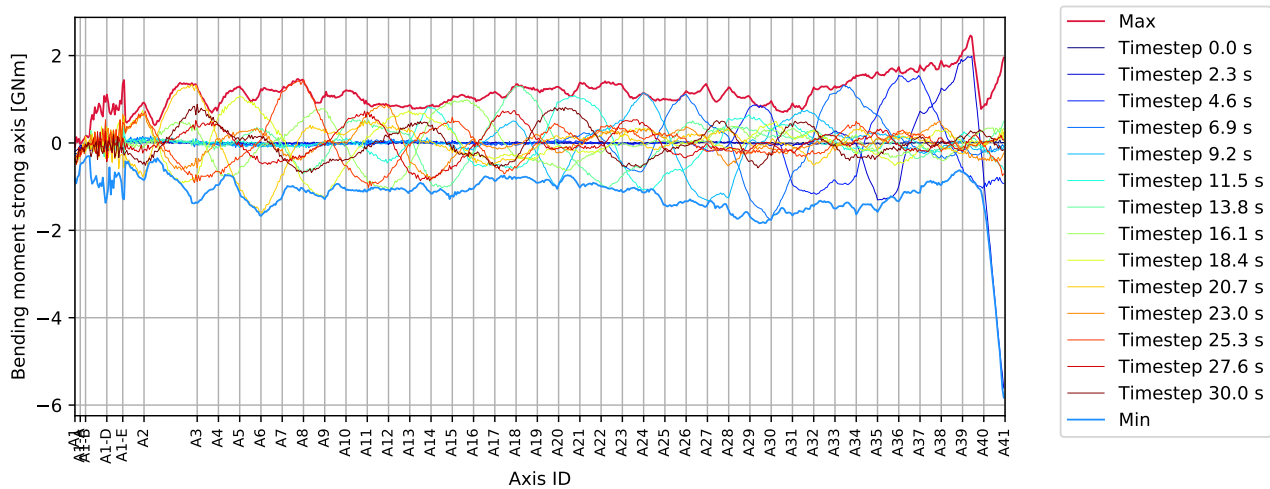Figure 4.999: DH A39-A40 180deg - bridgegirder @ pylon: Shear force strong axis [MN]
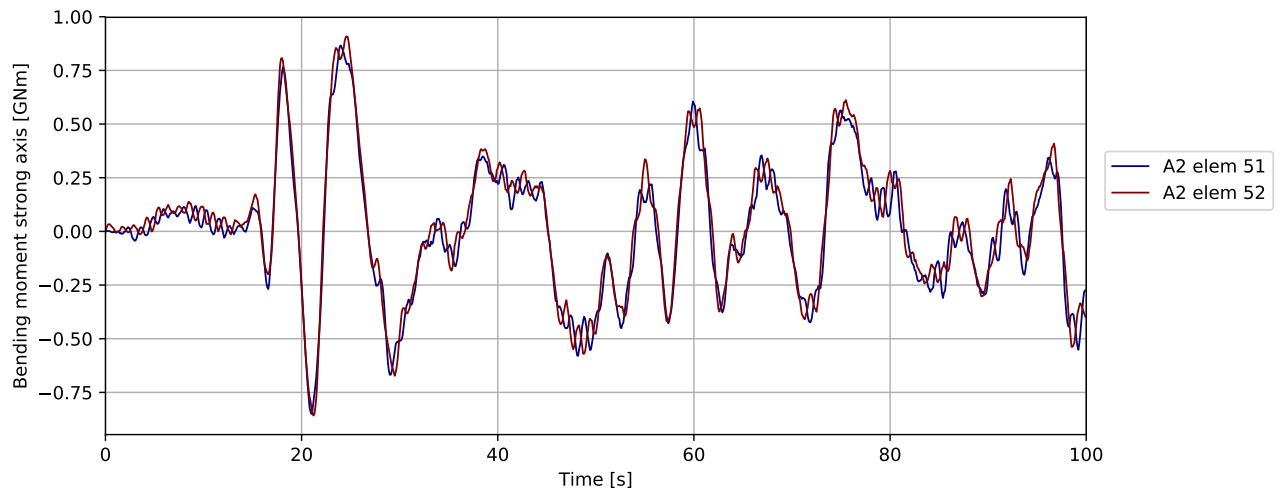
Figure 4.1000: DH A39-A40 180deg - bridgegirder @ pylon: Bending moment strong axis [GNm]
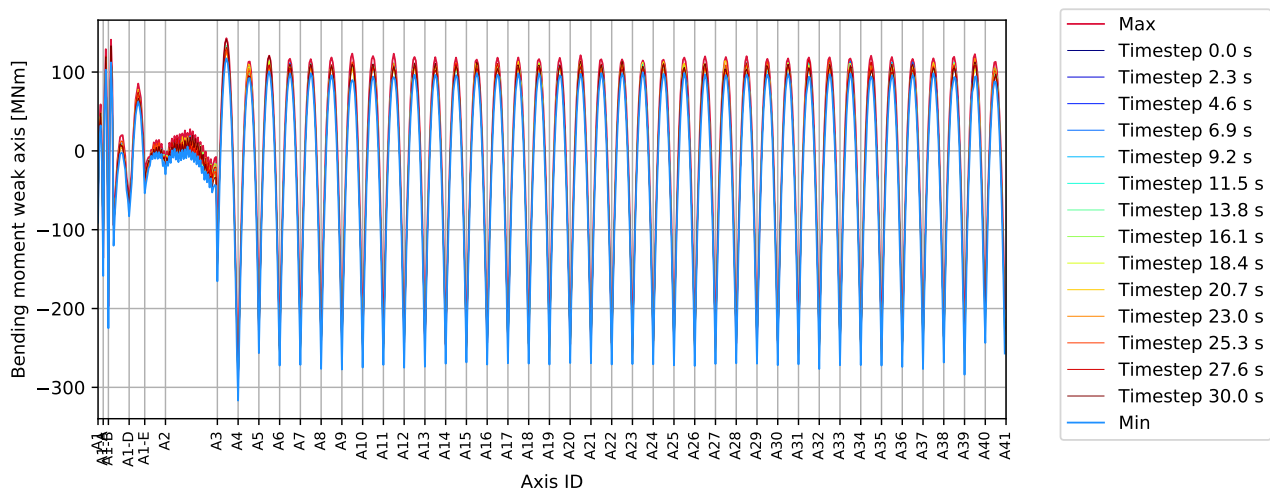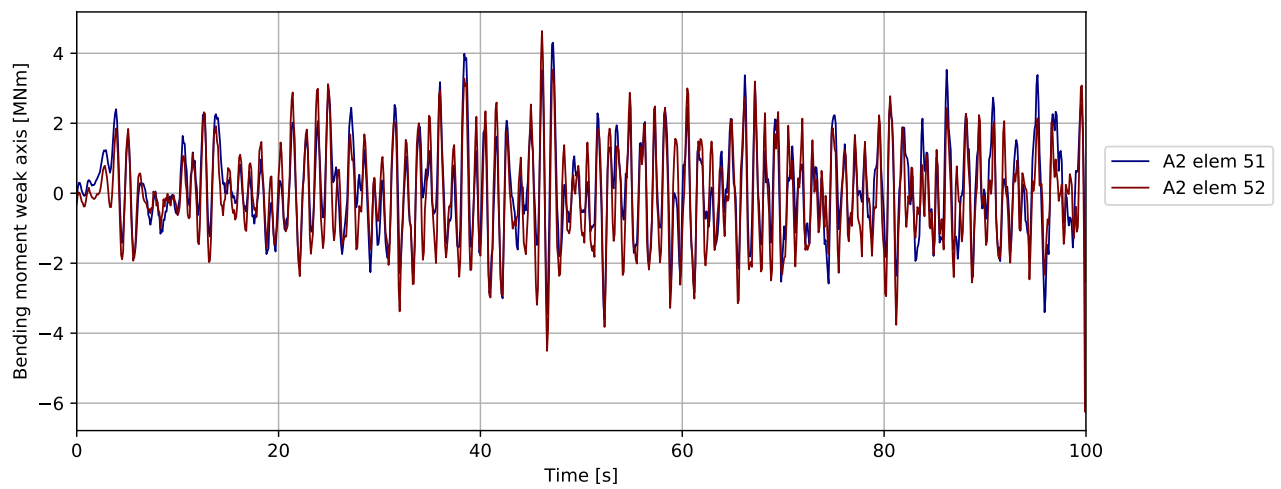

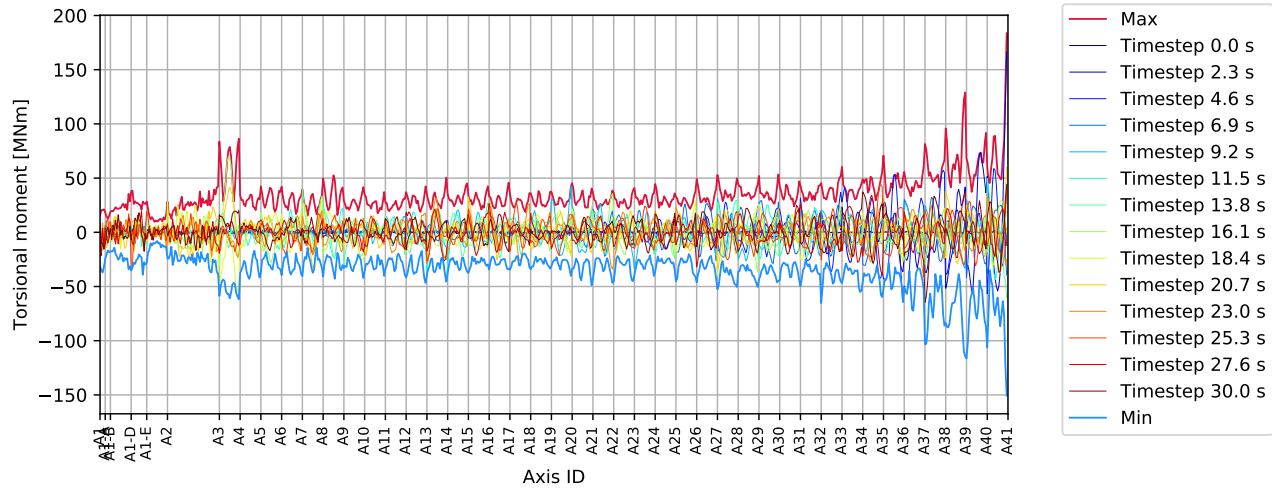Figure 4.1001: DH A39-A40 180deg - bridgegirder @ pylon: Bending moment weak axis [MNm]
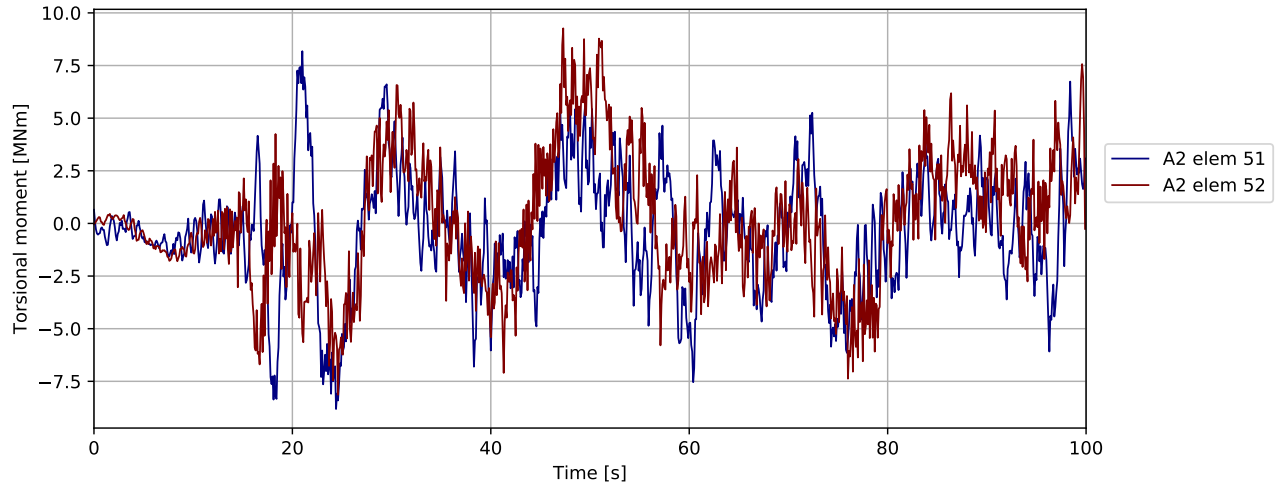
Figure 4.1002: DH A39-A40 180deg - bridgegirder @ pylon: Torsional moment [MNm]
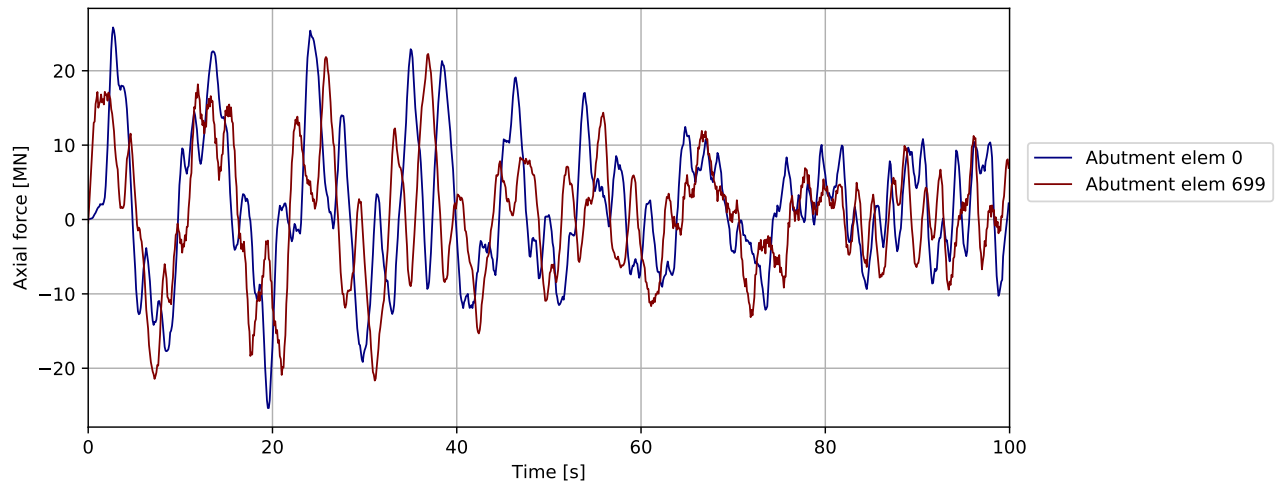
Figure 4.1003: DH A39-A40 180deg - bridgegirder @abutments: Axial force [MN]
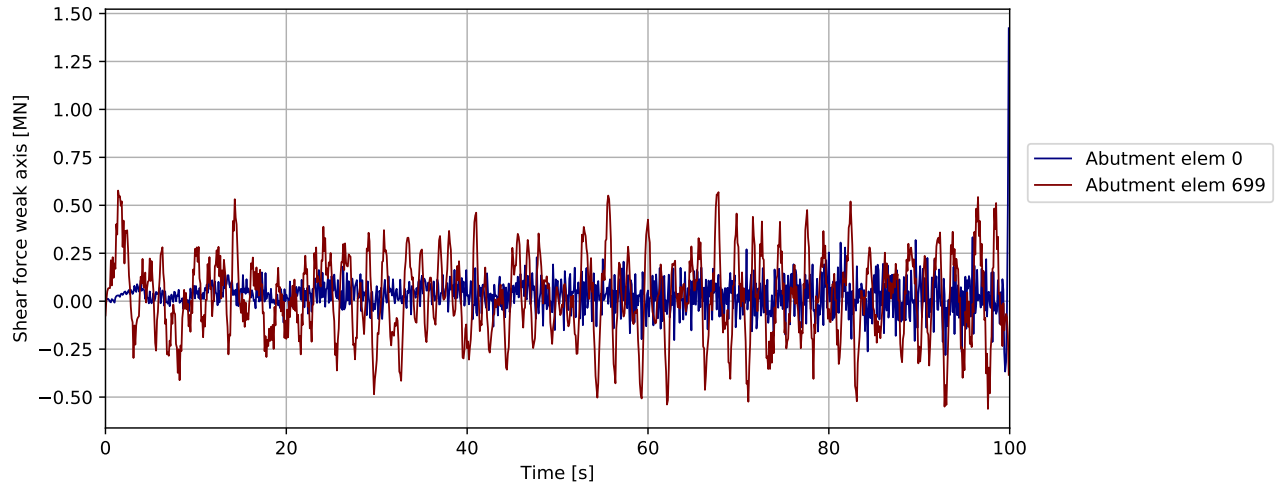
Figure 4.1004: DH A39-A40 180deg - bridgegirder @abutments: Shear force weak axis [MN]
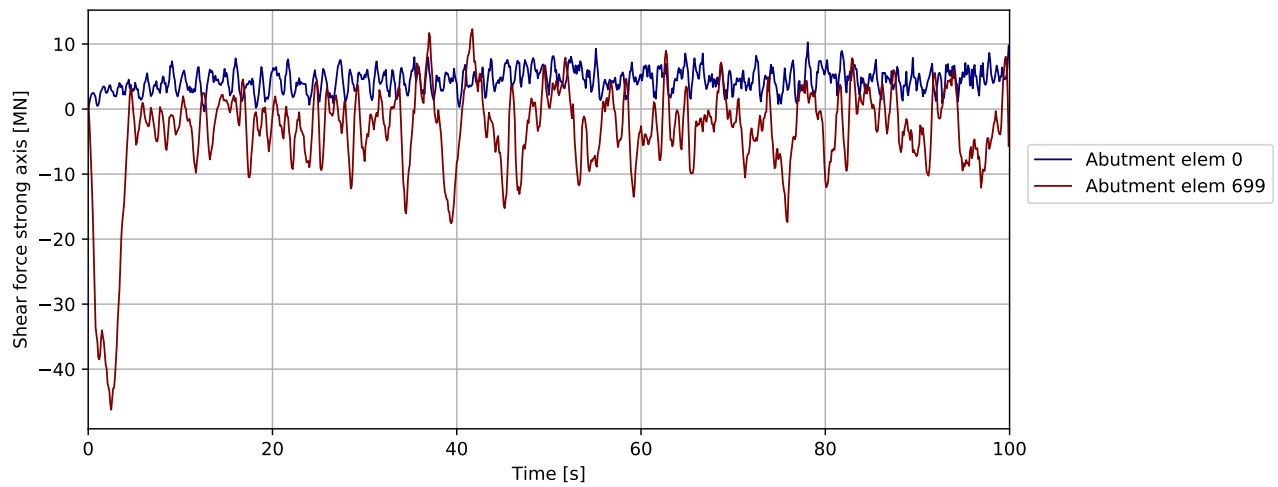
Figure 4.1005: DH A39-A40 180deg - bridgegirder @abutments: Shear force strong axis [MN]
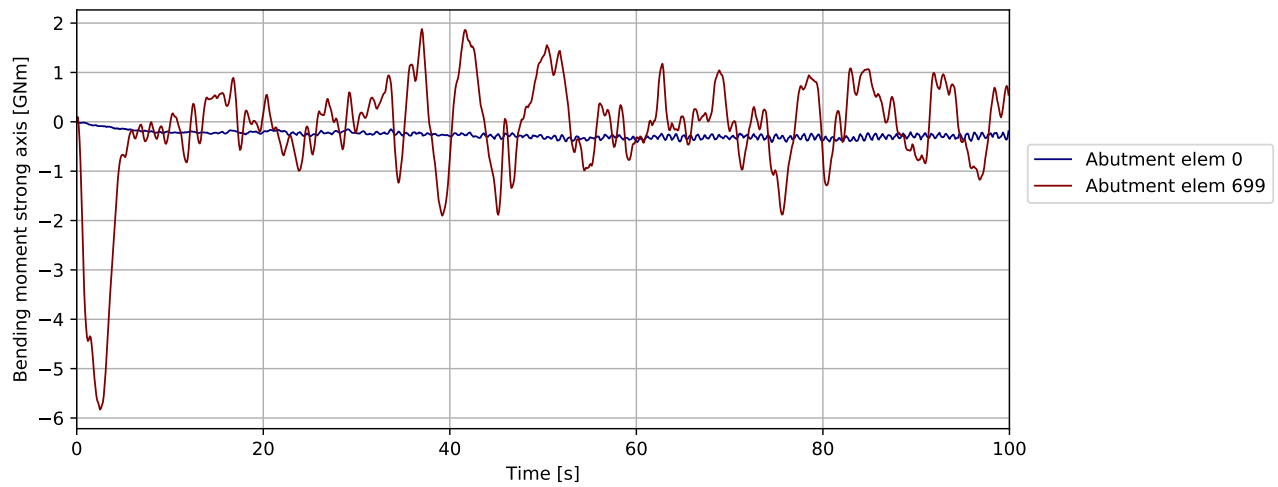
Figure 4.1006: DH A39-A40 180deg - bridgegirder @abutments: Bending moment strong axis [GNm]
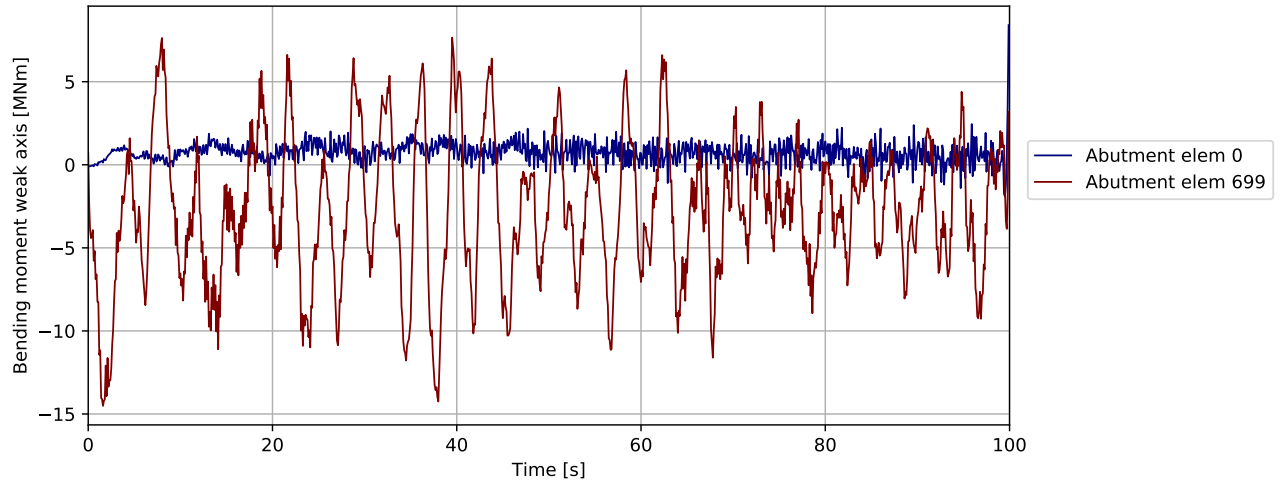
Figure 4.1007: DH A39-A40 180deg - bridgegirder @abutments: Bending moment weak axis [MNm]
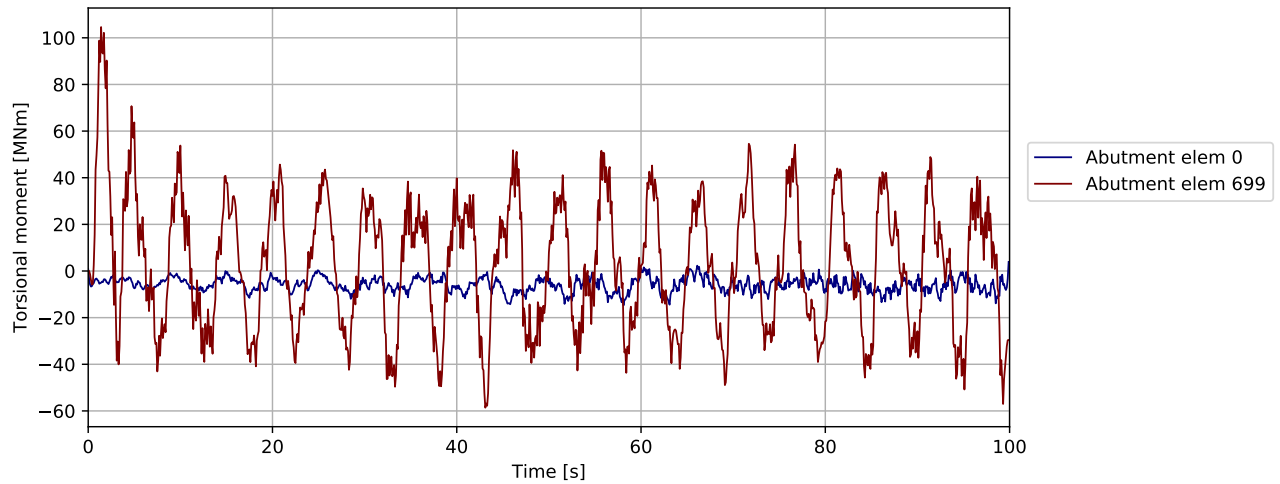
Figure 4.1008: DH A39-A40 180deg - bridgegirder @abutments: Torsional moment [MNm]

Note : Compressive spring force is negative
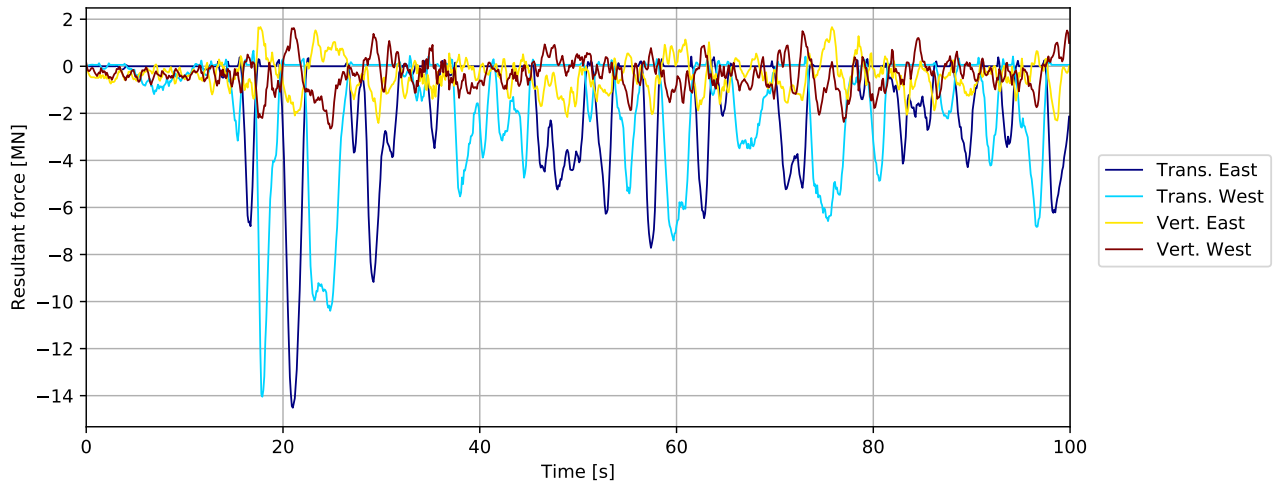
Figure 4.1009: DH A39-A40 180deg - bridgegirder supports in tower: Resultant force [MN]
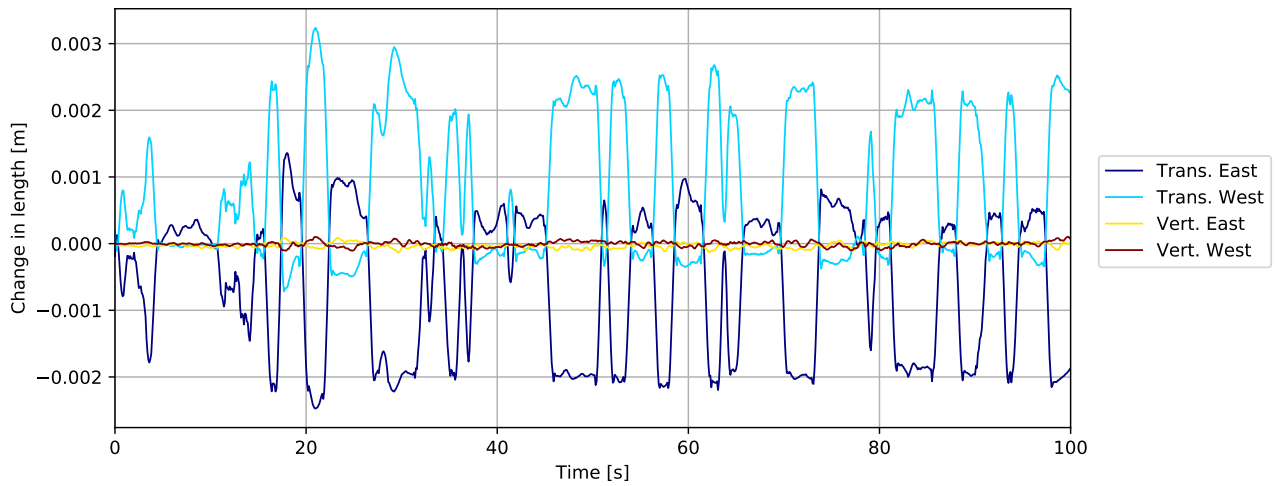
Figure 4.1010: DH A39-A40 180deg - bridgegirder supports in tower: Change in length [m]
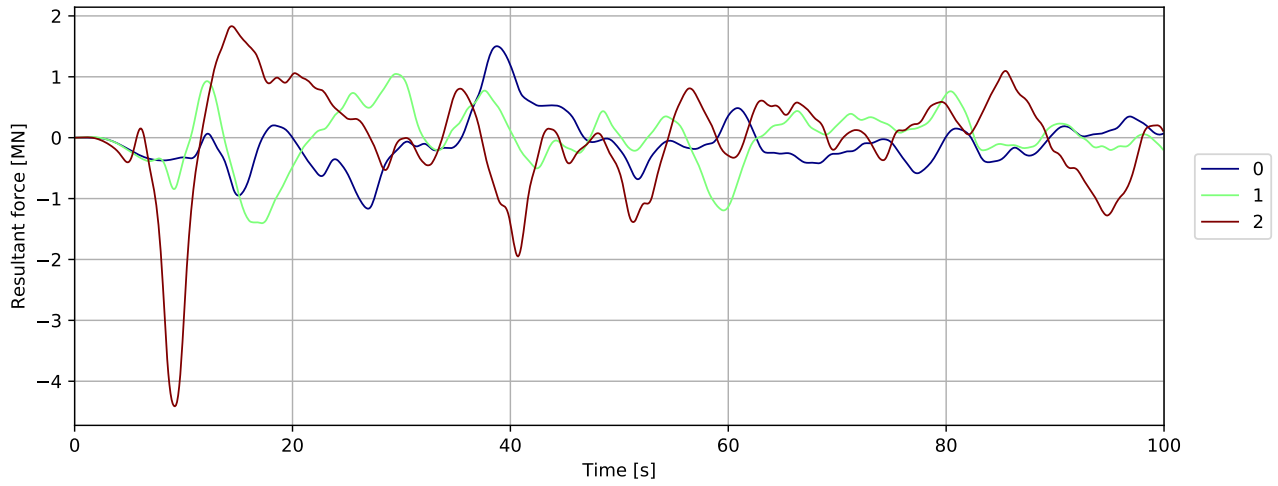
Figure 4.1011: Mooring force
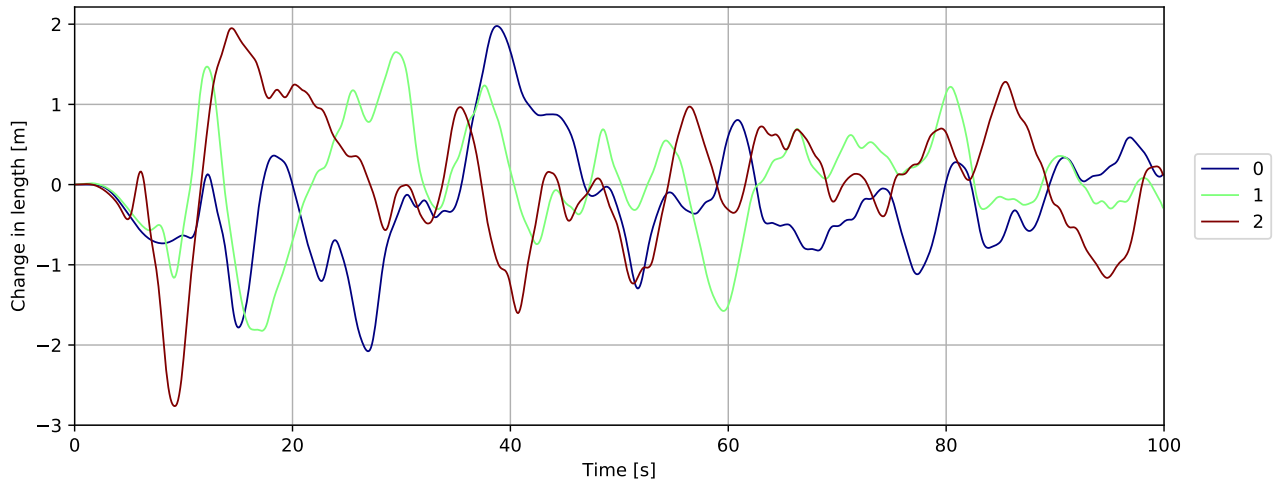
Figure 4.1012: Mooring displacement

References

[1] Lars Bjar. 10205546-12-NOT-065 : Mooring line damping. Technical report, 2019.

[2] Yanyan Sha, Ida Fagervik Osvoll, and Jørgen Amdahl. SBJ-30-C4-NTNU-27-RE-001 : Ship-pontoon collision analysis of the floating bridge concepts for Bjørnafjorden. Technical report, 2018.

[3] Martin Storheim. 10205546-11-NOT-018 : Initial global ship collision study. Technical report, 2019.

Concept development, floating bridge E39 Bjørnafjorden

Appendix J – Enclosure 2

10205546-11-NOT-076
Plastic capacity of column

MEMO

PROJECT	Concept development, floating bridge E39 Bjørnafjorden	DOCUMENT CODE	10205546-11-NOT-076
CLIENT	Statens vegvesen	ACCESSIBILITY	Restricted
SUBJECT	AMC status 2 - Plastic capacity of column	PROJECT MANAGER	Svein Erik Jakobsen
TO	Statens vegvesen	PREPARED BY	Andreas Landa / Martin Slagstad
COPY TO		RESPONSIBLE UNIT	AMC

SUMMARY

The plastic capacity of the column is investigated, and compared against the elastic capacities. It has been found that the short columns with a length of 11.5 m have plastic capacity well above the elastic capacity from shear forces and torsional moment experienced from ship collisions. A simplified capacity check of the longer column using the short column geometry has also been performed. The results show that the longer column at axis 3 must have a stockier geometry to ensure sufficient capacity. Note that the investigations are based on a model from phase 3 of the project. In addition, only one column model exists, hence all analyses are based on the similar column design.

1   Introduction and summary

The forces and moments from collisions between ships and the pontoon of the floating bridge have been found from the local collision analysis, ref. /4/. To make sure the global structural strength for the floating bridge is retained, the plastic capacity of the column has to be documented and compared against the elastic capacities. The plastic capacity of the column must be sufficient to prevent loss of a column and pontoon. It is also of interest to find the displacement of the column, since this will give an estimate on the level of buoyancy loss since the pontoon is pushed up and out of the water after a ship collision. A short and long column are investigated, however both are analysed using the cross-section for the short column from phase 3.

The non-linear analyses are run in LS-DYNA. Effort has been made to minimize the dynamic effects; hence, the level of kinetic energy in the analyses is as small as possible, i.e. a quasi-static analysis. This means that the aim is to keep the column from accelerating, and have the total energy being dominated by internal energy. Typically, the kinetic energy is kept <5% of the internal energy. This has been done by having a large load period. Note that the analyses are run using significant mass scaling in order to improve the analysis time step.

The plastic capacity is summarized in the table below.

0	29.03.2019	Status 2 issue	ALA/MSL	Rolf Magne Larssen	Svein Erik Jakobsen
REV.	DATE	DESCRIPTION	PREPARED BY	CHECKED BY	APPROVED BY

Table 1-1 Summary of capacities

Load	Short column [MN/MNm]		Long column [MN/MNm]	
	Elastic	Plastic	Elastic	Plastic
Shear force X	50MN	70MN	10MN	15MN
Shear force Y	60MN	70MN	-	-
Torsional moment	600MNm	800MN	-	-

2 Analysis setup

The element model is created in ANSYS and converted to a format that is compatible with LS-DYNA. The model consists of a column and the bridge girder, and is taken from phase 3 of the project. However, the results are assumed to be representative since the dimensions in phase 5 are similar or smaller than compared to the dimensions in phase 3.

2.1 Model

A beam with similar cross-section properties as the column is modelled at the bottom of the column. The load is applied at the bottom end node of the beam, and transferred to the rest of the model by including the bottom part of the column in a multiple constraint nodal set. The model is restrained by fixing the aft and forward part of the bridge girder. The model is shown in *Figure 2-1* below. A close up picture of the beam element where the load is applied is shown in *Figure 2-2*.
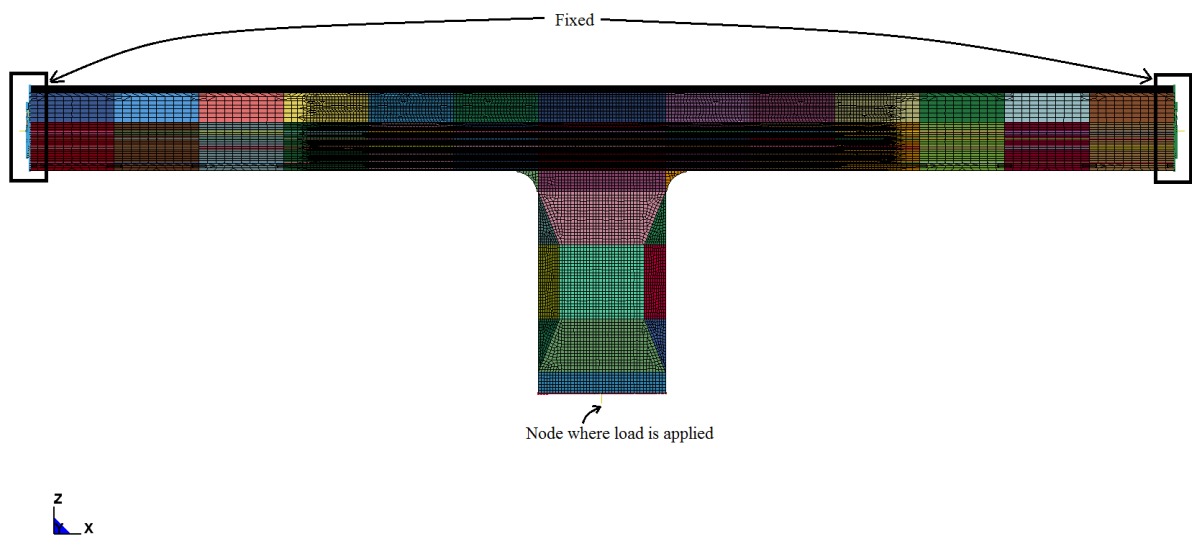
Figure 2-1 Model with mesh taken from LS-DYNA
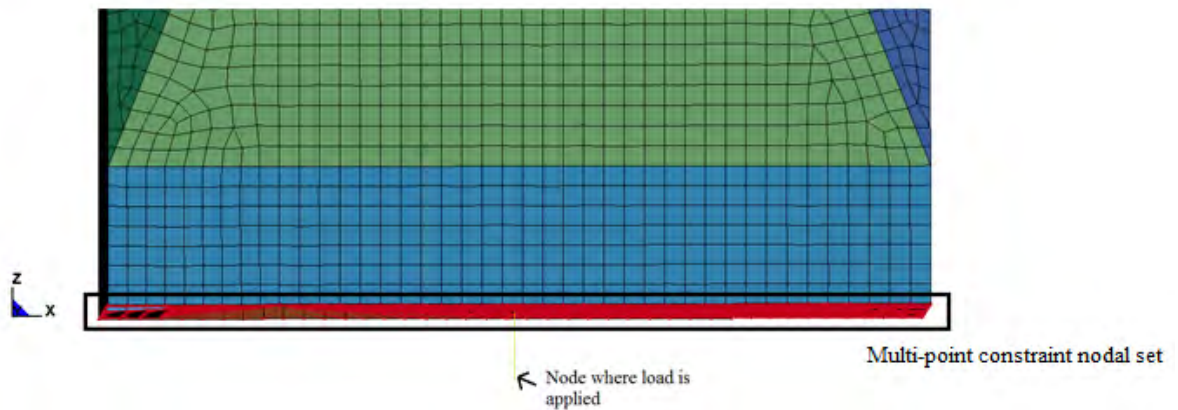
Figure 2-2 Beam element connected to multi-point constraint nodal set

Two column lengths are analysed; a short column and a long column. The long column is assumed to be 34m longer than the short column and is located at axis 3. This is modelled by extending the beam element shown in Figure 2-2 and keeping the cross-section properties equal to the column. Note that this will not give a correct estimate on the plastic capacity, since the longer column has a different cross-section compared to the shorter column. However, running a simple capacity check will provide useful input for the design of the intersection between the bridge girder and long column.

2.2   Materials

The stress-strain plot for the NV42 material used for the column and bridge girder is shown in *Figure 2-3* . For the beam element an elastic material with Young's modulus equal to $2.1 \cdot 10^{11}$ Pa is used.
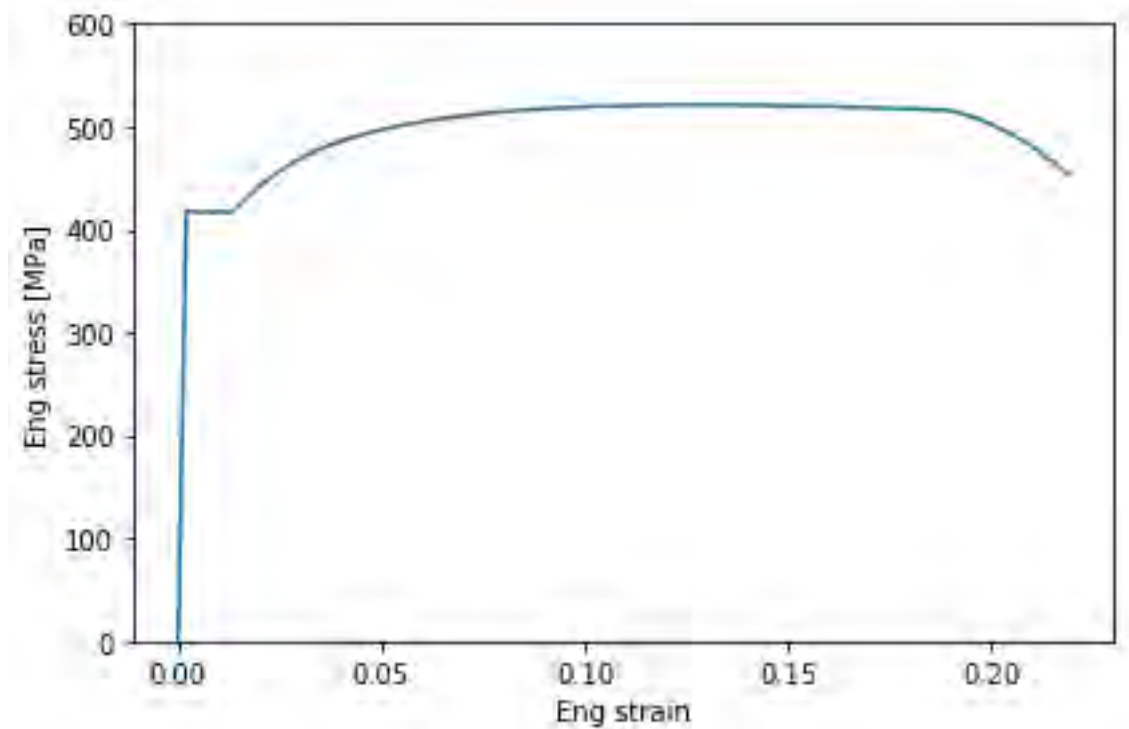
Figure 2-3 Stress-strain curve for S420 ALS lower bound material strength

2.3 Load input

To get an impression of the loads from a ship collision, the results from the global analysis is investigated. To get a conservative estimate, the loads applied in the analysis are somewhat higher compared to the results from the global analysis. Note that it is assumed that the higher column is 34m higher compared to the short column. The loads applied in the analysis are shown in Table 2-1. Note that the x-axis corresponds to the longitudinal axis of the bridge, and the y-axis is the transverse axis of the bridge

Table 2-1 Loads applied in plastic capacity check

Load	High column [MN/MNm]	Short column [MN/MNm]
Shear force X	100	100
Shear force Y	100	100
Torsional moment	1000	1000

The load curve showing the ramp up of load is shown in *Figure 2-4* below.
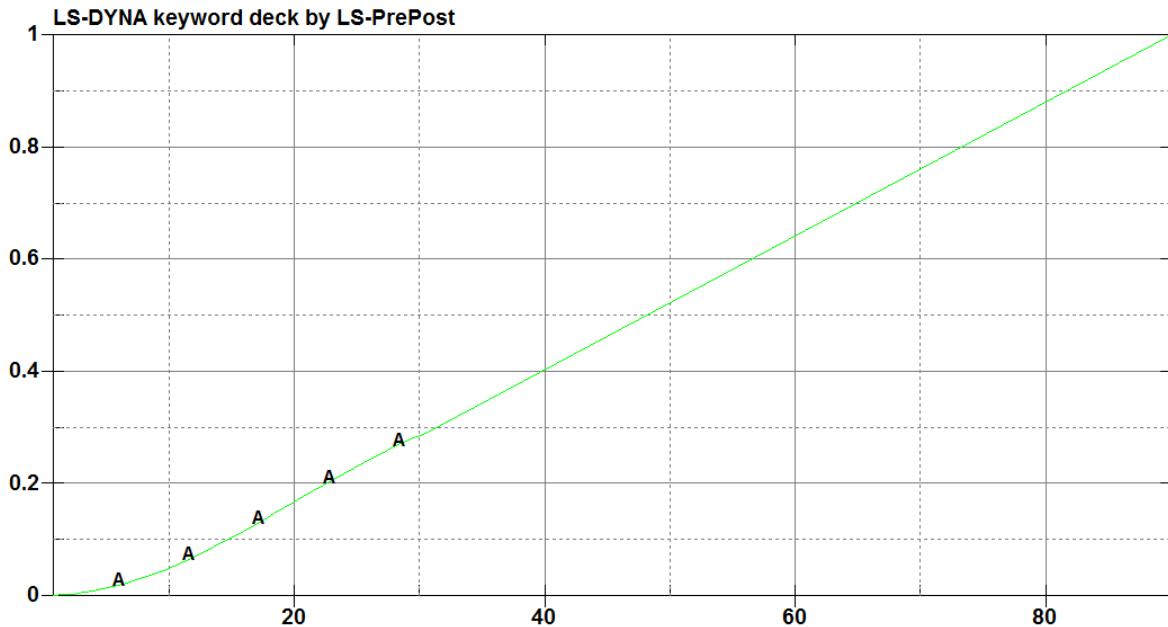
Figure 2-4 Load curve, time on x-axis

2.4 Section properties

A beam element is used to apply loads to the model. The properties for the beam element correspond to the sectional properties for the column, and are taken from the global analysis. The cross-sectional properties are shown in Table 2-2 below.

Table 2-2 Cross-sectional properties for column and bridge girder

	Cross sectional area, [m²]	Moment of inertia about transverse axis, [m⁴]	Moment of inertia about vertical axis, [m⁴]	Torsional constant [-]	Vertical shear area [m²]
Column	2.10	37.47	37.47	74.94	2.1000
Bridge girder	1.61	126.1	4.4474	9.36	0.0291

2.5 Imperfections

Imperfections are included by defining a harmonic curve for each panel using the perturbation option in LS-DYNA. The wave length is taken as two times the panel length, such that the imperfection curve corresponds to a half wave. The amplitude is calculated according to Table 1 in Chapter 2 Section 2.5 in DNVGL-OS-C401, ref. /2/, and is taken as 0.0015 times the panel length. The imperfections are combined according to *Figure 2-5* shown below. The sign combination of the amplitudes is assumed to be the most conservative way of combining the amplitude for the waves.
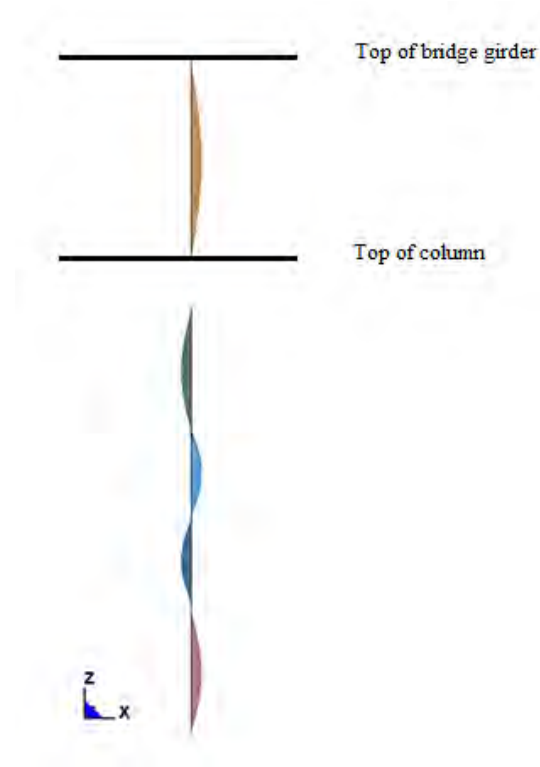
Figure 2-5 Imperfections in column and bulkhead in bridge girder bulkhead directly above column

The imperfections in the column is shown below in *Figure 2-6*. Note that that imperfection is, as shown in Figure 2-6, also included in the bridge girder.
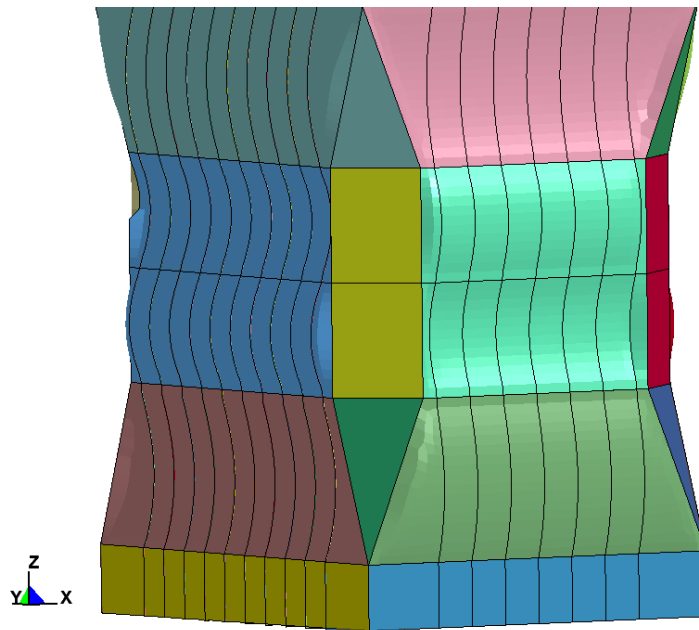
Figure 2-6 Imperfections in column, amplitude increased for visibility

3 Results

The results from the analyses are presented by plotting the section force (SEC) against the displacement. SEC is the sectional force for the end node on the beam element where the load is applied. The capacity is typically taken when the sectional force curve flattens and gets a significant drop.

3.1 Imperfection study

It is of interest to investigate the effect of including imperfections in the analysis. This is shown in Figure 3-1. It can be seen that the effect of imperfections on the capacity is negligible. Nevertheless, since the check below is only done for a case with shear force in longitudinal direction, imperfections are included in the analyses to mitigate the risk of being unconservative for other loads.
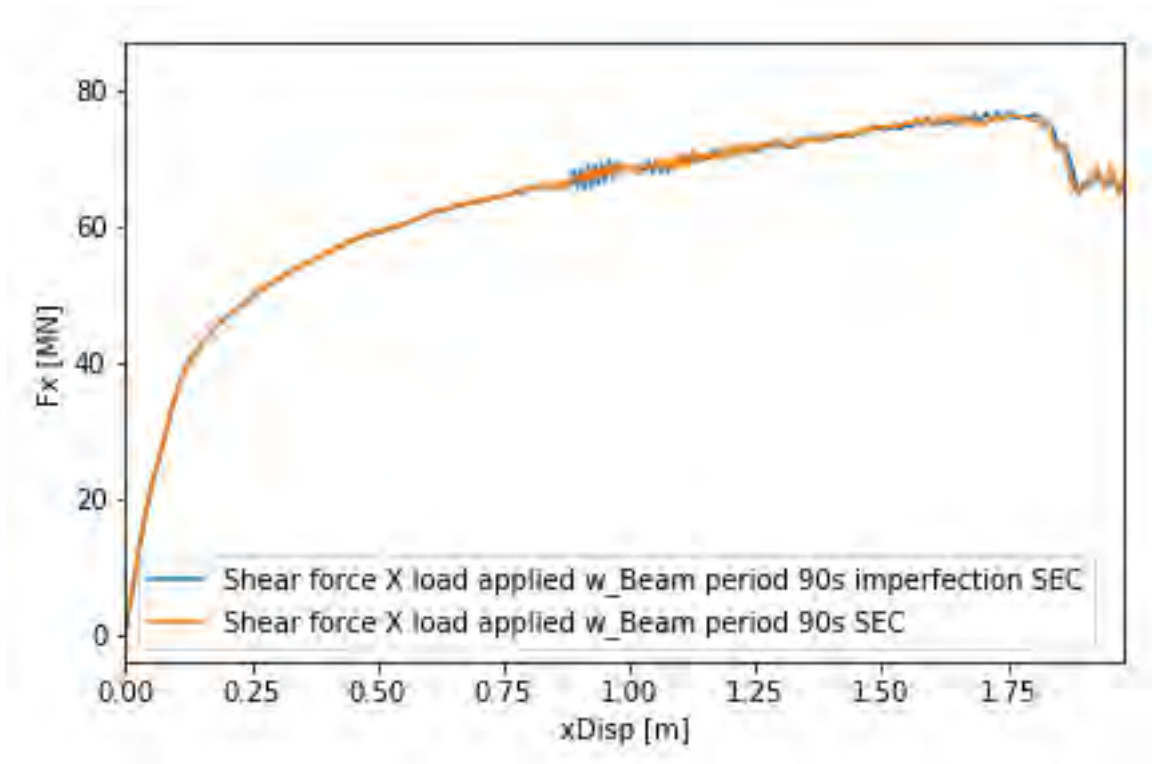
Figure 3-1 Force-displacement curves for analysis with and without imperfections

3.2 Short column

3.2.1 Shear force X

Figure 3-2 shows the model subjected to a shear force in the longitudinal direction. The deformation is not scaled, and is taken at the point at which a significant drop in the capacity is reached.

Figure 3-2 Model with shear force in x-direction, deformed model

Figure 3-3 shows the force-displacement curve for the node where the load is applied. Here, it can be seen that the plastic capacity is approximately 70MN. From the local collision analysis a maximum force from a "head-on" ship collision is 45MN, reference made to Section 3.2 in ref. /4/. Hence; it can be concluded that the phase 3 column has sufficient capacity against ship collisions from a shear force in longitudinal direction.
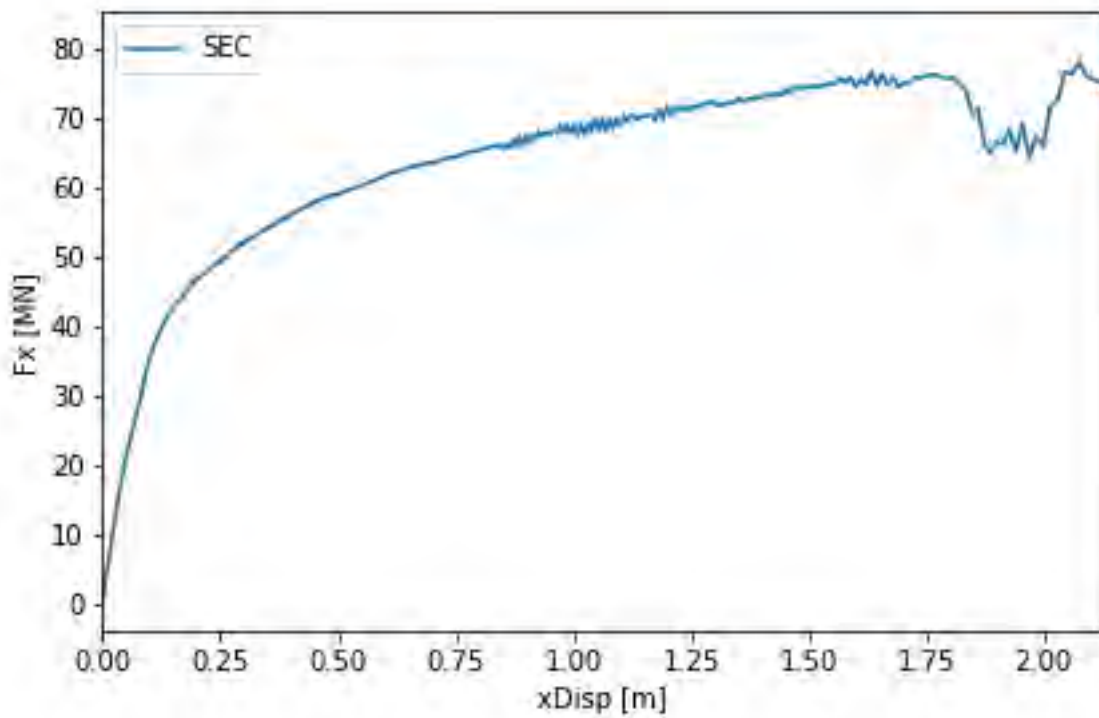
Figure 3-3 Force-displacement curve for short column with shear force in x-direction

Figure 3-4 to **Figure 3-6** shows the plastic strain in column and bridge girder at column intersection. **Figure 3-7** shows the effective stress. All plots are taken at the capacity limit.
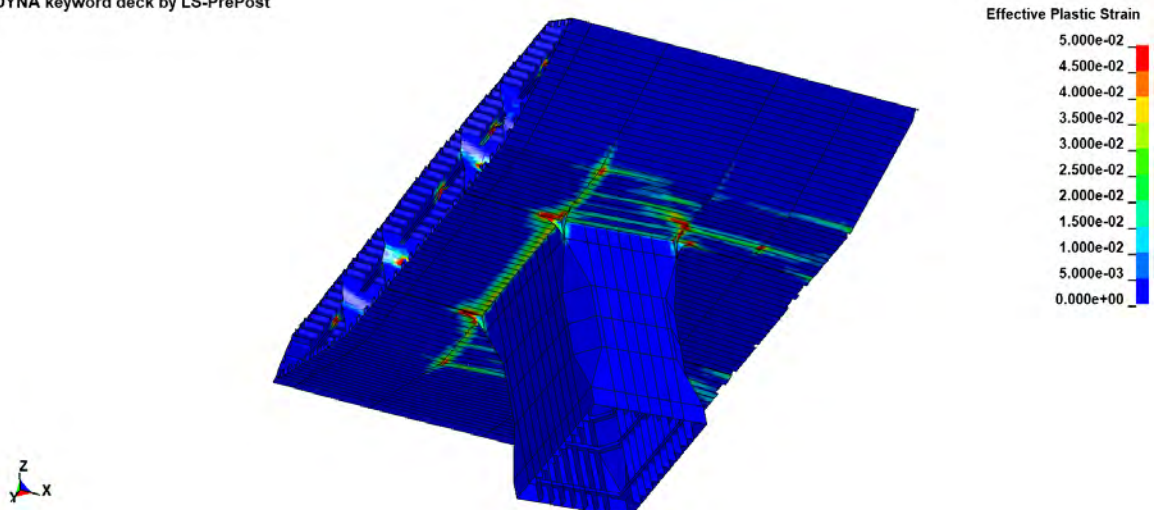
Figure 3-4 Plastic strain plot for short column with shear force in x-direction
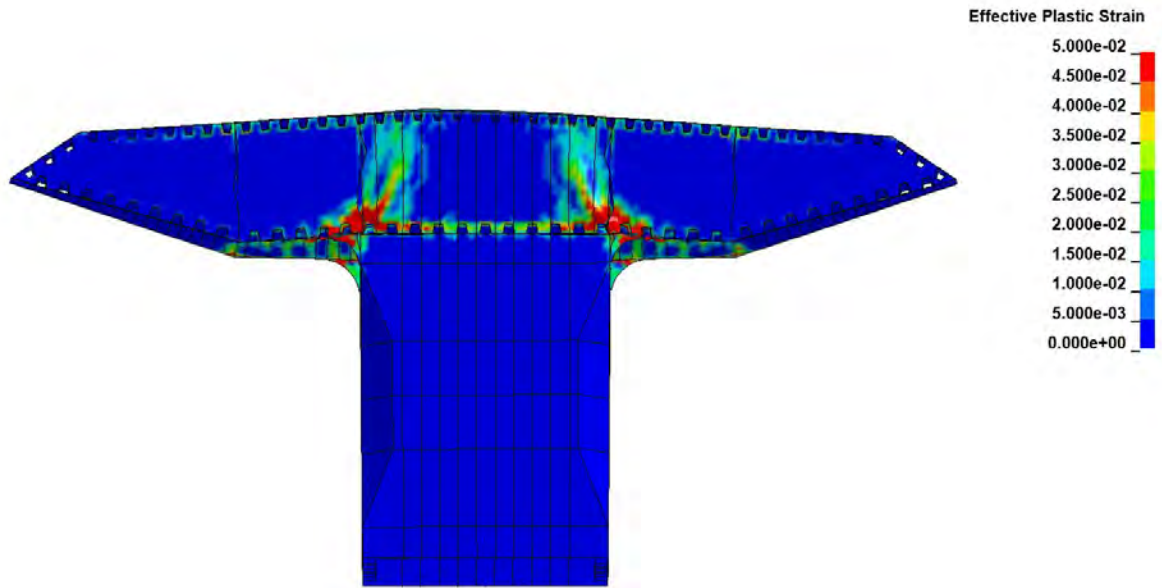
Figure 3-5 Plastic strain plot for short column with shear force in x-direction, bridge cross section at column interface shown, longitudinal section
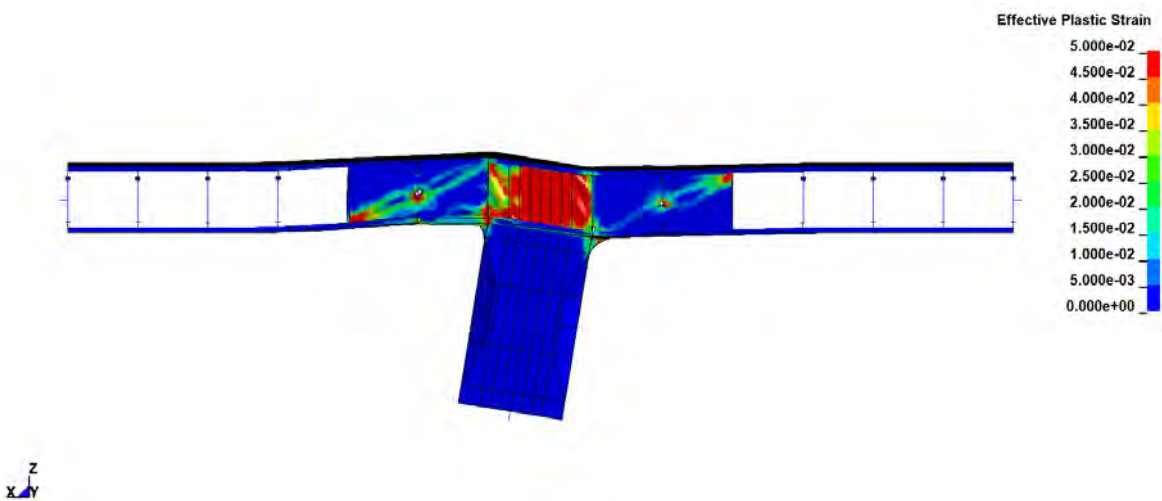
Figure 3-6 Plastic strain plot for short column with shear force in x-direction, bridge cross section at column interface shown, transverse section
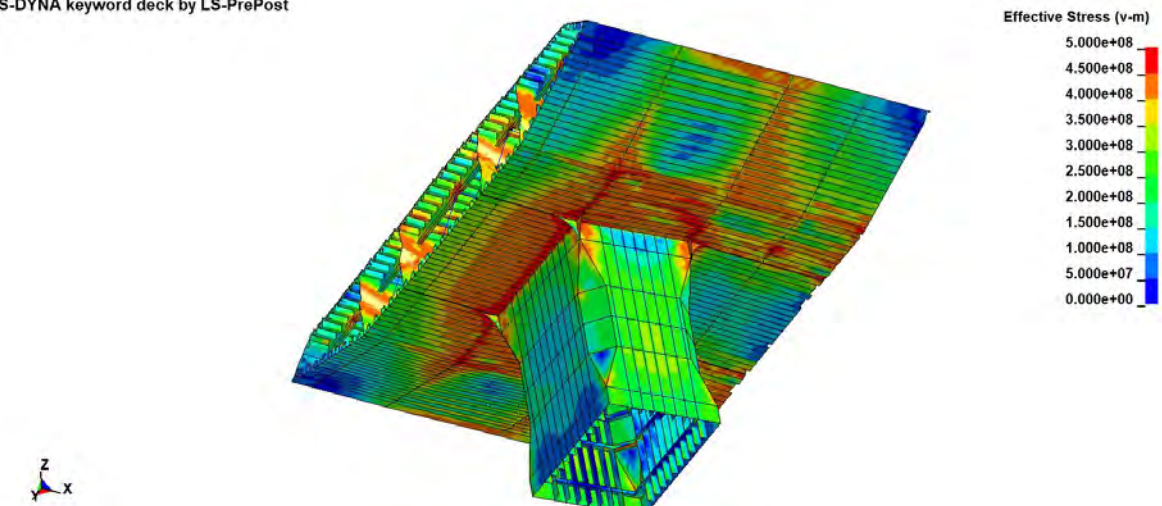
Figure 3-7 Effective stress plot for short column with shear force in x-direction

3.2.2   Shear force Y

Figure 3-8 show the deformed model subjected to a shear force in the transverse direction. The deformation is not scaled, and is taken at the time step where a significant drop in the capacity is reached.

Figure 3-8 Deformed model with shear force in y-direction

Figure 3-9 shows the force-displacement curve for the node where the load is applied. Here, it can be seen that the plastic capacity is approximately 70MN. From the local collision analysis a maximum force from a "head-on" ship collision is 25MN, reference made to Section 3.2 in ref. /4/. Hence; it can be concluded that the column has sufficient capacity against ship collisions from a shear force in transverse direction.

Figure 3-9 Force-displacement curve for short column with shear force in y-direction

Figure 3-10 to **Figure 3-12** shows the plastic strain in column and bridge girder at column intersection. **Figure 3-13** shows the effective stress. All plots are taken at the capacity limit.

Figure 3-10 Plastic strain plot for short column with shear force in y-direction

AMC status 2 - Plastic capacity of column

Figure 3-11 Plastic strain plot for short column with shear force in y-direction, bridge cross section at column intersection shown, longitudinal section
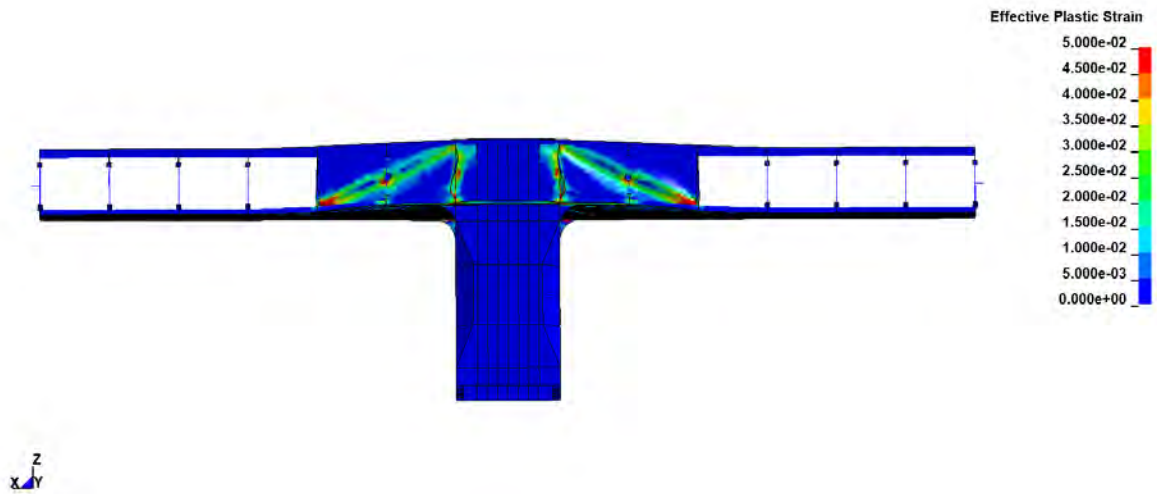
Figure 3-12 Plastic strain plot for short column with shear force in y-direction, bridge cross section at column intersection shown, transverse section
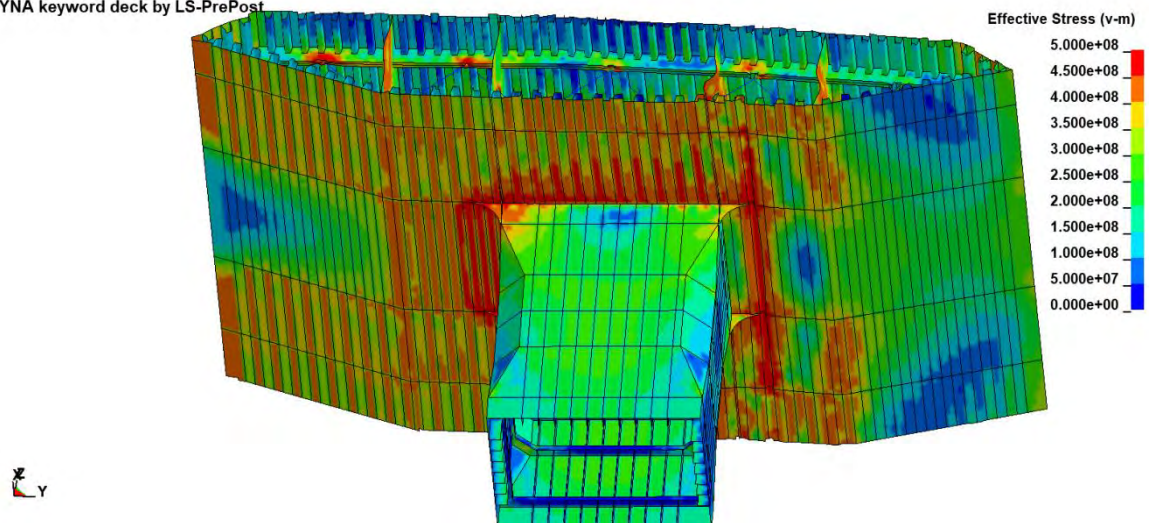
Figure 3-13 Effective stress plot for short column with shear force in y-direction

3.2.3 Torsional force

Figure 3-14 show the deformed model subjected to a torsional moment. The deformation is scaled by a factor of 2, and is taken at the time step where a significant drop in the capacity is reached. Note that imperfections included may not be relevant for the torsional moment case, and hence give unconservative results.
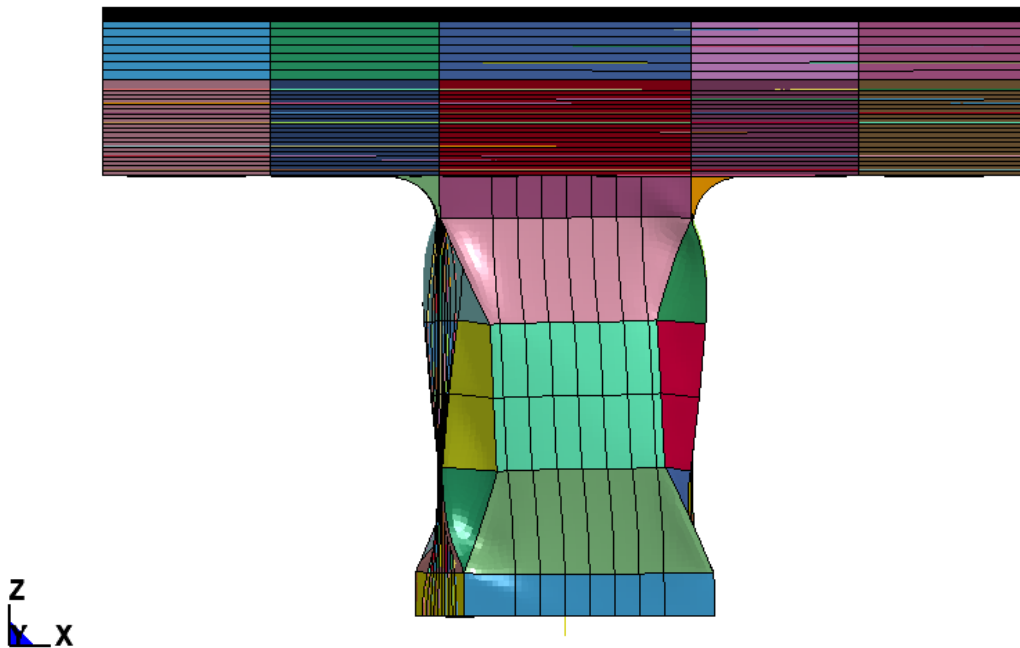
Figure 3-14 Deformed model for short column with torsional moment, deformation scaled with a factor of 2

Figure 3-15 shows the moment-rotation curve for the run with torsional moment. From the figure torsional capacity for the column can be taken as approximately 800MNm. From the local collision analysis a maximum force from a 90-degree ship collision is 30MN, reference made to Section 3.2 in ref. /4/. A collision with 90 degree angle with respect to the longitudinal axis of the pontoon, will give a torsional moment equal to:

$$T = F \cdot a = 30MNm \cdot \frac{53m}{2} \cong 800MNm$$

The moment arm is taken as half the length of the pontoon, reference made to Section 2.1 Table 2-1 in ref. /3/.
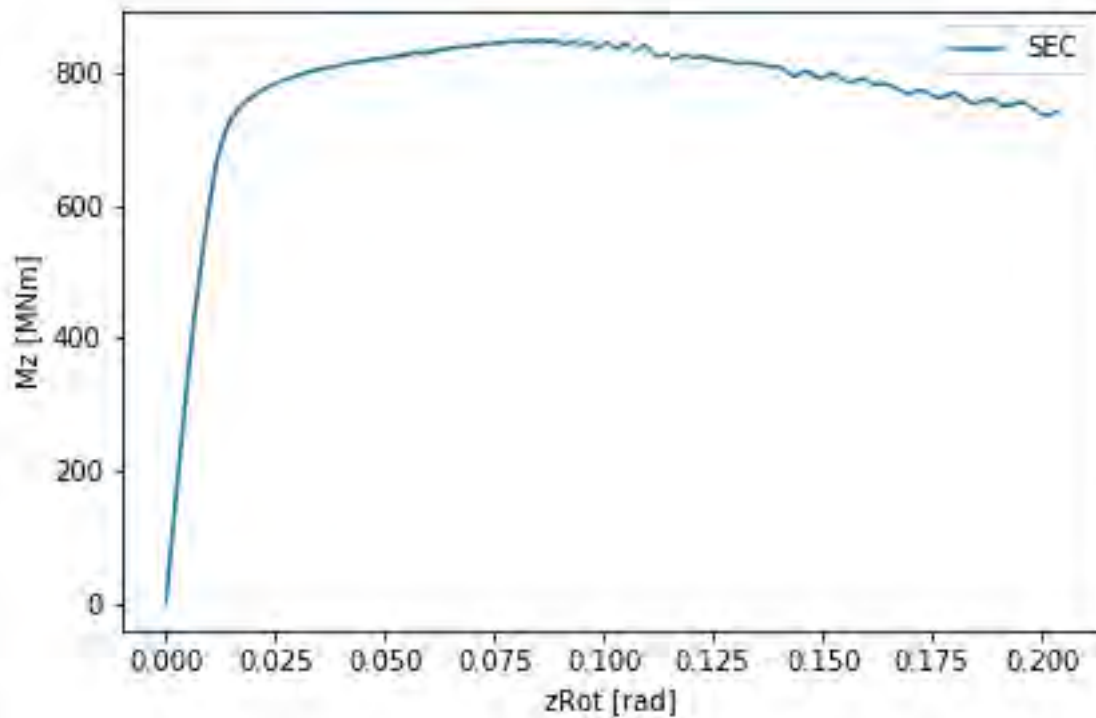
Figure 3-15 Moment-rotation curve for short column subjected to torsional moment

The torsional moment from the collision is approximately equal to the calculated capacity of the column. Hence; the results indicate that the torsional capacity of the column is sufficient, however with no or minor margins.

Figure 3-16 and *Figure 3-17* shows respectively the plastic strain and effective stress in the model at the time step when the capacity is reached.
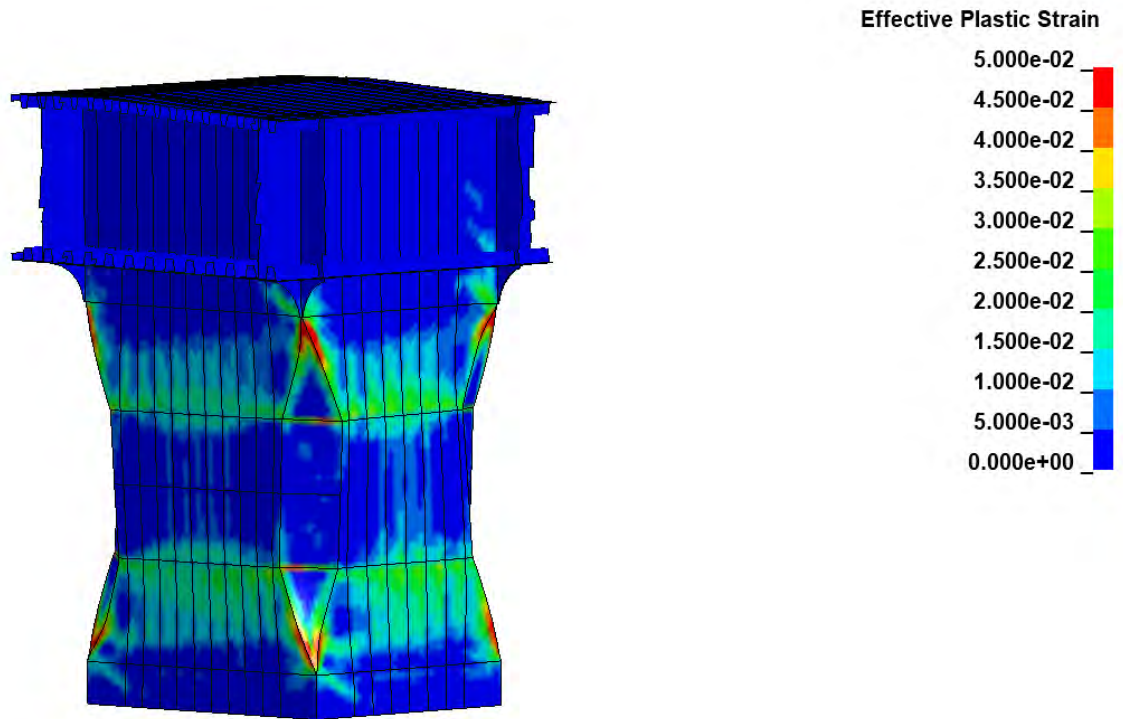
Figure 3-16 Plastic strain plot for short column with torsional moment
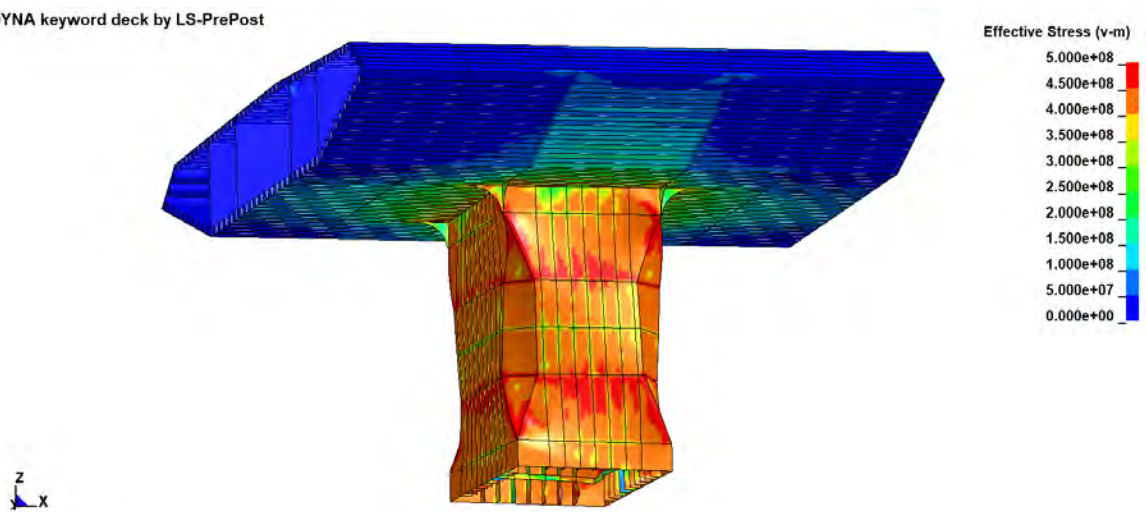
Figure 3-17 Effective stress plot for short column with torsional moment

3.3   Long column

3.3.1   Shear force X

Figure 3-18 show the model subjected to a shear force in the longitudinal direction. The deformation is not scaled, and is taken at the point where the capacity is reached.
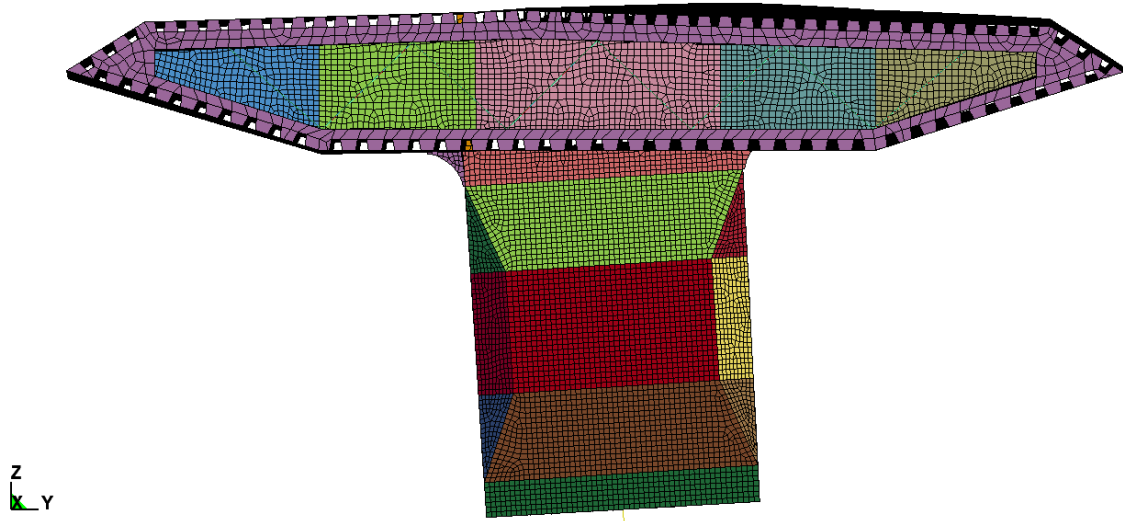
Figure 3-18 Model with shear force in x-direction, deformed model

Figure 3-19 show the force-displacement curve for the node where the load is applied. It is seen that the plastic capacity of the column/bridge girder intersection approximately 15MN. This is a significant reduction compared to the short column. From the local collision analysis a maximum force from a "head-on" ship collision is 45MN, reference made to Section 3.2 in ref. /4/. Hence; the long column does not have sufficient structural capacity with the current cross-section properties.
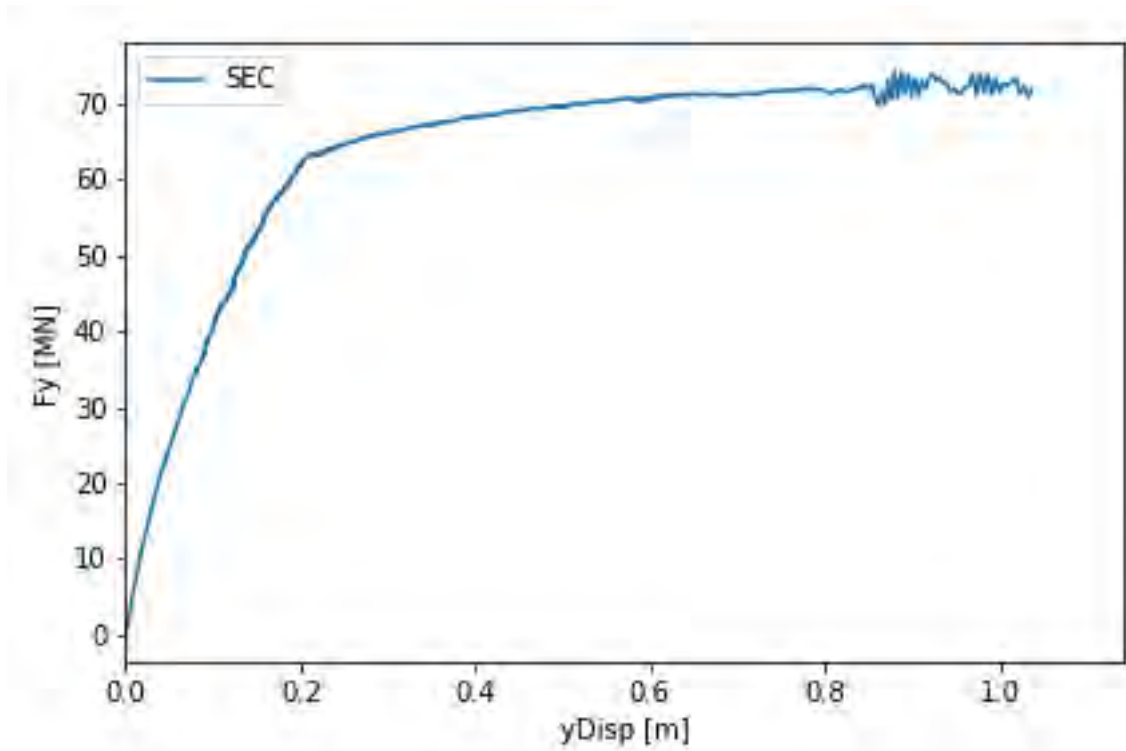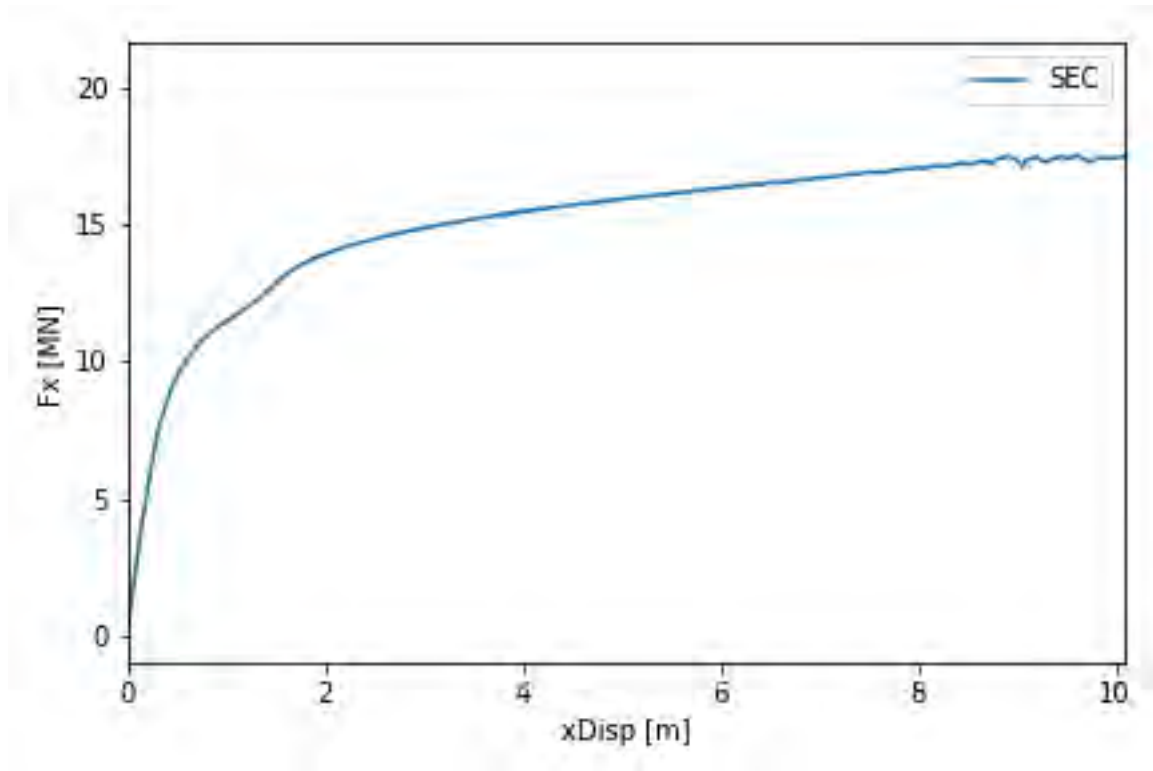

Figure 3-19 Force-displacement curve for long column with shear force in x-direction

Figure 3-20 to *Figure 3-22* shows the plastic strain in column and bridge girder at column intersection. *Figure 3-23* shows the effective stress. All plots are taken at the capacity limit.
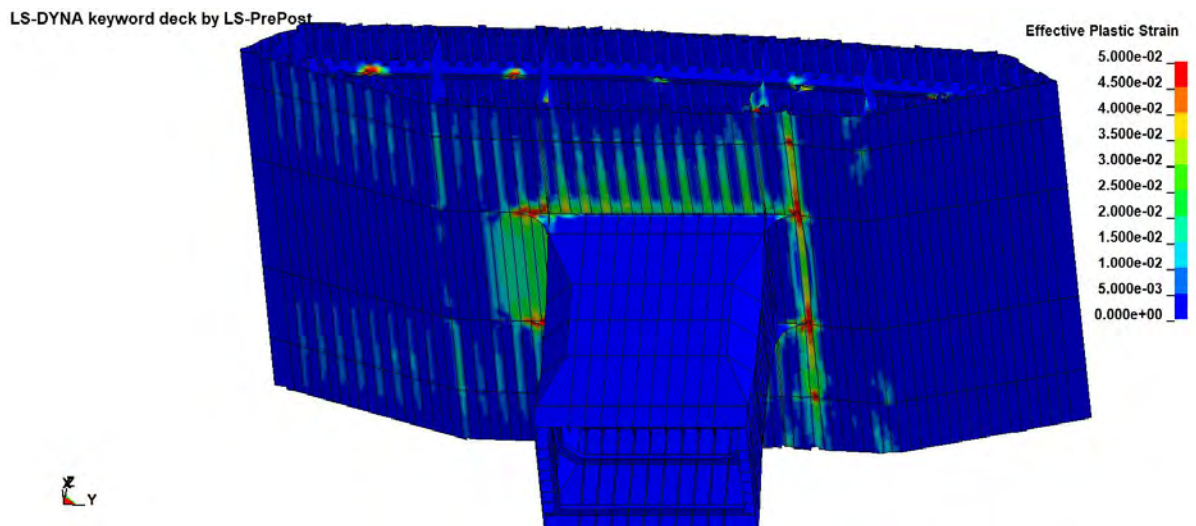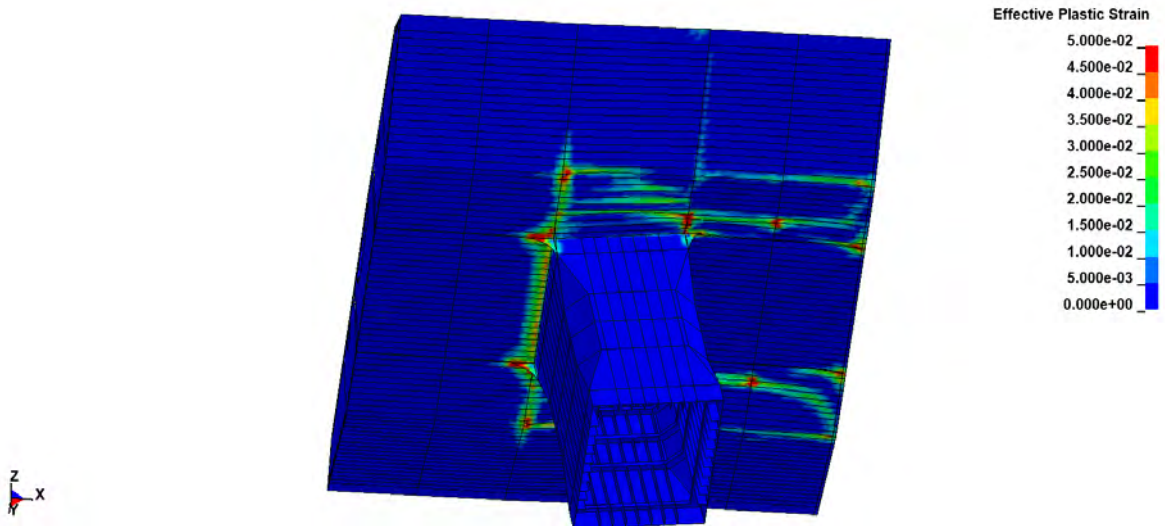
Figure 3-20 Plastic strain plot for long column with shear force in x-direction
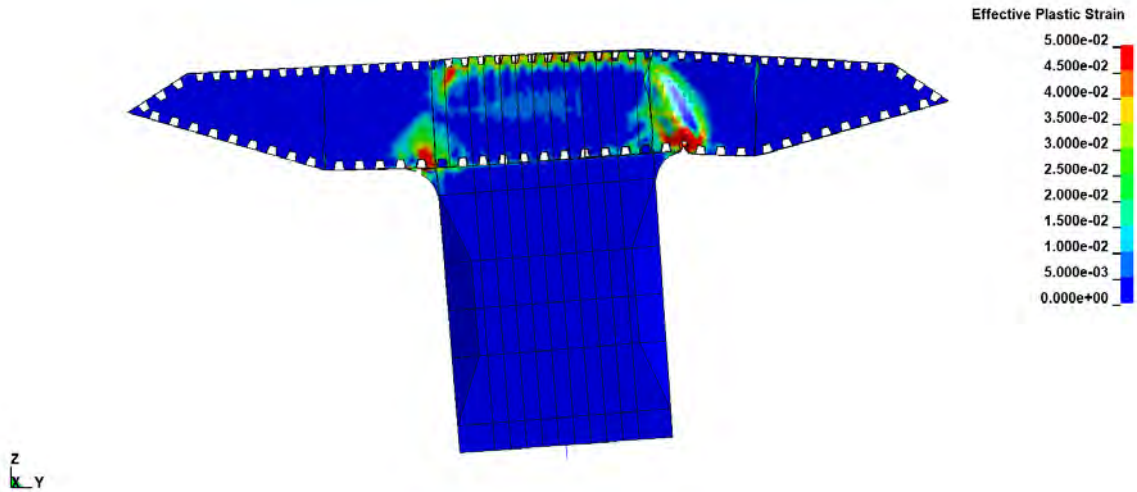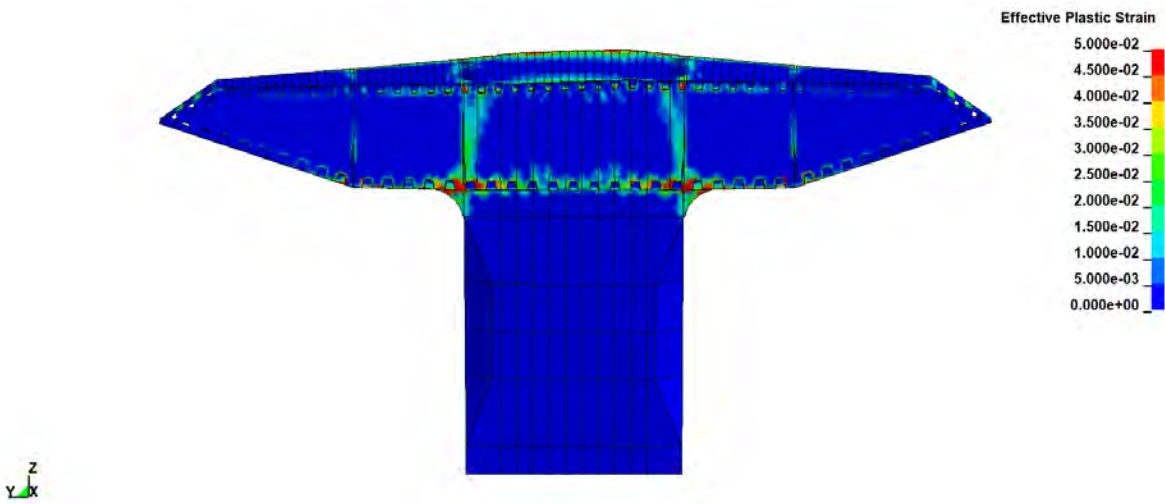

Figure 3-21 Plastic strain plot for long column with shear force in x-direction, longitudinal section
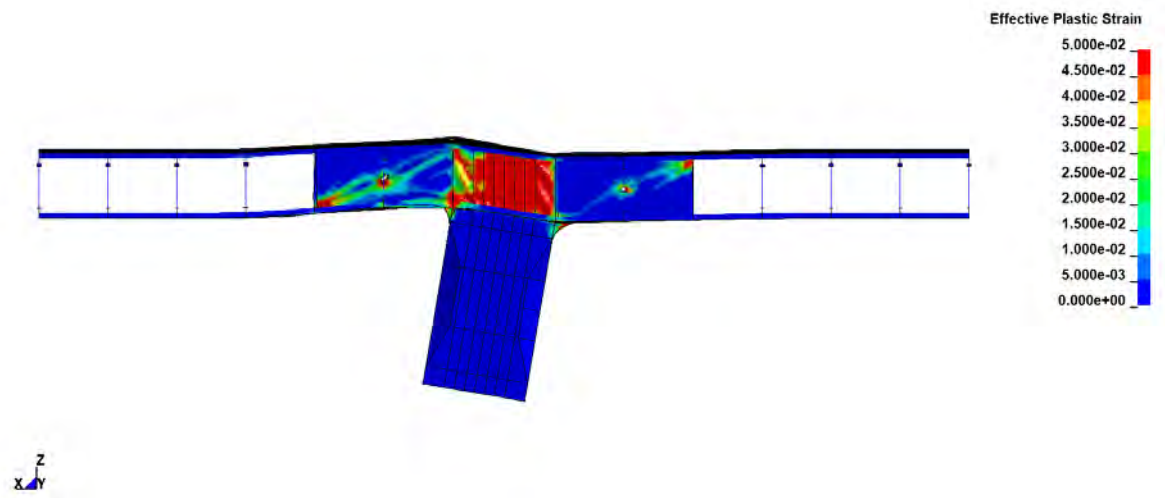
Figure 3-22 Plastic strain plot for long column with shear force in x-direction, transverse section
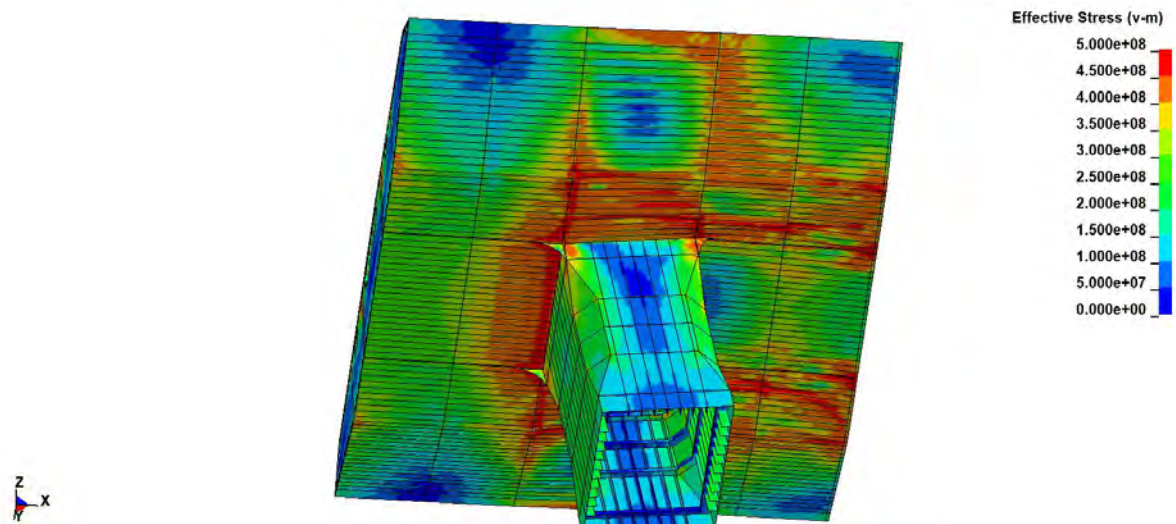
Figure 3-23 Effective stress plot for long column with shear force in x-direction

Note that the cross-section of the high columns will be increased significantly compared to the elongated version of the short type of columns as investigated here. As such, the capacity of the column/bridge girder intersection will be significantly increased compared to the results herein. However, due care should be taken to ensure that the plastic deformation of the intersection is not so large that a significant part of the pontoon is lifted out of water, thereby not causing a significant loss of buoyancy to the bridge system.

3.4 Verification of load application and total energy

The results are verified by plotting the sectional and reaction force against the displacement. The sectional force is taken from the beam element connected to the bottom of the column through a multi-point constraint nodal set. Effort has been made to ensure that the total energy is dominated by internal energy. One can conclude that the applied load is balanced by stiffness when the difference between the sectional force (SEC) and reaction forces (SPC) are small. The plastic capacity has been taken when the sectional force curve flattens.

Figure 3-24 and *Figure 3-25* shows a comparison of sectional and reaction forces for the case with shear force in x-direction and y-direction. From the plots it can be seen that internal energy dominates up until the sectional force curve flattens. This point is taken as the capacity limit. As time progresses it can be observed that the distance between the curves increases. This indicates increased level of kinetic energy, i.e. the column starts to accelerate and fracture of elements in the bridge girder-column intersection is observed.
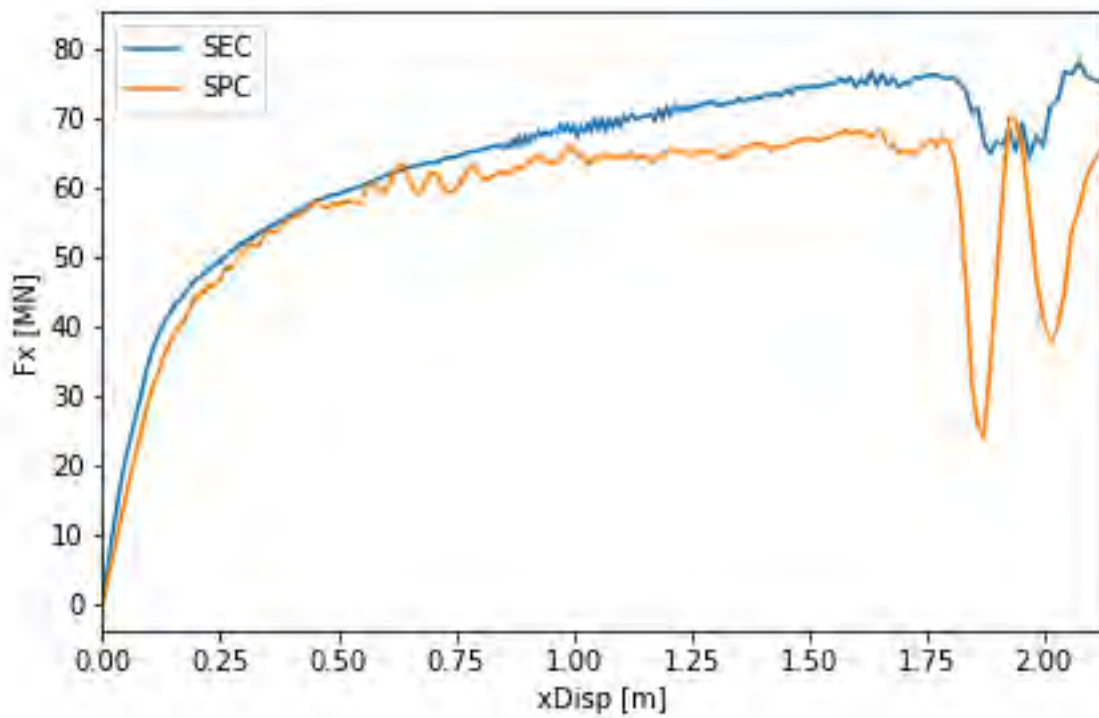
Figure 3-24 Force-displacement curve for short column with shear force in x-direction
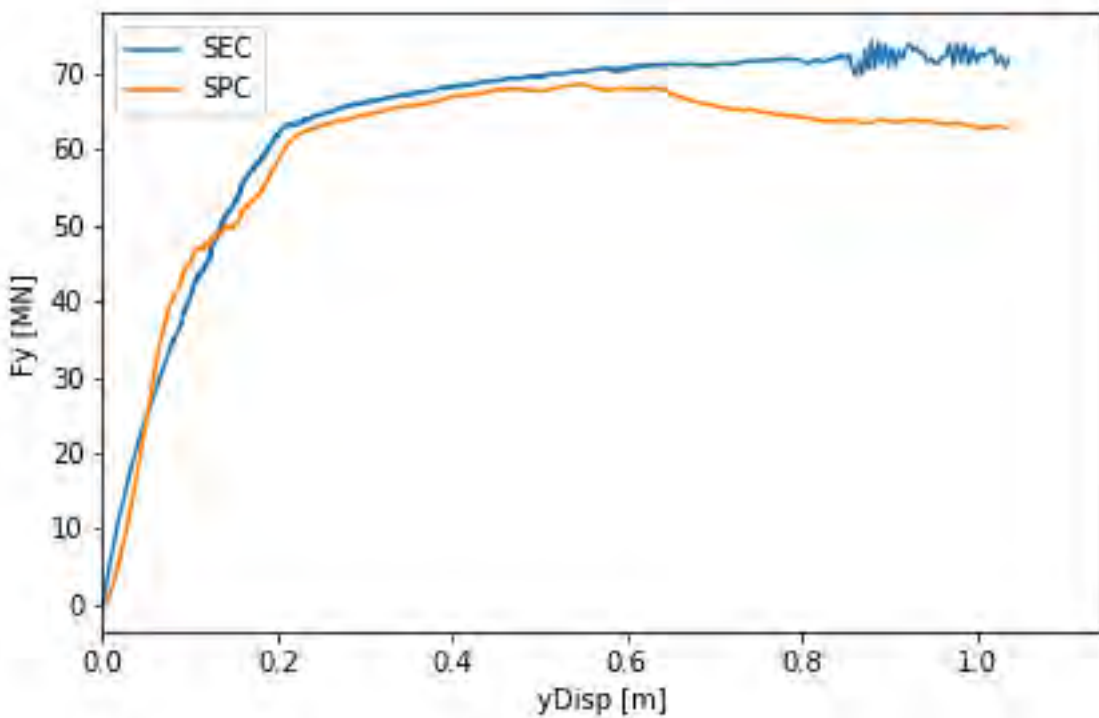
Figure 3-25 Force-displacement curve for short column with shear force in y-direction

This check can be avoided by running the analysis with deformations, rather than applying a load.

4 Discussion and further work

The results show that the plastic capacity in the short column is acceptable. However, the results indicate that further work is required to get a more accurate estimation on the plastic capacity of the long column situated at axis 3. This column has been found to have insufficient capacity against calculated forces from ship collisions. However, there a number of factors that may change the results:

- The analysis is based on cross-section properties taken from phase 3. The analyses should be re-run with the correct cross-section from phase 5. In addition an eigenmode analysis could be performed such that a more thourogh applicatiuon of imperfection can be performed

- Since only one column model exist, the longer column has been modelled by extending the short column. This simplification has showed that the cross-section properties for bridge girder/column intersection for the longer column has to be significantly increased compared to the short column.

- The forces from ship-pontoon collision, taken from ref. /4/, is from a previous phase and is hence based on a older pontoon design. Results based on the pontoon design presented in ref. /3/ should be included in ref. /1/ and compared to the calculated capacities.

- It is also of interest to run the analyses by including the column force history from the global analysis, or run a dynamic analysis in the global model with full interaction with the floating bridge

From Section 3.4 it is observed that the kinetic energy levels increases when the capacity is reached. This can be avoided by running the capacity check with implicit analysis and the *riks-solver* in LS-DYNA. An implicit analysis achieves equilibrium by solving the stiffness matrix once or even several times over the course of a time step.

5 References

/1/   10205546-11-NOT-077 AMC status 2 - Local collision analysis of pontoon, rev 0

/2/   DNVGL-OS-C401, Fabrication of offshore structures, July 2015

/3/   10205546-13-NOT-087 AMC status 2 - Design of pontoons, rev 0

/4/   SBJ-30-C4-NTNU-27-RE-001 Ship-pontoon collision analysis of the floating bridge concepts for Bjørnafjorden

Concept development, floating bridge
E39 Bjørnafjorden

Appendix J – Enclosure 3

Verification of fracture criterion

Appendix G Enclosure 03 Verification of fracture criterion

June 27, 2019

A. CALIBRATION OF FRACTURE CRITERION

The applied fracture method, described in section 3.3, is verified against a range of material tests and indentation tests covering a wide range of strain states, strain concentrations and variation of mesh between 1 and 10 times the plate thickness. Note that the criterion uses material theory, which then is calibrated towards the power law hardening parameters alone. Thus, rather than calibrating towards a known solution we simply verify the robustness of the criterion against many known solutions. The verifications can be found in ref. /1/, /2/ and /3/, and it is to our knowledge the most thoroughly verified fracture criterion for stiffened panel structures with the best performance and smallest statistical variation in predicted capacity up to fracture. A summary is given below, and compared to the new fracture criterion in the revised DNVGL-RP-C208.

Note that a 100% accurate prediction of fracture is not possible; partly due to challenges with structural discretization, partly due to structural deficiencies and partly due to variation of material parameters and imperfections. With a thorough benchmark study some of these challenges are captured and the robustness of the criterion can be identified. On the contrary, with calibration only towards one known solution one have to include a significant margin of safety to account for the variations in response when the reality is not equal to the calibration case.

The verification of the criterion is performed in two stages; first against material tests and second against indentation tests. The former gives a good impression of the overall robustness of the fracture criterion, and thereby how we would expect it to behave given changing circumstances from the original calibration. The latter demonstrates more directly the behavior of the criterion towards changing conditions in "real-life" structures, typically with a model scale of about 1:3.

The BWH criterion with a safety factor of 1.2 is compared to the simplified criterion in DNVGL-RP-C208 section 5.1.3. If not otherwise indicated, results with continuous lines are with the BWH criterion whereas dashed lines are with the RP-C208 criterion.

A.1 MATERIAL TESTS

A.1.1 Formability tests from Broekhuijsen, ref. /4/

Broekhuijsen /4/ reported results of material tests with varying stress triaxiality for 12 mm thick plates of mild steel. The material is of a similar grade to that used in the full-scale collision experiments reported by Peschmann /9/. Six different geometries were tested with a spherical indenter of 60 mm in diameter to obtain a forming limit diagram (FLD), with strain-rate ratios β between -0.19 and 0.66. The experimental setup is shown in Figure A-1. The FE mesh of the geometries with mesh size 10 mm (l_e/t_e = 0:8) are shown in Figure A-2, together with the simulation setup of a formability test with indenter.

The simulation results are shown in Figure A-3. The BWH criterion with damage, mesh scaling and safety factor is on the conservative side for all the simulations. The RP-C208 criterion (based on plane strain alone) is not surprisingly highly conservative for other strain states. More interesting, when simulating the FLD2 experiments with near plane

strain, RP-C208 still severely underestimates the capacity while the BWH criterion captures the physics fairly well.
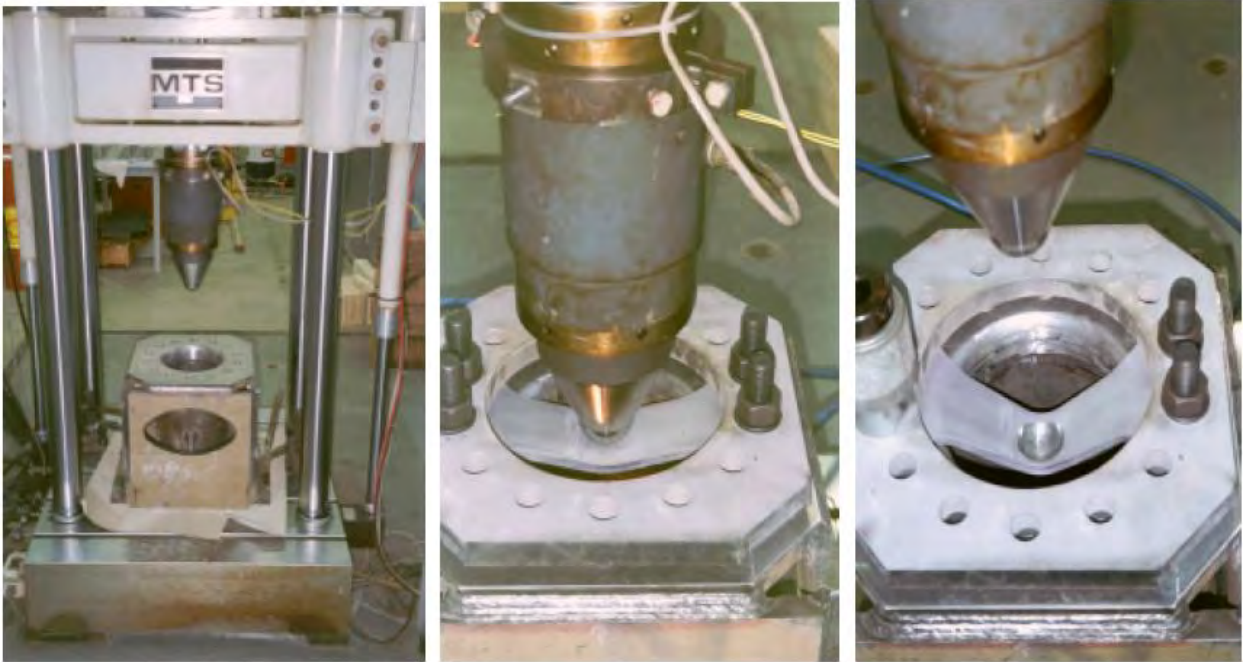
Figure A-1 Test apparatus and procedure
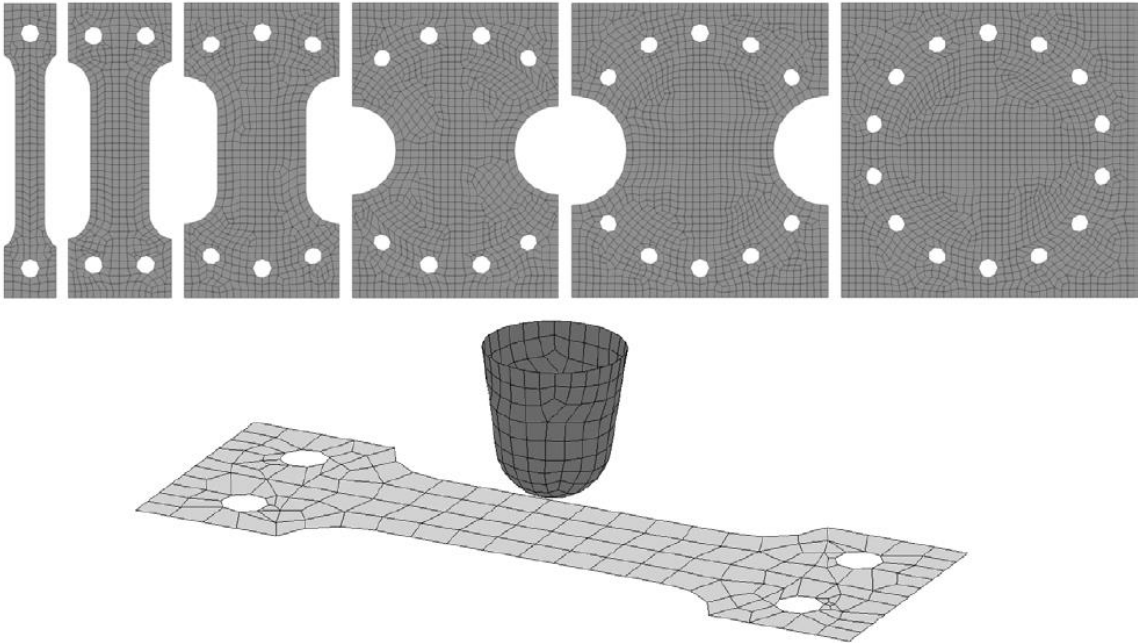
Figure A-2Formability models 1 (left) to 6 (right) with mesh size 10 mm (l_e/t_e = 0:8), and view of test setup with indenter (bottom) with mesh size 20 mm (l_e/t_e = 1:6).
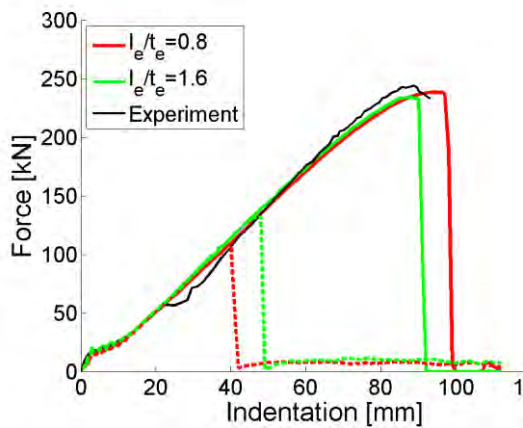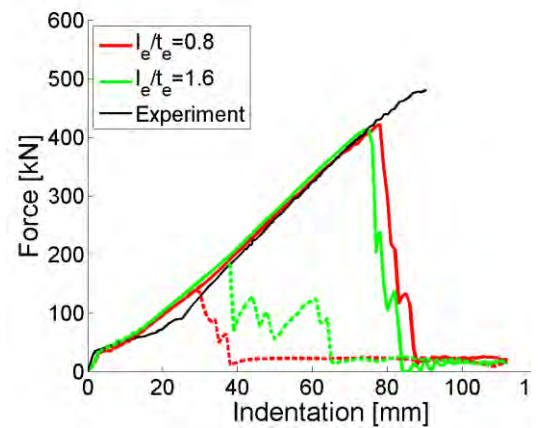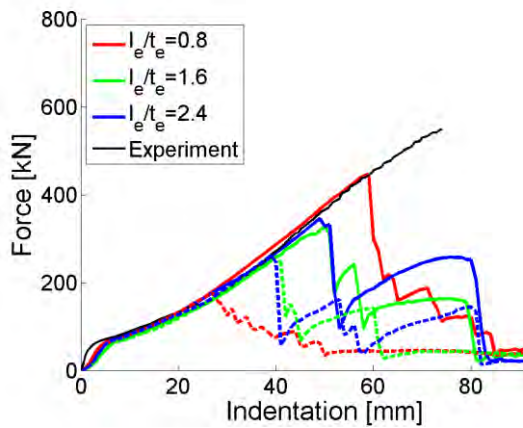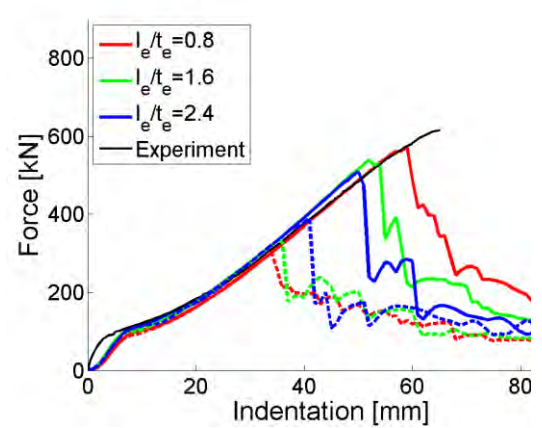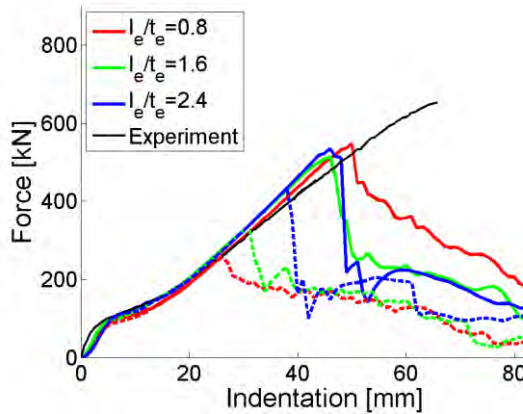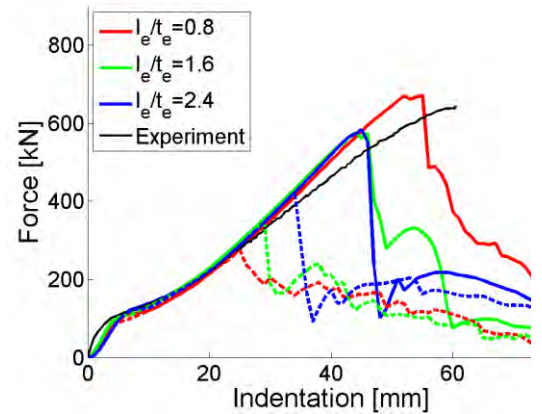
a) FLD 1, β=-0.19
b) FLD 2, β=0.03
c) FLD 3, β=0.28
d) FLD 4, β=0.43
e) FLD 5, β=0.44
f) FLD 6, β=0.66

Figure A-3 Simulation results of the formability experiment by Broekhuijsen

A.1.2 Nakajima tests from Gruben et al., ref. /5/

Gruben et al. conducted Nakajima formability tests for a dual-phase steel together with digital image correlation (DIC) measurements. By using DIC, the instantaneous strain field in the specimen is recorded through a high-speed video camera by post-processing the movement of the random speckle pattern sprayed over the test specimen. Hence, the evolution of strains is captured directly.

Figure A-5 compares the thickness strains at incipient necking (onset of instability) from Gruben et al.'s tests compared with the BWH criterion for the tested stress states. Without calibration to other parameters than the power law hardening, the BWH criterion manages to predict both the onset of instability and the subsequent fracture following local necking. For the highest stress states, the criterion somewhat underestimates the capacity compared to the tests.
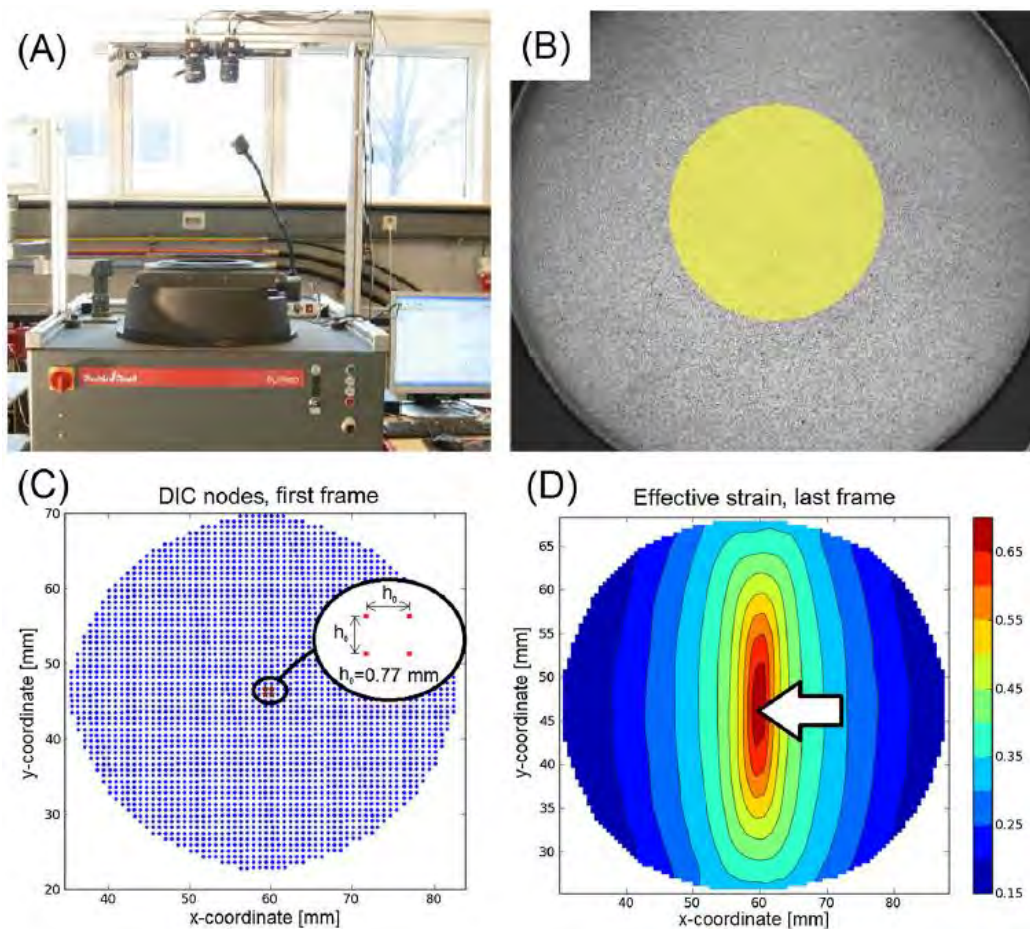
Figure A-4 Experimental setup and digital image correlation (DIC) measurements of strains, from ref./5/.
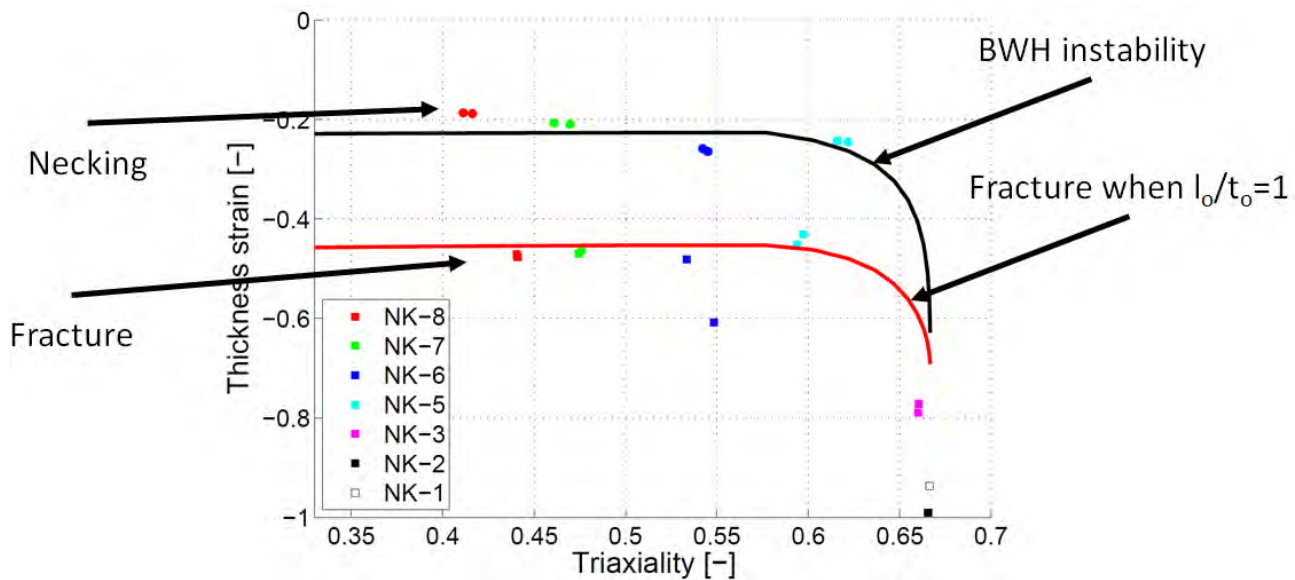
Figure A-5 Thickness strain at incipient necking and fracture, BWH criterion compared to experimental results

A.1.3   Plate tearing tests from Simonsen and Törnqvist, ref. /6/

Simonsen and Törnqvist (2004) investigated fracture propagation in shell structures through a tearing experiment, in which a mode-I crack was driven approximately 400 mm through a plate under displacement-controlled conditions. Many tests were performed using various materials and thicknesses; in the following, the experiments on 5 and 10 mm plates of normal-strength steel are considered. Plates of 700x580 mm were modeled, with an initial crack extending 150 mm into the long edge of the plate. The experimental crack had a blunt crack tip with a radius of 5 mm. In the simulations, this crack was created by simply removing elements 150 mm into the plate, leaving the crack tip sharp. This simplification is expected to lead to somewhat premature erosion of the initial elements and inaccuracy prior to stable fracture propagation. Four meshes were investigated; with characteristic element lengths of 5, 10, 20 and 40 mm. The material parameters are same as those used in Simonsen and Törnqvist (2004).

The simulation results are shown in Figure A-7. There is a clear difference in the propagation resistance of the crack between the RP-C208 and the BWH criterion, clearly illustrating that the post-fracture resistance is severely underestimated using the RP-C208 criterion.
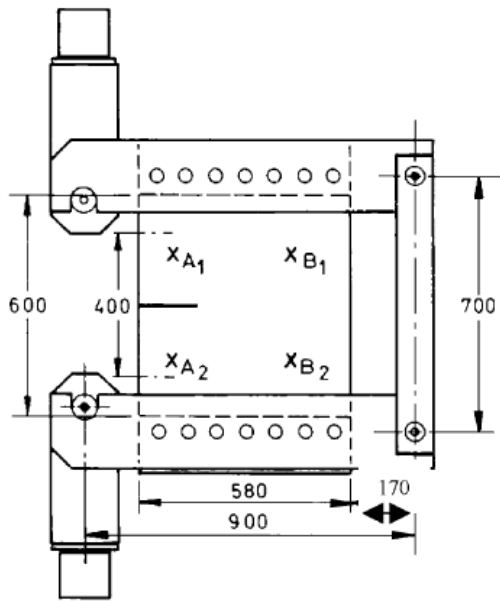
Figure A-6 Plate tearing test apparatus
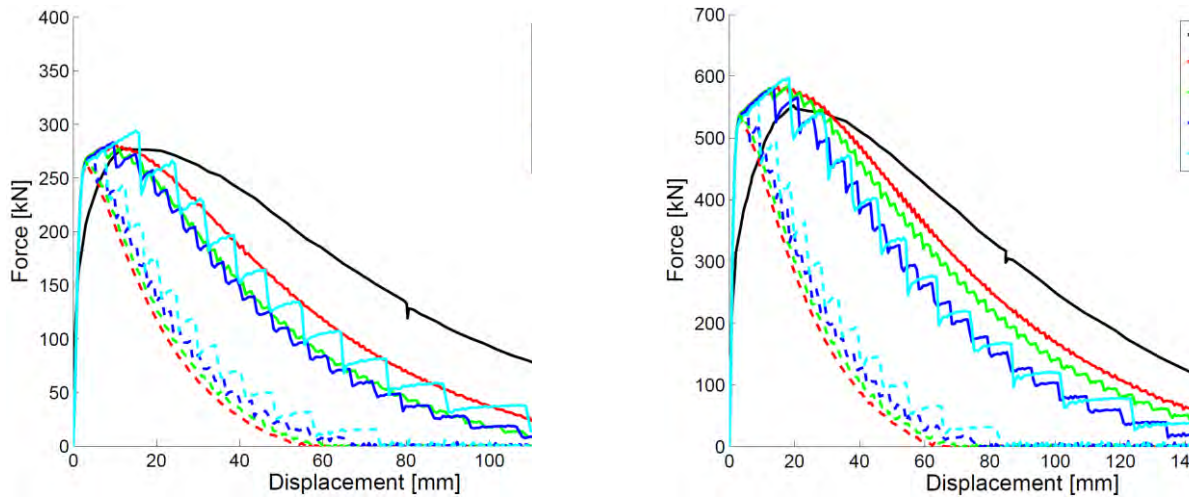
a) 5 mm steel plate   b) 10 mm steel plate

Figure A-7 Simulation results for the Simonsen and Törnqvist experiments.

A.2   INDENTATION EXPERIMENTS

A.2.1   Alsos and Amdahl, ref. /7/

Alsos and Amdahl (2009) performed indentation experiments using a rigid indenter and a panel with dimensions of 1200x720 mm. The plate thickness was 5 mm, and the stiffeners were flat-bars, FB120x6. The experimental results from the panels without stiffeners (US) and with one (1FB) and two (2FB) flat-bar stiffeners are considered in the following. The stiffener spacing's were 360 and 240 mm for 1FB and 2FB, respectively. The welds had overmatching strength and were modeled as thin shell elements with increased thickness in the plate and stiffeners (+2 mm for the plate, +4 mm for the stiffeners). The experimental setup is shown in Figure A-8. The hardening parameters for the material were selected based on the data reported in Alsos et al. (2009). A static friction coefficient of 0.3 was assumed.


The simulation results are shown in Figure A-9 in terms of force-displacement curves. Overall, both criteria are on the conservative side when estimating the response. However, RP-C208 is significantly more conservative than the BWH criterion. This is especially in the post-fracture phase, for which the RP-C208 criterion disregards most of the energy dissipation capacity due to the very conservative assumptions.

The results show a fair amount of scatter for the US and 1FB tests, whereas the 2FB test show less. This is due to the type of strain concentration in the specific problem. In the 2FB panel, fracture occurred in a strain-concentration close to the stiffener, in which geometric mesh scaling is appropriate. However, both for the US and 1FB experiments, fracture occurred in the free plate field. The mesh densities used in the simulations are able to capture this strain concentration reasonable well without mesh dependence. Hence, when applying geometric mesh scaling anyway, the capacity of the panels are underestimated. If geometry mesh scaling is turned off with the BWH criterion, the US

experiment is captured well without significant mesh variation, as shown in Figure A-9 (d). Applying geometric mesh scaling is always conservative, but not always relevant.

Figure A-10 compares the simulated vs. experimental fracture path when using the BWH criterion with damage and geometric mesh scaling, but without a safety factor. With decreasing mesh size, the fracture path is captured accurately. With increasing mesh size, the refinement is lost as the fracture is constrained to the mesh discretization. However, the onset of fracture and corresponding loss of capacity is captured well.
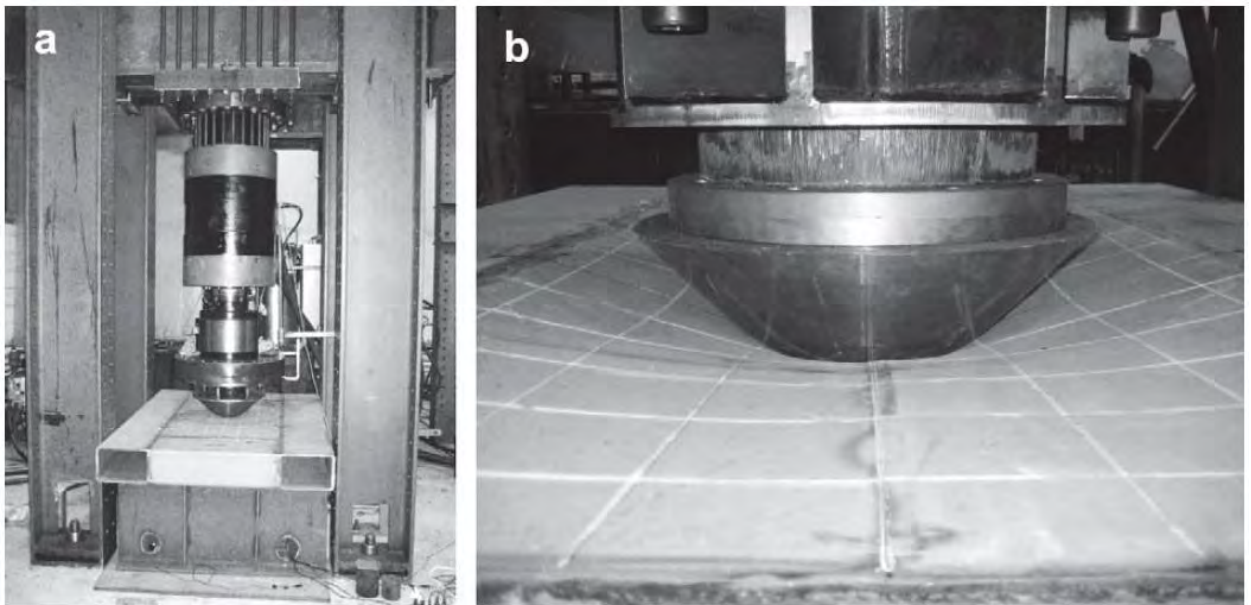
Figure A-8 Alsos and Amdahl's test rig
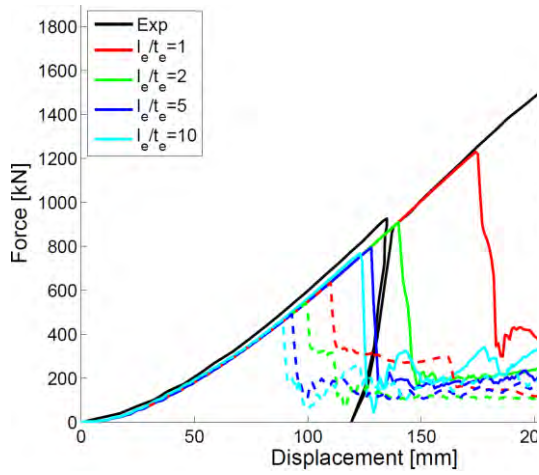
g) Unstiffened panel (US)
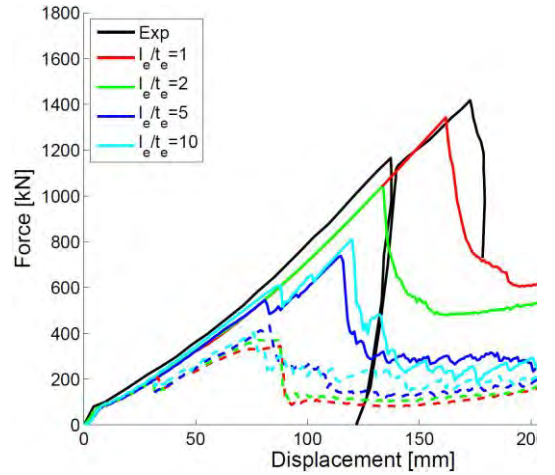
h) Stiffened panel w. 1 flat bar (1FB)
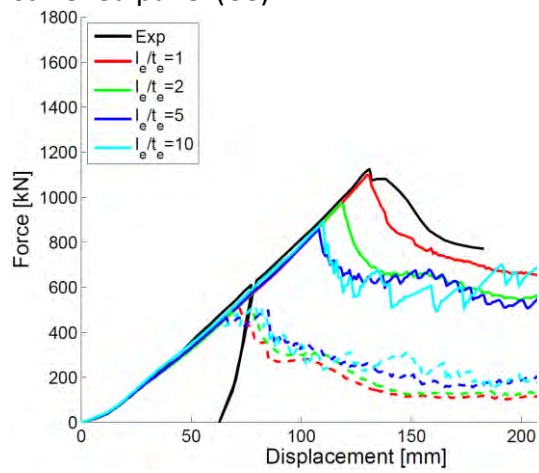
i) Stiffened panel w. 2 flat bars (2FB)
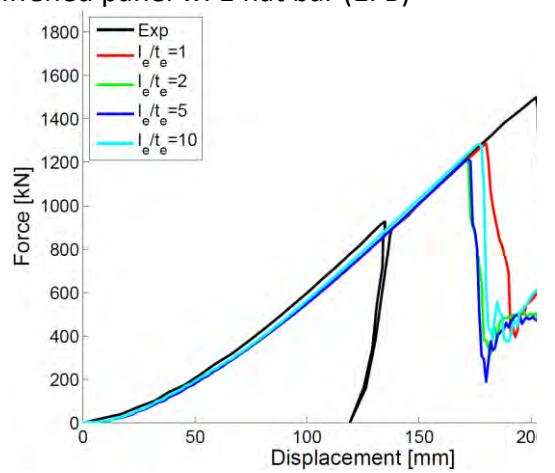
j) US panel with BWH criterion without geometric mesh scaling or safety factor

Figure A-9 Simulation results for the Alsos and Amdahl experiments. BWH criterion with damage as continuous lines, the RP-C208 criterion as dashed lines.

(a) Experimental failure mode, from Alsos (2008)
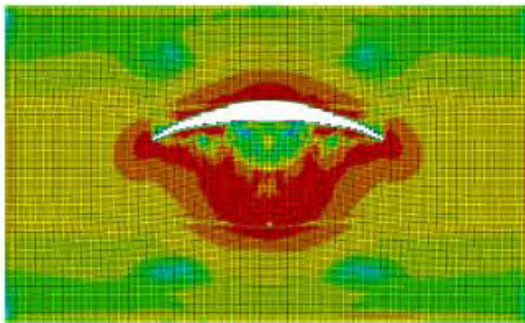
(b) $l_e/t_e = 1$
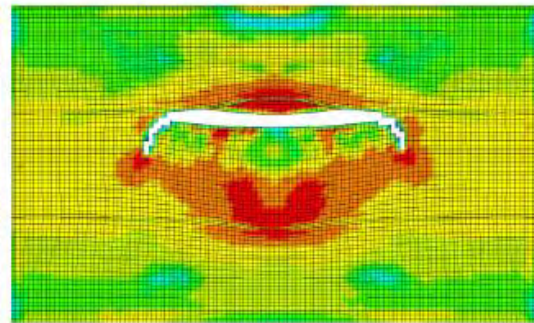
(c) $l_e/t_e = 2$
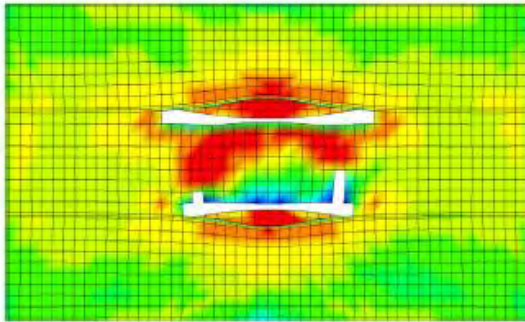
(d) $l_e/t_e = 5$
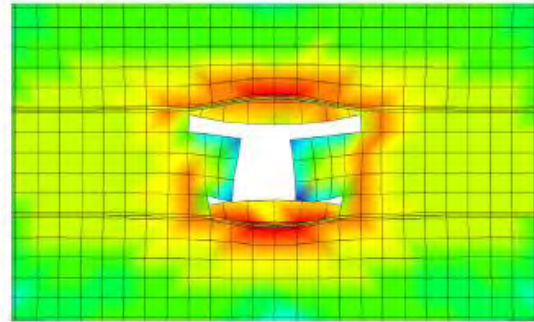
(e) $l_e/t_e = 10$

Figure A-10 Correlation between simulated and experimental fracture path using the BWH criterion with damage but without a safety factor on fracture.

A.2.2   Tautz et al., ref. /8/

Tautz et al. (2013) conducted indentation experiments using a model of a double-sided shell structure. The scale was approximately 1/3 compared to a large vessel. The plate of 4 mm thickness had bulb profile stiffeners (HP140x7) with a spacing of 280 mm. The frame spacing was 800 mm, with 5 mm plates containing 600x400 mm manholes. The total height from the outer to the inner shell was approximately 900 mm, and the total length of the deformable region was 4000 mm. Steel plates with a thickness of 20 mm were utilized at the boundary, creating a strong support frame around the panel. The experiments were performed using two types of indenters: rigid and deformable. Herein, only the experiment with the rigid indenter is considered for verification of the material model. Further details of the experiments can be found in Fricke et al. (2014) and Martens (2014) (both available in German only).

During construction of the tested shell structure, cutouts around the stiffeners were made in the web frames according to normal ship manufacturing procedures. The numerical simulations were conducted both with and without these cutouts. Figure A-11 shows the experimental setup.

The simulation results are shown in Figure A-12. With the BWH criterion with damage and safety factor, the experiment overall is simulated well. With the RP-C208 criterion, the resistance in the actual penetration phase of either outer or inner shell is significantly underestimated, but the transition phase through the double side is fairly acceptable.

Figure A-13 shows the fracture path in simulations vs. experiments. The BWH criterion simulates the fracture path remarkably well without calibration to more than the power law hardening parameters.
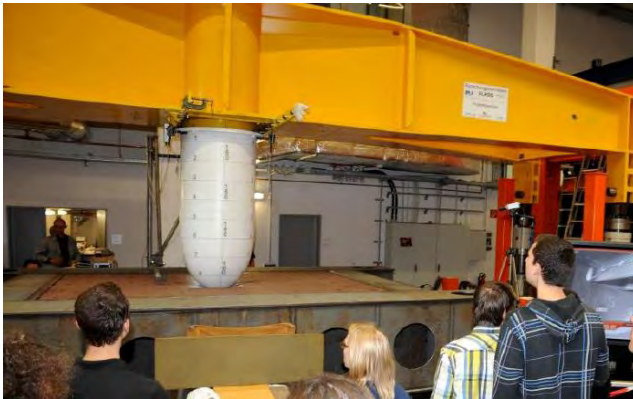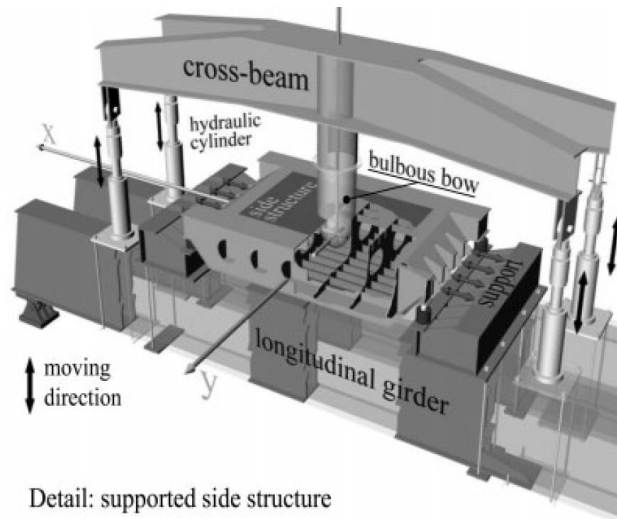
Figure A-11 Tautz et al. experimental setup
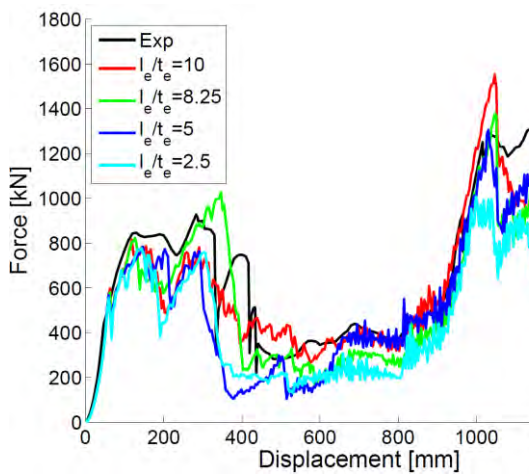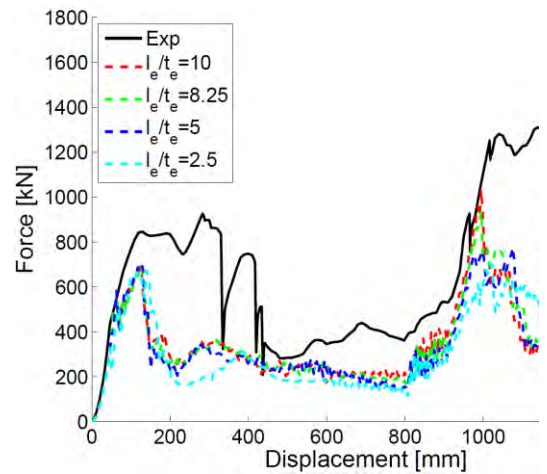
c) BWH criterion   d) RP-C208 criterion

Figure A-12 Simulation results for the Tautz et al. experiments, simulation with cutouts modelled.

(a) Experimental failure mode, figure from Fricke et al. (2014)
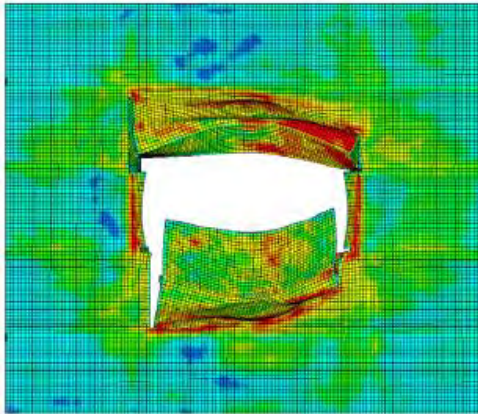
(b) Simulation with $l_e/t_e = 3.1$
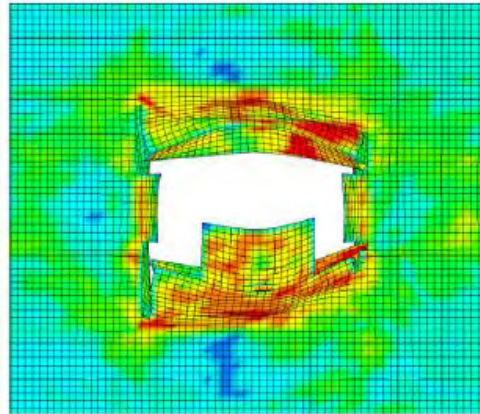
(c) Simulation with $l_e/t_e = 6.3$

Figure A-13 Simulated vs. experimental fracture path of the Tautz et al. experiments using the BWH criterion with damage and mesh scaling but without a safety factor.

A.2.3 Peschmann et al., ref. /9/

Peschmann (2001) reported data from large-scale collision tests performed on two inland waterway barges in the Netherlands during 1997 and 1998 by the research organization TNO, also documented in their report (Wevers and Vredeveldt (1999), not publicly available). An 800-ton tanker struck another 1400-ton tanker at a 90º angle at approximately 4 m/s. The striking vessel was fitted with a rigid bulb, and the struck vessel had a total of four different deformable side panels. The collision with test section 3 is considered for comparison herein because this panel most closely resembled a full-scale ship structure. The experimental setup is shown in Figure A-14, and the struck structure in Figure A-15. Note that due to the limitations with respect to experimental control due to the floating nature of the experiment, the actual impact location is not precisely known. Hence, the results of these experiments should be given less weight than those in Alsos or Tautz as we are not completely sure that the experimental conditions are represented in the simulations.

Figure A-16 shows the simulation results. The BWH criterion show results fairly close to the experimental force peak, whereas the RP-C208 criterion only use about half the capacity. Following this difference in estimation of first fracture, the energy dissipation during the rest of the experiment is significantly underestimated by RP-C208.

Figure A-14 Experimental setup, TNO experiments as reported in Peschman
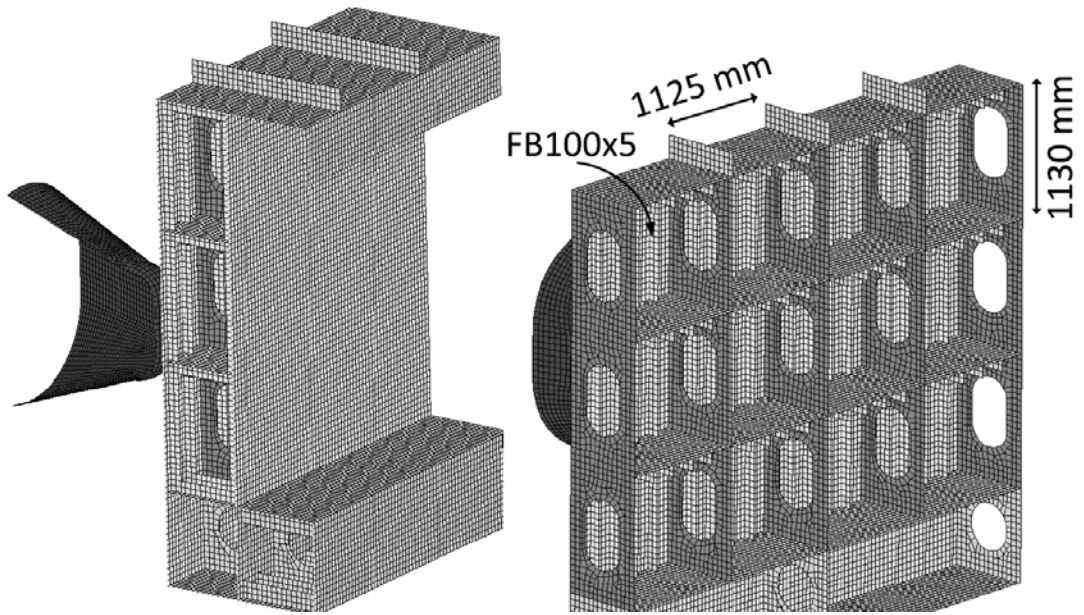
Figure A-15 Struck structure and indenter. Parts of structure removed for clarity
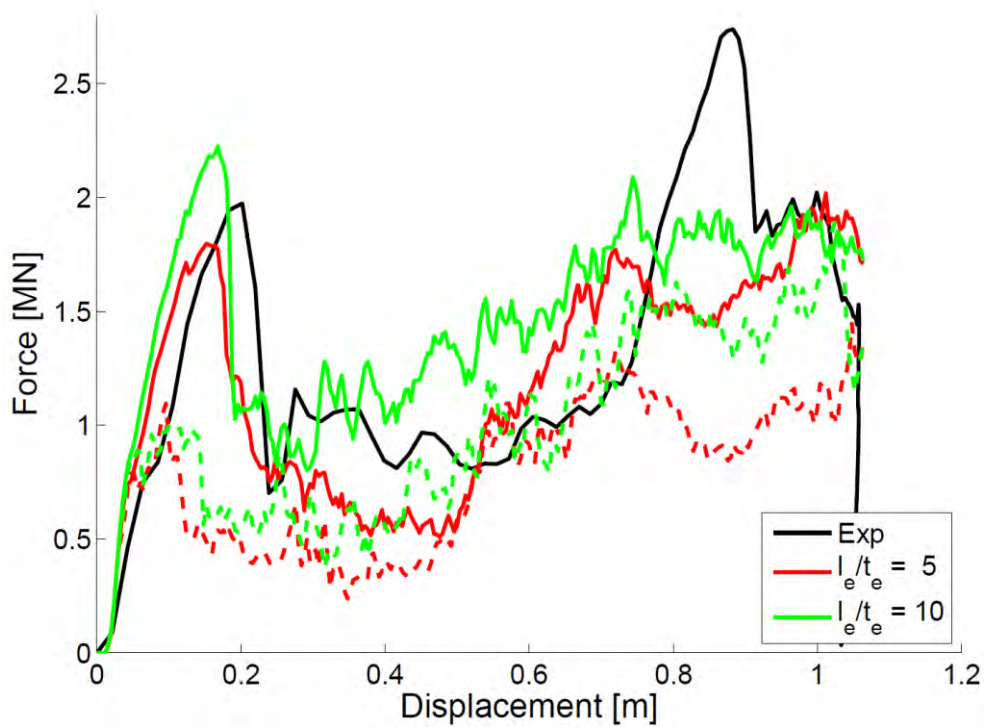
Figure A-16 Simulation results for the Peschmann experiments

A.3   SUMMARY OF RESULTS

A normalized energy is defined to compare the results for the range of experiments used in the current verification study. This relates the energy dissipated in the simulation to the energy dissipated in the experiment, thereby giving a more robust scale of verification than just comparing force or displacement alone. A normalized energy of 1 means that the experiment is captured perfectly.

Two different measures were compared (illustrated in Figure A-17); the energy to peak force and the energy to end of simulation. The first represent the accuracy of the fracture criterion to predict the onset of fracture and thereby the first large drop in resistance to deformation. The latter represents the overall behaviour of the complete system, including the post-fracture response. Hence, if onset of fracture is a governing design parameter, the energy to first peak force is most important. However, if large-scale fracture can be accepted provided that the structure does not collapse, the energy at end of simulation may be a more relevant parameter to check.
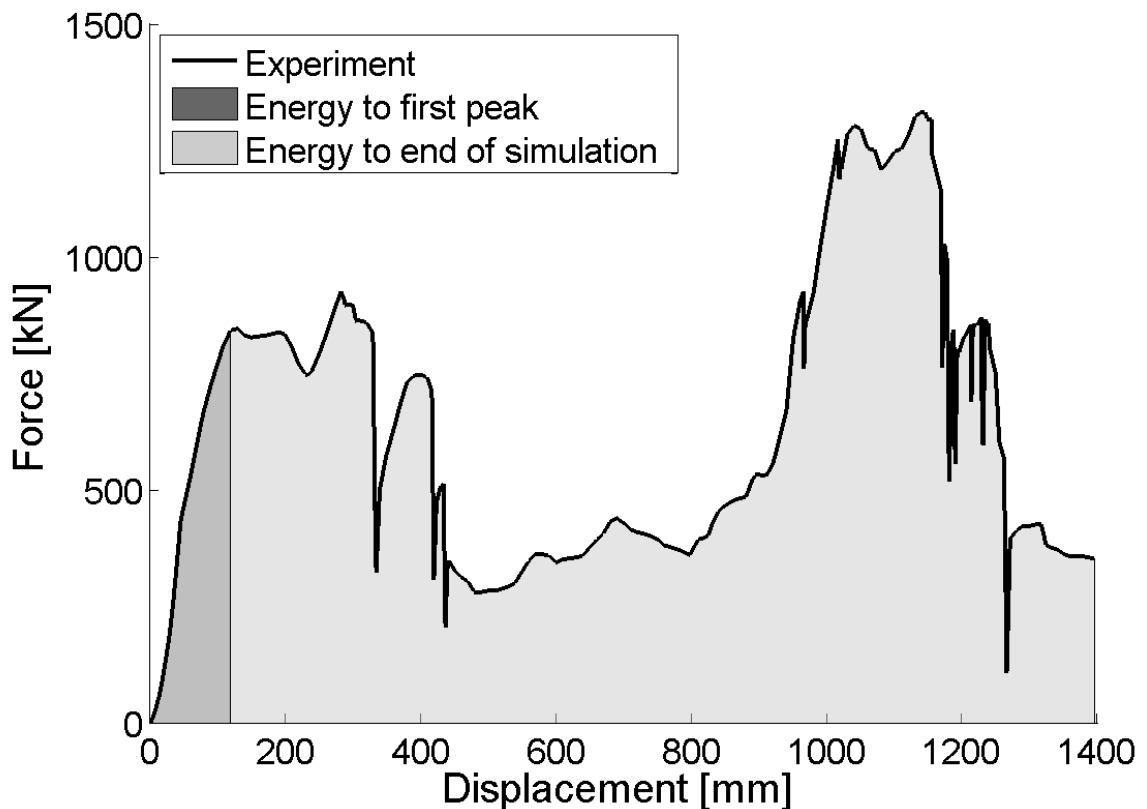
Figure A-17 Definition of normalized energy

Using the extensive numerical study, with a total of 46 simulations with around 1500 CPU-hours for each fracture criterion, a statistical comparison of the fracture criteria can be performed. In the following, the below listed fracture criteria are evaluated:

- **BWH:** BWH criterion with geometric mesh scaling and coupled damage

- **BWH w. safety 1.2:** BWH criterion with geometric mesh scaling and coupled damage. A safety factor of 1.2 is included in the calculation of critical principal stress for estimating onset of fracture (Eq. (6)) .
- **BWH w. safety 1.4:** BWH criterion with geometric mesh scaling and coupled damage. A safety factor of 1.4 is included in the calculation of critical principal stress for estimating onset of fracture (Eq. (6)).
- **RP-C208:** The simplified criterion in RP-C208 Section 5.1.3 (2016 draft edition), with separate fracture strains for membrane and bending calculated according to the prescribed calibration cases. For the experimental simulations, the measured stress-strain response of the material is used, and the fracture strain evaluated based on the initial yield stress. The load factor of 1.2 to be used together with the criterion is disregarded.
- **RP-C204:** The simple criterion from RP-C204 (also given in NORSOK N-004) as a function of element size vs. plate thickness.
- **GL:** The GL criterion (ref./10/), based entirely on measurements of fractured full-scale plates after collisions. Interestingly, the 5% gross strain limit as imposed in RP-C208 section 5.1.3 is not mentioned in the GL criterion.

Figure A-18 shows comparisons against different groups of tests. Figure A-18 (a) shows the material test results. Capturing a material test correctly is the true test of any fracture criterion; if the criterion fails to simulate the types of tests often used for calibration it will under no circumstance be an accurate and trustworthy criterion for simulations without a known solution. From the results, the BWH criterion shows a low statistical variation centered around about 80% of the experimental capacity. With inclusion of a safety factor, the mean decreases while the variability is fairly constant. The RP-C208 criterion systematically underestimates the experimental capacity, centered around 25%. Both the RP-C204 and the GL criterion shows a large statistical variability, and the mean results overestimate the experimental capacity. Similar tendencies are found in Figure A-18 (b).

Looking at the stiffened panels alone gives a good estimate of how the criteria perform against the complex interaction between the material behavior and the structural response, complicated further by the coarse mesh discretizations. Figure A-18 (c) shows the normalized dissipated energy up to first peak force. The BWH criterion without safety factor is centered around the actual experimental capacity, and with a fairly low statistical variability. Hence, the criterion gives a robust and accurate fracture prediction for onset of fracture. When including a safety factor, the capacity decreases quicker for the stiffened panels than for the material tests, likely due to the coupling between the mesh scaling and the safety factor. With a safety factor of 1.4, the BWH criterion is within the statistical variability of the RP-C208 criterion, but with a lower variability and higher mean. Hence, this safety factor on the BWH criterion gives the same robustness against overestimation of the capacity as with the RP-C208 criterion, but far more accurate. Both the RP-C204 and the GL criteria show high variability and a high mean energy to fracture.

If large-scale fracture can be accepted (providing that the residual capacity of the structure is sufficient), it is of interest to evaluate how the fracture criteria perform with

respect to energy dissipation after onset of fracture. Figure A-18 (d) shows these results. Again, the BWH criterion with or without safety factors behave predictably. On the other hand, the RP-C208 criterion reveals its full conservatism, with about 50% of the energy dissipation compared to the experiments. This is a significant discrepancy. In a collision scenario in the ductile energy regime, simulations with the RP-C208 criterion would yield about twice the damage as if a more accurate criterion was used. Hence, the conclusions as to how to counteract the imposed damage will be severely affected by an overly conservative fracture criterion.
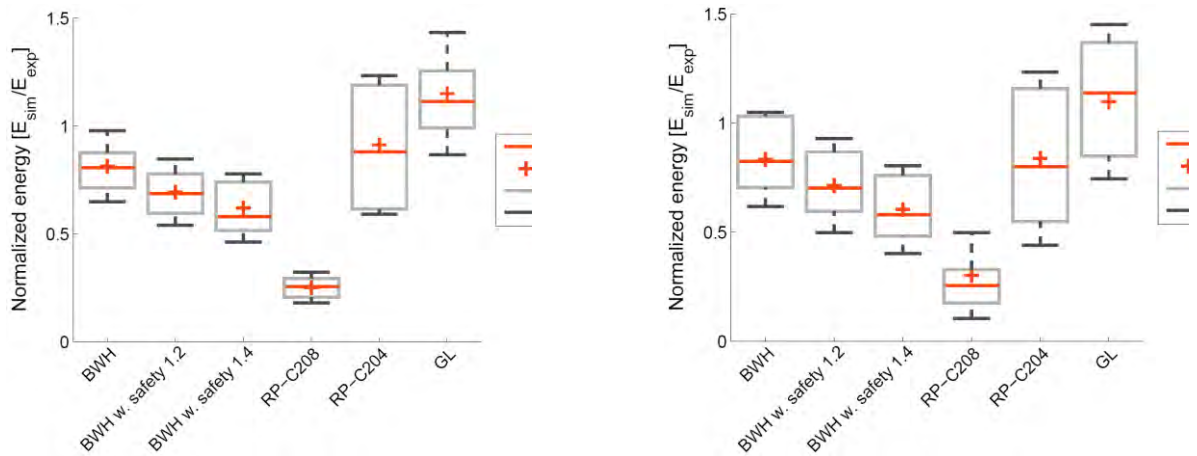
a) Material tests, peak force

b) All tests, peak force
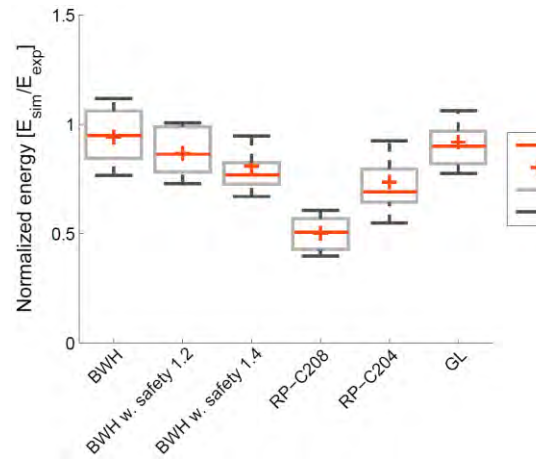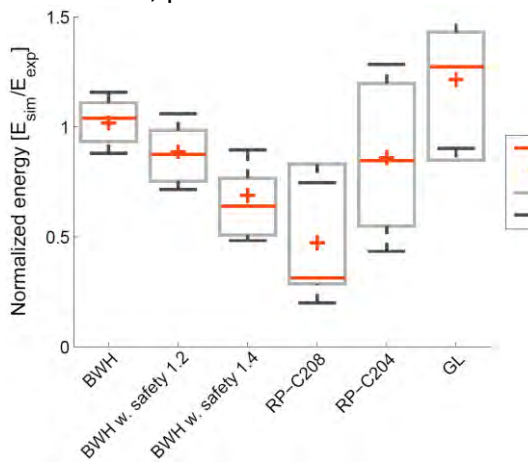
c) Stiffened panels, peak force

d) Stiffened panels, end of simulation

Figure A-18 Statistical comparison of behavior of the tested fracture criteria

Some differences may arise between the experiments that were used in this section to verify the structural response and a full-scale structure. Some of these are related to the fact that we simulate full-scale structures using lower bound parameters (in some cases severely conservative assumptions), which again change how the plastic strains localize and where fracture initiates. Further, there may be misalignments, bad welds and defects in the full-scale structure that are not present in the experiments. When using the BWH criterion with a safety factor of 1.2, we consider that we have sufficient margin to account for such discrepancies, but without being overly conservative.

REFERENCES

/1/ Storheim, M., Amdahl, J., and Martens, I. On the Accuracy of Fracture Estimation in Collision Analysis of Ship and Offshore Structures. Journal of Marine Structures, 44:254–287, 2015. doi: 10.1016/j.marstruc.2015.09.006.

/2/ Storheim, Martin. "Structural response in ship-platform and ship-ice collisions.", PhD Thesis, NTNU, Trondheim, Norway, 2016.

/3/ Storheim, Martin, Alsos, Hagbart S., Amdahl, Jørgen, Evaluation of nonlinear material behavior for offshore structures subjected to accidental actions, Proceedings of the ASME 2017 37th International Conference on Ocean, Offshore and Arctic Engineering, Trondheim, Norway, 2017

/4/ Broekhuijsen, J. Ductile failure and energy absorption of Y-shape test section. Master thesis, Delft University of Technology, 2003.

/5/ Gruben, G., Vysochinskiy, D., Coudert, T., Reyes, A., and Lademo, O.-G. Determination of Ductile Fracture Parameters of a Dual-Phase Steel by Optical Measurements. Strain, 49(3):221–232, 2013b.

/6/ Simonsen, B. C. and Törnqvist, R. Experimental and numerical modelling of ductile crack propagation in large-scale shell structures. Marine Structures, 17 (1):1–27, 2004.

/7/ Alsos, H. S. and Amdahl, J. On the resistance to penetration of stiffened plates, Part I : Experiments. International Journal of Impact Engineering, 36(6):799–807, 2009.

/8/ Tautz, I., Schottelndreyer, M., Lehmann, E., and Fricke, W. Collision tests with rigid and deformable bulbous bows driven against double hull side structures. 6th International Conference on Collision and Grounding of Ships and Offshore Structures, ICCGS 2013, June 17, 2013 - June 19, 2013, pages 93–100, 2013

/9/ Peschmann, J. Energy absorption computations of ship steel structures under collision and grounding (translated from German language). PhD Thesis, Institute for Ship Structural Design and Analysis, Hamburg University of Technology, Germany, 2001.

/10/ Scharrer, M., Zhang, L., and Egge, E. D. Kollisions-berechnungen in schiffbaulichen entwurfssystemen (collision calculation in naval design systems). Report,Bericht ESS 2002.183, Germanischer Lloyd, 2002.